KU LEUVEN

ARENBERG DOCTORAL SCHOOL
Faculty of Science

Filamentation and Dynamics in Coronal Loops

Xia Fang

Supervisor:
Prof. R. Keppens
Prof. T. Van Doorsselaere

Dissertation presented in partial fulfillment of the requirements for the degree of Doctor in Science: Mathematics

June 2016

Filamentation and Dynamics in Coronal Loops

Xia FANG

Examination committee:
Prof. A. Kuijlaars, chair
Prof. R. Keppens, supervisor
Prof. T. Van Doorsselaere, supervisor
Prof. S. Poedts
Prof. M. Goossens
Dr. C. Xia
Dr. J. Andries
(Royal Observatory of Belgium)

Dissertation presented in partial fulfillment of the requirements for the degree of Doctor in Science: Mathematics

June 2016

Uitgegeven in eigen beheer, Xia Fang, Celestijnenlaan 200B box 03.33, B-3001 Leuven (Belgium)

Acknowledgements

"When I walk along with two others, they may serve me as my teachers. I will select their good qualities and follow them."

—Confucius

First of all, I would like to thank my supervisors, Profs. Rony Keppens and Tom Van Doorsselaere for introducing me to the fascinating field of magnetohydrodynamics in the solar atmosphere, and for giving me the opportunity to be a PhD student at the Centre for mathematical Plasma Astrophysics (CmPA) in Mathematics Department of KU Leuven. I still clearly remembered the day that I met Prof. Rony Keppens in his talk at Nanjing University for the first time. Prof. Tom Van Doorsselaere is more like a friend, always smiling and encouraging me. Without their advice, guidance, and experience, it would have been impossible to write this Thesis.

A large portion of what I learned I owe it especially to Dr. Chun Xia whose experiences of the numerical simulation and kindness enriched greatly my formation. I am also very grateful to have had the opportunity to work with Dr. Antolin Patrick for the many inspiring discussions and great collaborative work.

During all these years in CmPA, I learned the importance of group unity. It is a pleasure to convey my gratitude to my office mates, Sofia Paraskevi Moschou, Dimitrios Millas, Jo Raes, Christine Verbeke, Ding Yuan and shaaban Mohammed. I would like to thank to rest the members of CmPA during the time I was there for the great atmosphere and support which made being a PhD student such as pleasure.

I would like to thank Dr. Rong Lu who helped me a lot both in studying and living in a foreign country. I would like to thank Prof. Pengfei Chen, Dr. Yang Guo, Dr. Qingmin Zhang, Dr. Zhixing Mei, and Xiaozhou Zhao for their help as well.

My last acknowledgment, is for my wife, Jingjie Guan, and for my parents, whose constant support and encouragement allowed me to find the motivation to finish my PhD and to write this Thesis. It is impossible for me to go through the four years without them.

Thanks to all of you!

Abstract

In this thesis I study the filamentation and dynamics in solar coronal loops by numerical models that directly confront observational findings. I consider coronal loops with a realistic arcade magnetic topology in quiet and active regions. I want to highlight how the extremely different energy releases in coronal loops located at different regions affect their thermal dynamical evolutions. I more specifically study how gradual footpoint heating triggers the thermal instability in coronal loops, as well as explore the phenomena related to explosive energy release in solar flares when more impulsive extreme heating is at play. To solve equations I use the code MPI-AMRVAC with a self designed user file, and self developed IDL and Fortran codes for the analysis.

After a general overview of the Sun's structure and solar phenomena provided in Chapter 1, Chapter 2 begins with the introduction of the MHD system and Computational Magnetohydrodynamics. Then we briefly introduce MPI-AMRVAC using a test run demonstrating for a solar prominence evolution.

In Chapter 3, we present the first 2.5 dimensional, magnetohydrodynamic simulations which capture the initial formation and the long-term sustainment of the enigmatic coronal rain phenomenon. We demonstrate how thermal instability can induce a spectacular display of in-situ forming blob-like condensations which then start their intimate ballet on top of initially linear force-free arcades. We also present a preliminary result of our 3D simulations of coronal rain.

In Chapter 4, we simulate the chromospheric evaporation and the following reflected patterns in a flare loop. We demonstrate that the quasi periodic propagating intensity variations match the previous observations well.

In Chapter 5, we propose a model for the formation of loop-top hard X-ray (HXR) sources in solar flares through the Inverse Compton mechanism, scattering the surrounding soft X-ray (SXR) photons to higher energy HXR photons.

A brief conclusion is draw in Chapter 6 and comes along with a short discussion of future plans.

Beknopte samenvatting

In dit proefschrift onderzoek ik de filamentatie en dynamica van coronale lussen in het kader van de astrofysica. Ik beschouw coronale lussen met een lineaire-kracht vrije magnetische topologie in rustige en actieve gebieden. Ik wil benadrukken hoe de zeer verschillende energie input in coronale lussen in verschillende gebieden hun thermische dynamische evoluties beinvloeden. Meer specifiek onderzoek ik hoe geleidelijke voetpunt verwarming de thermische instabiliteit in coronale lussen activeert, en verken ik het verschijnsel gerelateerd aan de explosieve energie die vrijkomt in zonnevlammen. Om mijn vergelijkingen op te lossen gebruik ik de MPI-AMRVAC code met een zelf ontworpen gebruikersbestand, en voor de analyse zelf ontwikkelde IDL en Fortran codes.

Na een algemeen overzicht van de structuur en fenomenen van de Zon in hoofdstuk 1, begint Hoofdstuk 2 met de introductie van het MHD systeem en Computationee Magnetohydrodynamica. Daarna introduceren we in het kort MPI-AMRVAC en voeren we een test uit op basis van een protuberans evolutie.

In hoofdstuk 3 presenteren we de eerste 2.5 dimensionale, magnetohydrodynamische simulaties die de initiele vormingen en lange termijn behouding van het raadselachtige coronale regen fenomeen vastleggen. We laten zien hoe thermische instabiliteit een spectaculaire vertoning van in-situ gevormde, blob-achtige condensaties kan induceren die vervolgens hun intieme ballet bovenop oorspronkelijk lineaire-kracht vrije arcades beginnen. We presenteren ook een eerste resultaat van onze 3D-simulatie van coronale regen.

In hoofdstuk 4 simuleren we de chromosferische verdamping en de resulterende gereflecteerde patronen in de vlam lus. We laten zien dat de quasi periodieke voortbewegende intensiteit variaties goed overeenkomen met de eerdere waarnemingen.

In hoofdstuk 5 introduceren we een model voor de vorming van harde X-ray (HXR) bronnen in zonnevlammen door het Inverse Compton mechanisme, dat de omringende soft X-ray (SXR) fotonen naar hogere energie HXR fotonen verstrooid.

Een korte conclusie is te vinden in hoofdstuk 6, tesamen met een korte discussie omtrent toekomstige plannen.

Contents

Chapter 1

Introduction

"Fine words and an insinuating appearance are seldom associated with true virtue."
—Confucius

In this chapter a general overview of the Sun's structure and solar phenomena is provided along with physical concepts associated with them. The chapter begins with an introduction to the Sun itself and its interior structure, then it discusses the Sun's atmosphere and magnetic field as well as its link to solar atmospheric activity, especially in the corona, like prominences, coronal rain and solar flares. Finally, solar flares are discussed in detail in terms of observations and the models we use to describe them. The chapter concludes with an overall outline of this thesis itself, describing the problems addressed.

1.1 General aspects about the Sun

The Sun, a main sequence star of spectral class G2, contributes about 99.8% of the mass of the whole Solar System.

There are more than 100 million G2 class stars in our galaxy, so the Sun is not so special from an astronomical point of view. However, as the closest star to Earth, the Sun has long been recognised as one of the most influential factors for life on Earth. Its relation to the seasons is key to marking the passage of time and the growth of crops. This made Sun vital to the survival of early civilisations with a deep curiosity of the Sun's nature and behaviour. A much more accurate scientific view of

the Sun has been developed in recent centuries. Although early civilisations depicted the Sun as a god, we now have verified it as the centre of the solar system. Many recently built telescopes, ground observatories, and space satellites have given us an unprecedented understanding of this nearest neighbour. In addition to as an essential energy source for the life on Earth, the Sun also plays an important role for the Earth's climate. As the solar plasma hosts conditions impossible to recreate on Earth, the Sun is considered as an ideal laboratory for studying plasma physics, magnetism, thermodynamics, shocks, and atomic physics. In addition it also provides an excellent opportunity to verify astrophysical models such as those of stellar evolution and solar system formation. Thus the study of the Sun and solar activity is vital for both improving our predictions of space weather and better understanding the fundamental physics which drives our Universe.

The Sun contains 74% hydrogen, 25% helium, and 1% metals. With a surface temperature of approximately 5800 K and central temperature of 15 million K, all of its material is in the plasma state. The Sun is believed to be approximately half way through its life with an age of 4.6×10^9 years. This is estimated from the oldest meteorites found to date with the assumption that they were formed around the same time as the Sun. Therefore this estimate of the Sun's age is uncertain.

The nuclear fusion of combining hydrogen nuclei into helium at the core of the Sun, is the power source of the Sun. The radius, mass, luminosity, chemical composition, surface temperature, age, and nuclear reactions are all key boundary conditions for determining the internal structure of the Sun. This is done via what is known as the Standard Solar Model (SSM, Bahcall et al. (1982)) which predicts a highly structured interior, outlined by the cartoon in Fig 1.1. As shown, the interior can be divided into three zones depending on the production and transport of energy. These are the core, radiative zone and convective zone. Fig 1.2 from Carroll and Ostlie (1996) presents the temperature and pressure (top panel) as well as the density and cumulative mass (bottom panel), as a function of distance from the Sun's centre. Extending from the centre to around 0.2 $R_\odot$ (1 $R_\odot$ = 1 solar radius), the core has an extremely high density of up to 1.5×10^5 kg m^{-3} and a temperature of about to 15×10^6 K, and the process of quantum tunnelling allows the protons to overcome the repulsive Coulomb barrier so that the attractive strong nuclear force can take affect. The energy continually generated by the nuclear fusion in the Sun's core is transferred through the two more outer layers to the Sun's surface finally.

The first layer, named the radiation zone, starts from the outer boundary of the core, 0.2 $R_\odot$, to 0.7 $R_\odot$. Over the width of the radiative zone the temperature and density drop to 0.04 MK and 2×10^2 kg m^{-3} respectively. Like the core inside, the radiative zone rotates as a solid body and the primary mechanism to transfer the energy from the core is thermal radiation. Because of the high densities in the radiative zone, photons are repeatedly scattered, resulting in a very short mean free path. The energy carried by photons is emitted, absorbed, and reemitted ceaselessly by surrounding protons, helium nuclei and other metal nuclei. These random thermal processes indicate that the photons have to spend an average 10^6 years to go through the radiation zone to slowly arrive at the inner boundary of the upper layer. The layer from 0.7 $R_\odot$ up to

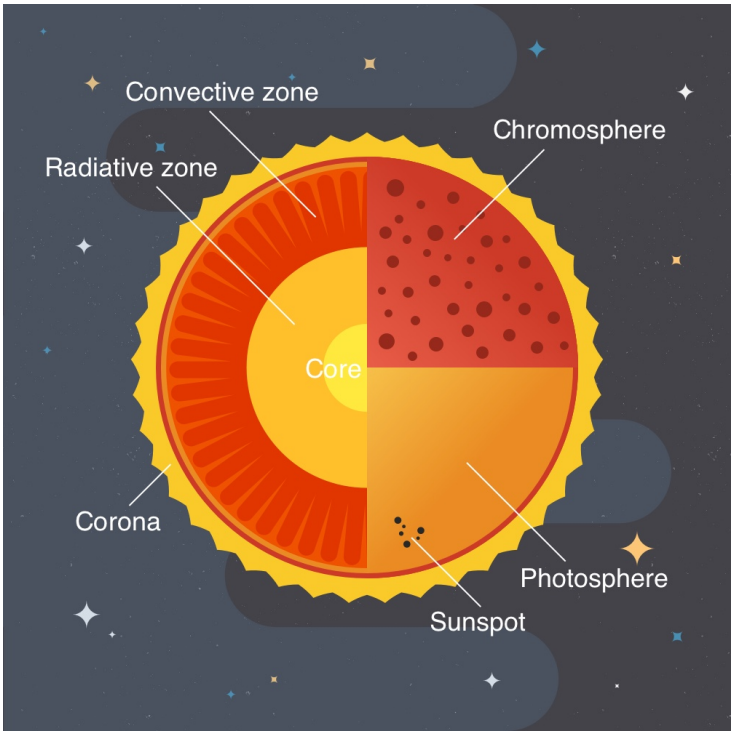

Figure 1.1: Cut-away cartoon of the Sun's interior shows the core, the radiative zone and the convection zone. It also shows the three different layers of the atmosphere as the photosphere, the chromosphere, and the corona. Drawn by Jingjie Guan.

the surface, is called the convection zone because the thermal convection dominates the energy transfer. The lower density and cooler temperature in the convection zone diminish the thermal radiation process which is more active in the radiation zone, and the temperature becomes low enough so that some nuclei can capture electrons. Moreover, the temperature gradient is too large for the material to remain in static equilibrium. As a result, thermal convection becomes the dominant energy transfer mechanism. By means of convective motions, large hot plasma volumes rise and carry heat toward the Sun's surface. The predominant thermal convection infers that huge hot plasma volumes release part of their thermal energy once they rise up to the Sun's surface.

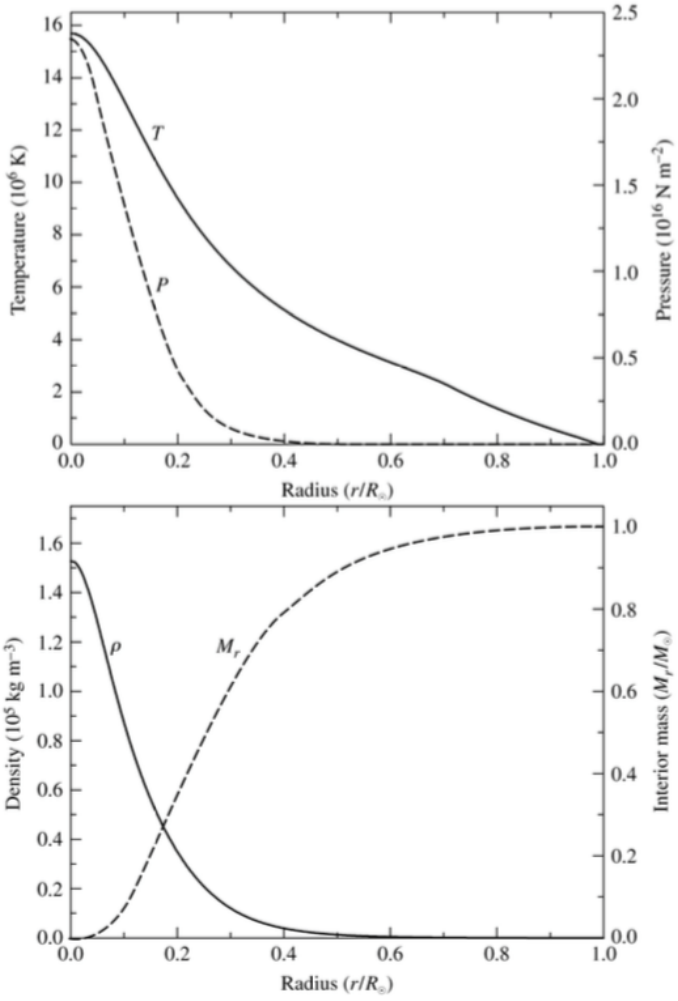

Figure 1.2: Plots of temperature and pressure (top panel) and density and cumulative mass (bottom panel) as a function of distance from the Sun's centre as predicted by the Standard Solar Model. Adapted from Carroll and Ostlie (1996).

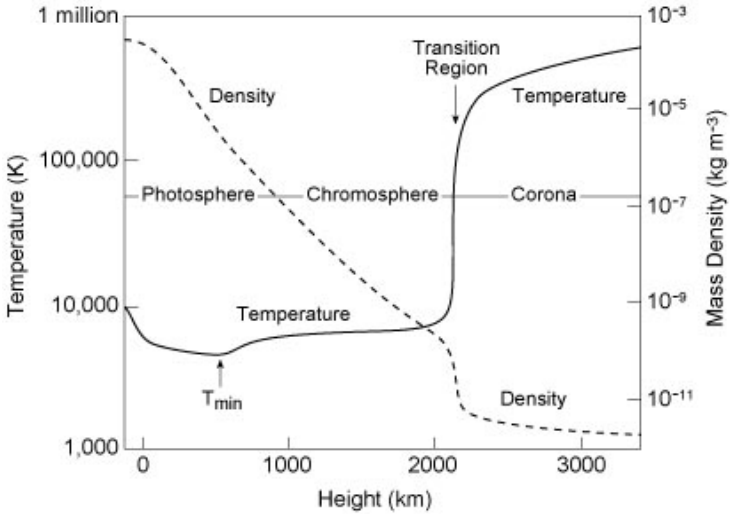

Figure 1.3: Schematic drawing showing the density and temperature as a function of height above the surface in the solar atmosphere. Although the temperature decreases monotonically from 15×10^6 K at the Sun's centre to about 5800 K at the surface in Fig 1.2, it only takes a few thousand kilometers above the surface for the plasma to reach 10^6 K again. Meanwhile the density keeps monotonically decreasing from the solar surface. (Courtesy of Eugene Avrett, Smithsonian Astrophysical Observatory.)

1.2 The Solar Atmosphere

Over the centuries, we have witnessed continuous improvements in astronomical observation to build up an increasingly comprehensive view of the Sun and its physical properties. On top of the solar convection zone, one finds the the solar atmosphere, which is traditionally divided into four layers: the photosphere, chromosphere, transition region, and corona. These four layers are distinguished through their different thermodynamic conditions. Fig 1.3 shows the temperature and density profiles of the solar atmosphere. The density decreases roughly exponentially throughout the first few hundred kilometers, and then falls off more slowly with height (more as a power law). A total of 9 orders of magnitude are spanned in density from the photosphere to the corona. The magnetic field does not decrease abruptly above the solar atmosphere, rather more gently, which results in two totally different plasma regimes: from non-magnetic to magnetic-dominated. The plasma β parameter, defined as the ratio of magnetic pressure to gas pressure, is the most intuitive proxy for understanding the structuring of the solar atmosphere: the photosphere ($\beta \gg 1$), the chromosphere ($\beta \gtrsim 1$ to $\beta \lesssim 1$) and the corona ($\beta \ll 1$).

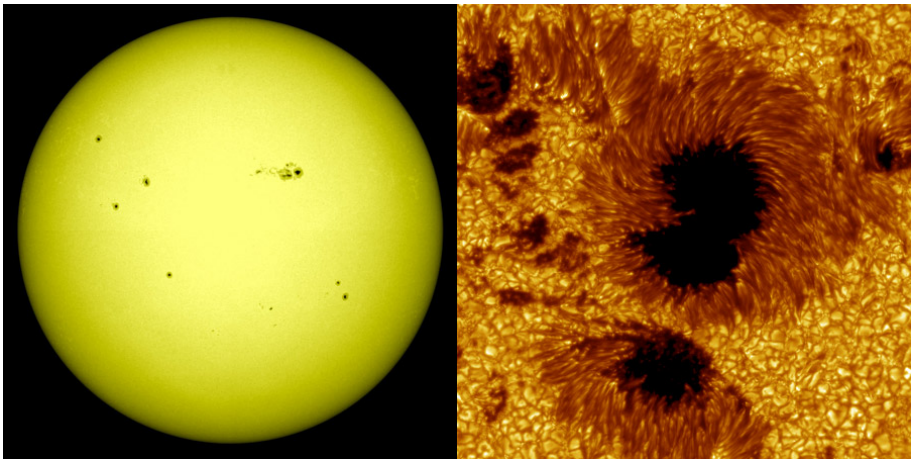

Figure 1.4: Left panel: shows several sunspots on the full disk of the Sun as viewed by NASA's Solar Dynamics Observatory (SDO) spacecraft on November 9, 2011. Right panel: shows a closeup view of a sunspot group as seen through a ground-based solar telescope operated by the Royal Swedish Academy of Sciences in the Canary Islands. Credit: NASA/SDO and the AIA, EVE, and HMI science teams and Royal Swedish Academy of Sciences.

1.2.1 The photosphere

The part of the Sun which we can see by the naked eye is named the photosphere, the first layer of the solar atmosphere. The thickness of the photosphere is only 550 km, with the typical number density of 10^{17} cm^{-3} and temperature varying from 6,000 K at its base to 4,000 K at its upper boundary, seen as the very first decrease of the temperature in Fig 1.3. In spite of its thinness, the photosphere has been the major source of information on the Sun. Roughly 50% of the incident light escapes out into space from the photosphere, meaning that the Sun radiates an overwhelming large fraction of the energy transfered from the lower convection zone as visible and infrared radiation. The observations of the photosphere indicate that its spectrum can be considered as a blackbody with a temperature about 5800 K. The left panel of Fig 1.4 shows an image of the photosphere taken by SDO/AIA at 4500 Å, a visible wavelength where the photosphere is rather featureless. The photosphere is observed to be covered by irregularly shaped and constantly moving granules which are the tops of the convective cells from the upper convection zone.

From photospheric observations, the most well-known features are the dark sunspots seen as black spots in the left panel and a close view at the right panel in Fig 1.4. Sunspots are magnetic phenomena caused by the emergence of magnetic flux from the solar interior. At the centre of a sunspot, the magnetic field strength can be larger than 1,000 G. The reason why the sunspots appear dark is that because the stronger

magnetic pressure inside them overcomes the gas internal pressure which affects and suppress the local magneto convection, to cause the temperature inside to be lower than the surrounding photosphere, ∼3,000 to 4,000 K instead of ∼5,800 K.

Another important observed characteristic, the acoustic waves, driven predominantly by pressure fluctuations, are revealing the Sun's internal pulsations. These oscillations are generated by the combined effect of linear to nonlinear plasma dynamics in the stellar interior and convection zone, trigging a tremendous number of waves travelling inside and across the Sun. The key point of these oscillations is that waves with longer wavelengths penetrate deeply into the Sun and back to the photosphere, and can provide verification of the structure of the Sun. This vast amount of wave-deduced information about the solar interior forms the basis for helioseismology.

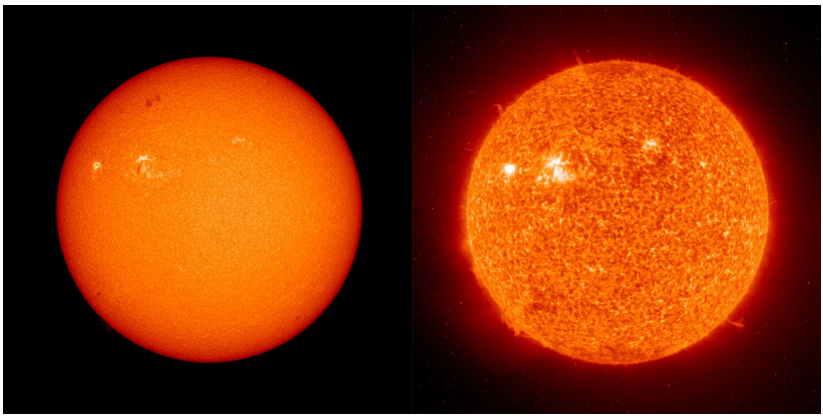

Figure 1.5: At thursday, March 24th, 2016, left panel: shows H-alpha (6,563Å) image of the Sun from the Big Bear Solar Observatory at Big Bear Lake, CA; right panel: shows ultraviolet (304Å) image of Sun taken by the SOHO Extreme Ultraviolet Imaging Telescope. Credit: NASA/SDO and the AIA, EVE, and HMI science teams.

1.2.2 The Chromosphere and Transition Region

Just beyond the photosphere, the temperature rises again as shown in the Fig 1.3. The first slow rising temperature part is named Chromosphere, whose typical thickness is 2 Mm, and the next explosive rising temperature region is called Transition region of only a few hundred kilometers thick. For naked eyes, the chromosphere is usually not visible since the brightness of the underlying photosphere dominates it. However, the Chromosphere can be visible during a total solar eclipse, appearing as a thin reddish ring. We can see the Chromosphere on the entire disk through the visible spectrum (6563 Å) as shown in the left panel of Fig. 1.5, and the emission in this line is also the reason for the name. Different from the photosphere, the chromosphere shows

constantly appearing and disappearing spicules, small jet like structures that pop up into the transition region and corona. The right panel of Fig 1.5 shows the upper chromosphere and lower transition region with the light taken at 304 Å.

The number density of the Chromosphere ranges from 10^{16} cm^{-3} at its bottom to 10^{11} cm^{-3} at its top, while the temperature increases gradually with altitude from 4000 to 10000 K near the top of the chromosphere. The vast majority of the dissipated energy in the Chromosphere is lost through the excitation of elements, resulting in a relatively constant temperature of the gas with height. In such a condition, a photon travels a long distance before interacting, leading to the importance of non-local thermodynamic equilibrium radiative processes (know as non-LTE radiative processes).

The transition from $\beta \gtrsim 1$ to $\beta \lesssim 1$ from the Chromosphere to the Transition region indicates that the magnetic field starts to dominate the thermodynamics of the gas and allows wave conversion processes which regulate the energy conversion between kinetic, magnetic and thermal energy (Aschwanden, 2004). From the chromosphere, the magnetic field begins to expand and fill the vast majority of the solar atmosphere as shown using an SDO/AIA 1700 Å view with extrapolated field lines (Fig. 1.6). Both closed and open magnetic field lines can be found, depending on the height (more closed field lines are found at lower heights), but also depending on the region in the Sun. Where the magnetic field dominantes over the gas pressure ($\beta < 1$), one defines the magnetic canopy, in which there exists a special relevance for wave heating mechanisms (Aschwanden, 2004). Also electric fields become vital for small spatial scales and associate with current sheets through anomalous resistivity, leading to ohmic dissipation and magnetic reconnection processes.

Above the chromosphere, a very thin (few hundred Km) layer called the chromosphere-corona transition region (CCTR) exhibits extraordinary changes there, as its name claims. The number density of CCTR decreases from 10^{11} to 10^{9} cm^{-3}, while the temperature grows rapidly from 25,000 K to almost 1 MK (10^{6} K). These astounding changes appear to violate the laws of thermodynamics, which is quoted as the coronal heating problem. Acoustic and magnetic waves, spicules, and nanoflares have all been suggested as the cause, however large uncertainties still remain and no consensus has yet been reached.

1.2.3 The Hot Corona

The upper layer above the Chromosphere is called the corona which is extremely tenuous with typical densities of 10^{7} cm^{-3} and temperatures of 2 MK. It is very faint, six orders of magnitude dimmer than the photosphere in visible light. Therefore, it's only visible during a solar eclipse, similar to the chromosphere as shown in the left panel of Fig 1.7. The visible light seen here is not emitted, but reflected from the photosphere via free electrons, which is known as Thompson scattering. The left panel of Fig 1.7 shows helmet streamers which are clearly visible at 3 o'clock and 11 o'clock. Helmet streamers are regions of relatively dense plasma contained by the coronal magnetic field. They have been dragged out into almost triangular structures by the

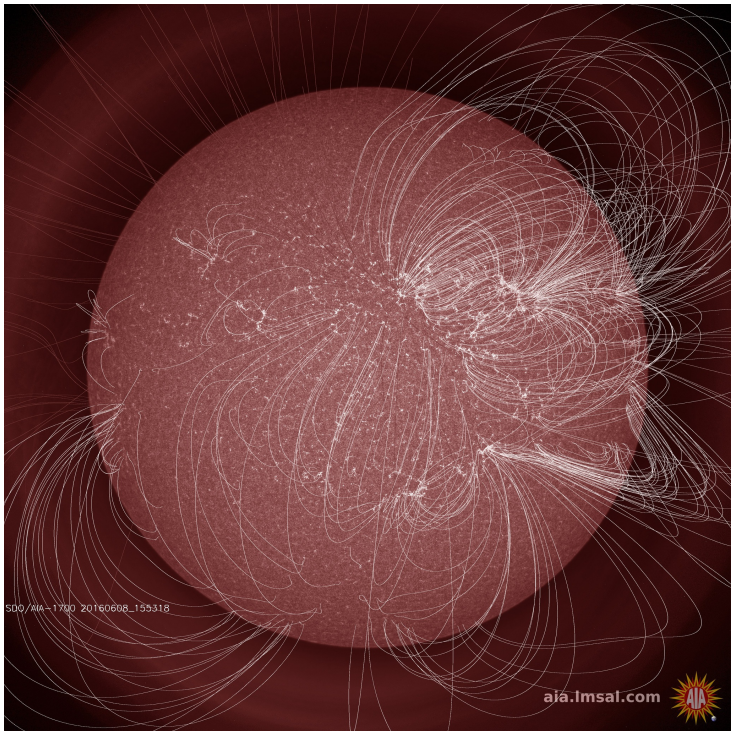

Figure 1.6: May 18th, 2016 PFSS Magnetic field lines on the Sun, over 1700 Å band of SDO. Credit: NASA/SDO and the AIA, EVE, and HMI science teams.

solar wind, a steady stream of particles released into the solar system, or heliosphere. There are two types of solar wind, fast (700 km s^{-1}) and slow (400 km s^{-1}). The fast solar wind is typically associated with coronal holes. Also visible in Figure 1.7 are polar streamers, long thin straight features emanating from the poles which outline the open polar magnetic field lines. Nowadays the corona is more typically examined with a coronagraph which creates an artificial eclipse by placing an occulting disk in front of a camera. Depending on the size of the disk, it is possible to image different regions of the corona. The more light is blocked out from close to the Sun, the further out into the increasingly faint corona one can see. The development of coronagraphs has greatly improved our knowledge of the outer corona and allowed us to track features such as coronal mass ejections (CMEs) further out into the heliosphere than ever before.

Spectroscopic observations by Grotrian of the solar corona in the late 1930s revealed unusual absorption lines in the visible spectrum (Grotrian, 1937). The mysterious transition lines were interpreted as belonging to an unknown element at the time which was then called coronium. Later, in the 1940s, the correct interpretation of the

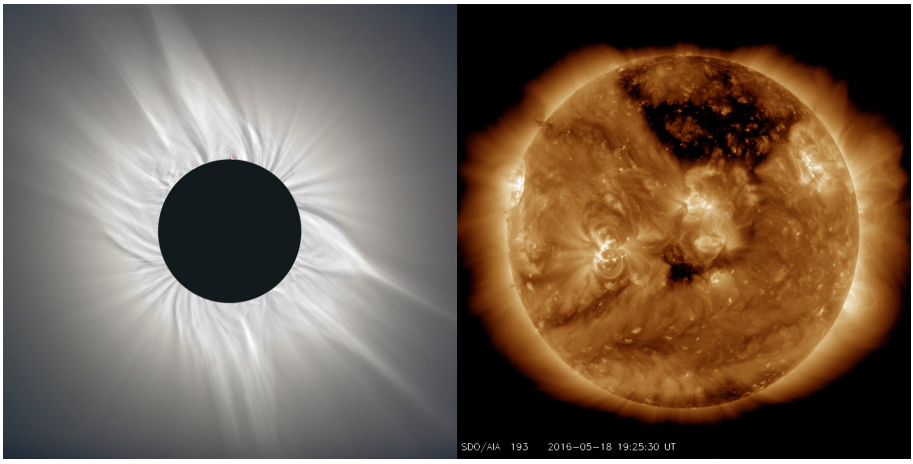

Figure 1.7: Left panel: the Sun's corona in visible light during a total solar eclipse that occurred in March of 2006. This reveals its complex and highly non-spherical structure, largely determined by the solar magnetic field. Right panel: the corona viewed at 211 Å band from SDO/AIA.Credit: NASA/SDO and the AIA, EVE, and HMI science teams.

spectral lines discovered by Grotrian was put forward by Edlen showing that they corresponded to transitions of highly ionized iron (Edlén, 1945), namely, Fe X and Fe XI. Rapidly, the discovery of further spectral lines of highly ionized elements followed. It was then realized that in order to reach such levels of ionization the gas in the corona had to be in a very hot permanent state, with temperatures above one million degrees Kelvin. Therefore, beside the visible light, the strong Extreme Ultra-Violet (EUV) and X-ray emission emitted by the high temperature of the coronal gas could also be useful for observing the corona.

In the early 70s, EUV and soft X-ray (SXR) observations of the solar corona made by Skylab (launched in 1973) pointed out that the solar corona is highly structured. The right panel of Fig 1.7 shows the corona viewed at 211 Å band from SDO/AIA, which represents the corona of 1 MK and highlights the global inhomogeneity of it. The EUV image in the right panel of Fig 1.7 of the corona most strikingly reveals the importance of the corona's magnetic field and its topology as shown in Fig 1.6. The particularly strong emission in the corona, sharing the same location of sunspots in the photosphere, indicates that the plasma above sunspots is dense and hot. The large loop-like structures spreading all over the corona are thought to reveal the topology of the magnetic field there. On the other hand, dark regions in the right panel of Fig 1.7 can be found near the top and bottom of the solar disk. These dark regions are known as coronal holes which locate at regions of open magnetic flux and do not hold the coronal plasma, but guide it into the heliosphere. Recent observations have emphasized the dynamic and variable nature of coronal structures, as well as

that the coronal plasma is dominated by the ambient magnetic field, which emerges continuously from below the photosphere and changes on timescales from hours to days. Thus the appearance of the corona at any instant reflects the geometry and strength of the magnetic field which permeates the solar atmosphere.

The corona keeps in an extreme hot permanent state, with temperatures above one million degrees Kelvin (MK). However, comparing with the temperature of the corona, the temperature of the underlying photosphere is several hundred times lower, close to 5800 K. This huge discrepancy in temperatures between the corona and photosphere is a mystery, introducing the coronal heating problem in solar physics. As explained above, the corona consists of a very tenuous gas with a number density around 10^8 cm^{-3}. In order to maintain a million degree temperature, balancing the energy losses by optically thin radiation and thermal conduction, the energetic input for the corona is estimated to be 10^5 erg cm^{-2} s^{-1} for quiet Sun and 10^6 erg cm^{-2} s^{-1} for active regions (Withbroe and Noyes, 1977). Although the resulting requirement only takes a very small portion of the total radiative energy flux of the Sun (5.4×10^{10} erg cm^{-2} s^{-1}), nevertheless, due to the tenuous corona, most of the photons from underlying layers (photosphere and chromosphere) could escape without interacting with the gas in the corona, meaning almost none of the photon energy is transfered to heat the coronal gas. Then we need to find a reasonable mechanism which can transfer the required amount of energy from the underlying layers and dissipate the energy in the appropriate length and time scales in the corona. Since the 1930s, many different heating mechanisms have been proposed to solve this mystery. However, so far there is no solid conclusion of any proposed coronal heating mechanisms (Taroyan and Erdélyi, 2009).

The first attractive theory is based on acoustic heating (Schwarzschild, 1948) since acoustic waves are easily generated by the solar granulation. However, it was soon realized that the energy budget from these waves was only enough for the lower chromosphere, not enough for the corona. Around the same time, Alfvén (1947) proposed that magnetic modes would carry the required energy to heat the corona. It was found that the energy flux from these waves was enough to supply the estimated heating. However the easy reflection and refraction of the fast and the slow magnetohydrodynamic (MHD) mode posed a problem for it to be accounted as a viable coronal heating agent. Then the Alfvén mode was found able to carry enough energy into the corona and not to suffer from reflection nor refraction. Alfvén wave heating became one of the leading candidates for heating the solar corona but then the problem shifted to how these waves can release their energy globally. The important role played by the magnetic field in the heating of the solar corona became apparent since the days of the Skylab mission (1970s). The simultaneous magnetogram and X-ray image of the Sun reveal the correlation between the strong magnetic field regions and high temperature regions in the solar atmosphere, suggesting a magnetic origin for the coronal heating mechanism.

Parker (1988) suggested another strong candidate of coronal heating. Due to the constant shuffling of the magnetic field from convective motions, the resulting build-up of magnetic stresses as non-potential free magnetic energy in the corona was suggested

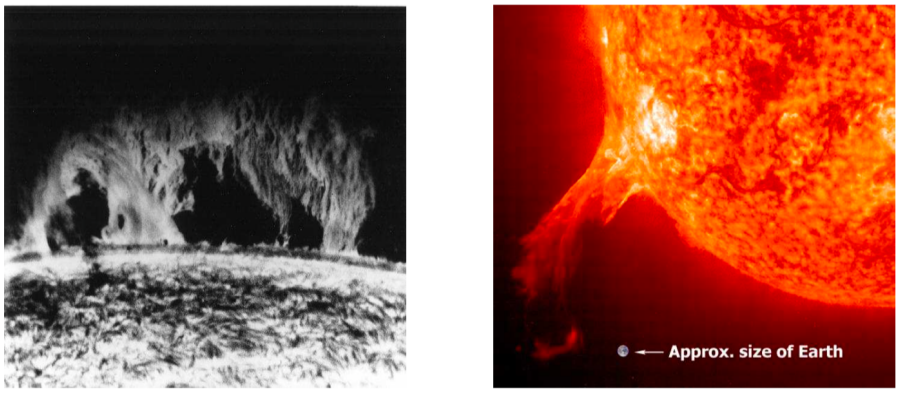

Figure 1.8: On the left: a classic H (6563 Å, T ≈ 10,000 K) image of a prominence at the solar limb from the Big Bear Observatory (1970). On the right: an image in EUV (304 Å, T ≈ 60,000 - 80,000 K) from the SOHO spacecraft, where an erupting prominence is compared to the size of Earth.

to be dissipated in discrete events uniformly distributed over the corona. These events are thought to be magnetic reconnection events in which the bulk of the dissipation takes place either through anomalously high resistivity (Parker, 1957; Sweet, 1958) or through slow shocks in the reconnection region (Petschek, 1964). Parker estimated the energy release in such events to be roughly 10^{24} erg, that is, 10^9 times smaller than that of a solar flare, thus giving rise to the nanoflare concept.

Now the heating mechanisms have been divided into categories regarding the timescales in which they perturb the magnetic structures in which they act. On one hand we have alternating current (AC) heating mechanisms, in which the perturbation of the magnetic field is faster than the relaxation time of the structure, e.g. waves. On the other hand we have direct current (DC) heating mechanisms, or stressing models, in which the perturbations caused on the magnetic structures are slow compared to the relaxation time. In this case the coronal magnetic field lines become twisted, braided, shuffled around, or sheared. They build up non-potential free magnetic energy, which eventually becomes unstable and released by a magnetic reconnection process (Taroyan and Erdélyi, 2009).

1.3 The Cool Corona

However not everything in the corona is extremely hot and tenuous. Some astonishing features in the corona are solar prominences, which are clouds of relatively cool (10^4 K) and dense gas (10^{17} m^{-3}). Some other similarly interesting features are coronal

rain with the same temperature and density as of prominences, but they have a very different morphology and life time.

Both coronal rain and prominences are manifestations of a phenomenon called thermal instability in plasmas (Field, 1965) which was first applied to prominences (Parker, 1953). The thermal instability has also been suggested as the reason for the formation of some larger scale structures: planetary nebulae (Zanstra, 1955), spiral arms condensing out from the galactic halo (Spitzer, 1956), and condensation of interstellar clouds (Field, 1962). Numerical simulations in the last 30 years have largely contributed to the understanding of thermal instability (Goldsmith, 1971; Hildner, 1974; Mok et al., 1990; Antiochos and Klimchuk, 1991; van der Linden and Goossens, 1991a,b; Antiochos et al., 1999; Mok et al., 2008). The thermal instability occurs when radiative cooling dominates over heating in some region. This can happen following a density perturbation (anything leading to an increase of the density, such as a shock wave) since the cooling increases faster than linearly with density. As a consequence, temperature and pressure drop in the perturbed region, accreting gas from the surroundings and forming an increasingly larger condensation. This cascading effect proceeds until heating and cooling balance again at some lower temperatures and higher densities (and when pressure balance is regained).

In the case of the solar corona, this thermal instability leads to thermal non-equilibrium or catastrophic cooling. High densities necessary for the instability onset are thought to be achieved through footpoint heating. The coronal heating is concentrated towards the footpoints of coronal loops. In such a scenario, chromospheric evaporation together with direct mass injection into the corona from the heating events ensure the gradual building of a dense corona. Thermal conduction becomes insufficient in transporting enough energy to the dense corona, whose temperature is consequently reduced over time. At some point a critical state is reached in which any small density perturbation is enough for triggering the thermal instability. The catastrophic cooling and condensation that ensues implies recombination of elements. The partially ionized clumps form and become visible in cool lines. Depending on the existing forces (gravity, magnetic and gas pressure gradients), the clumps either fall (coronal rain), or stay (prominences). Since the material can remain over long periods of time in the corona supported by the magnetic field, the element population can differ significantly between coronal rain and prominences, as well as the thermodynamics. It is thus important to distinguish both phenomena.

1.3.1 Prominences

Prominences are large-scale coronal magnetic structures which are the subject of many present investigations. Recent reviews by Labrosse et al. (2010) and Mackay et al. (2010) provide more detailed information about the physics of solar prominences. Although prominences are located in the corona, they possess temperatures a hundred times lower and densities a hundred or a thousand times higher than typical coronal values. The fact that its physical conditions are akin to those in the chromosphere suggests one possible scenario for prominence formation, in which prominences are

made of chromospheric material which has been lifted up into the corona. Although the processes that lead to prominence formation are still under investigation, another proposed scenario to explain how prominences acquire their mass is in-situ condensation and cooling of plasma from the surrounding corona. In eclipse or coronagraph pictures, these objects appear bright at the limb but on the disk they form dark ribbons. They have typical lengths of 10^5 km, heights of 5×10^4 km and widths of 6×10^3 km. As the rest of the solar atmosphere, prominences are roughly composed of 90% hydrogen and 10% helium. The prominence plasma is only partially ionized and the hydrogen ionization degree could probably vary in different prominences or even in different regions within the same prominence (Patsourakos and Vial, 2002). Regarding helium, recent studies by Gouttebroze and Labrosse (2009) indicate that for central prominence temperatures, the ratio of the number densities of He II to He I is around 10%, whereas the presence of He III is negligible. It is well established that prominences exist above the polarity inversion line that divides two regions of opposite magnetic polarity in the photosphere. The prominence itself is thus embedded in a larger coronal arcade that connects the two opposite polarity regions. Prominences that appear in regions well removed from solar active regions are called quiescent and maintain their overall shape for days or weeks and can even exist for several solar rotations. A prominence forms over time-scales of about a day. The so-called quiescent prominences may persist in the corona for several months, whereas active prominences (i.e., those located in active regions) have life-times of only minutes or hours. At the end of their life, some prominences may suffer an instability with a subsequent eruption. Such eruptions are sometimes accompanied by a flare or coronal mass ejection. Due to their longer life-time, quiescent prominences have been more studied than the active ones. Some basic questions about the nature of prominences are still unsolved, e.g., how is the denser prominence material supported against gravity in the much less dense corona, and how is the cooler prominence plasma thermally isolated from the much hotter external medium. There is no doubt that the magnetic field is responsible for keeping up the prominence plasma and maintaining it thermally shielded, but the precise structure and orientation of the magnetic field lines, especially in the surrounding corona, is still enigmatic and not well-known.

1.3.2 Coronal rain

Observations show recurrent formation and reshuffling of cool and dense material in coronal loops. The small scale ($\mathcal{O}(100)$ km) coronal rain is observed as cold, dense elongated blob-like features condensing in a much hotter loop and descending along one of its legs. The rain is guided by the loop magnetic field (Beckers, 1962), dropping from heights of tens of Mm into the chromosphere (Kawaguchi, 1970; Leroy, 1972). Similar phenomena have been observed by analysing absorption profiles in EUV spectral lines (Schrijver, 2001; O'Shea et al., 2007). Seen to propagate from the top of the loop towards its footpoints (De Groof et al., 2004), systematic intensity variations in EUV spectral lines are confirmed as downflows of cool plasma, rather than representing slow magneto-acoustic waves (de Groof et al., 2005). In addition to downflows towards footpoints, Tripathi et al. (2009) also found upflows towards

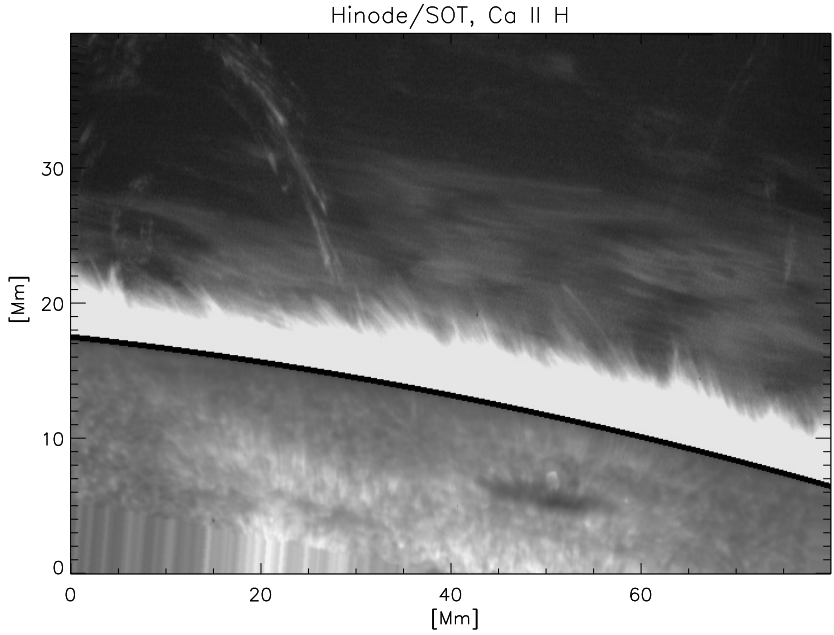

Figure 1.9: High-resolution Hinode/SOT image at the limb in the Ca II H line on 2006 November. The intensity of coronal rain in the Ca ii H line is about 1% of the on-disk photospheric intensity. (from Antolin et al. (2010)

the loop apex. Antolin et al. (2010) observed and tracked coronal rain in 30 active region loops and found more than one hundred descending condensations within 71 minutes as shown in Fig 1.9. Tracing the cool material towards loop footpoints, Kamio et al. (2011) observed propagating patterns suggesting a hot upflow following the downflows, supplying hot plasma into the loops. Antolin and Rouppe van der Voort (2012) suggested that coronal rain consists of plenty of small blobs, with sizes around 300 km in width and 700 km in length on average. They also estimated the occurrence rate of coronal rain in active region loops to be once every two days. Since the solar corona is swamped with magnetic loops, this suggests a scenario where coronal rain is rather common.

In view of the very small sizes involved, one of the most attractive features of coronal rain is that it can be used to probe the local magnetic field structure, or that it can expose valuable properties of the local thermodynamic conditions inside coronal loops (Antolin et al., 2010). Indeed, the magnetic field structure has a much longer lifetime than the timescale for condensations to form and fall (Beckers, 1962). Additionally, due to the low temperature (of order 10^4 K) of these condensations, coronal rain is normally observed in cold chromospheric lines (Levine and Withbroe, 1977; Müller et al.,

2005). Coronal rain results from thermal instability, with its non-linear counterpart and evolution also known as thermal non-equilibrium or catastrophic cooling. The linear thermal instability takes places whenever radiative losses locally overcome the heating input and is governed by well-known stability criteria for uniform radiative plasma conditions (Parker, 1953; Field, 1965). These can be met in the coronal temperature range, as one encounters locally negative slopes in the radiative loss function $\Lambda(T)$ as function of temperature. When thermal conduction is insufficient in transporting enough energy to cooling (and condensing) material, the temperature reduces over time. As a consequence of thermal instability, temperature and gas pressure drop dramatically in the perturbed region, resulting in matter sucked in from the surroundings to the perturbed region, forming an increasingly larger and cooler condensation. This runaway effect will continually increase the density and decrease the temperature of condensations until heating and cooling achieve a balance again at lower temperatures and higher densities.Numerical simulations have contributed to our understanding of thermal instability over the last 40 years (Goldsmith, 1971; Hildner, 1974; Mok et al., 1990; Antiochos and Klimchuk, 1991; Dahlburg et al., 1998; Antiochos et al., 1999, 2000; Karpen et al., 2003, 2006; Mok et al., 2008; Karpen and Antiochos, 2008; Xia et al., 2011). Early numerical work shows that in the million degrees solar corona, small temperature contrasts could be enhanced by line and recombination-driven radiative losses within several minutes (Goldsmith, 1971). Catastrophic cooling drives recombination of elements in the cool condensations, making them partially ionized and visible in cool chromospheric lines. Hildner (1974) concluded that the rate of condensation is determined by hydrodynamical processes mainly.

An important progress in modeling was obtained in Antiochos and Klimchuk (1991), by using a spatially dependent heating increase that is localized nearer to the chromospheric footpoints than to the loop midpoint. With this localized heating at the footpoints, Dahlburg et al. (1998) pointed out that another key requirement to generate a stable, prominence-like condensation is a dipped geometry in the loop. With an adaptive grid code, Antiochos et al. (1999) showed, in a 1D model, that the complete growth of a condensation reached a quasi-steady state after ≈ 5000 s. In a similar 1D setup, Xia et al. (2011) calculated the linear instability criterion from numerical results and proved that the onset of coronal condensation indeed satisfies the linear isochoric instability criterion (Parker, 1953). In the solar corona, the fairly high densities required for the instability onset are thought to be obtained by evaporating material with heating located near the footpoints of coronal loops in the chromosphere or by direct mass injection into the corona (Wang, 1999; Chae et al., 2001), resulting e.g. from nano-heating events.

Influenced by magnetohydrodynamic forces (gravity, Lorentz force and gas pressure gradients), condensations, once formed, either fall from the corona down to the chromosphere as coronal rain or they collect into larger structures and remain suspended in the corona over long time periods as prominences, supported by the magnetic field. Many numerical works addressed formation and dynamics of coronal rain, but adopted simplifying one-dimensional (1D) approximations reducing the problem to gas dynamic, thermodynamic evolutions along individual field lines

(Antiochos and Klimchuk, 1991; Schrijver, 2001; Karpen et al., 2001, 2005; Müller et al., 2003, 2004; de Groof et al., 2005; Karpen et al., 2006; Mendoza-Briceño et al., 2005; Antolin et al., 2010; Xia et al., 2011; Luna et al., 2012). Since coronal rain occurs in many active region loops, the heating input is generally thought to be concentrated at the loop footpoints (Antiochos and Klimchuk, 1991; Mendoza-Briceño et al., 2005), which evaporates chromospheric plasma into the loops and increases the density. With a persistent heating, the anisotropic thermal conduction and optically thin radiation lead these coronal hot loops to reach thermally unstable regimes with a higher density in a timescale of hours (Xia et al., 2011). Then catastrophic cooling sets in locally, resulting in the fast formation of cool condensations, as demonstrated in 1D models (Karpen et al., 2001; Müller et al., 2003; de Groof et al., 2005; Karpen et al., 2005). Numerical simulations by Müller et al. (2004) emphasized that a loss of equilibrium at the loop apex and the process of catastrophic cooling is caused by constant heating concentrated at the footpoints of the loop rather than a drastic decrease of the total loop heating which was used in earlier models. Müller et al. (2005) compared observations from an EIT shutterless campaign with simulations of coronal loops and confirmed that observed localized brightenings and fast flows are consistent with this model. An important conclusion from Antolin et al. (2010) was that the structure and dynamics of the coronal rain blobs are more sensitive to the pressure variations arising from catastrophic cooling than to gravity itself. This is in agreement with Schrijver (2001), who suggested that the internal pressure evolution of the loops, rather than gravity, determines the condensation speeds. Furthermore, Antolin et al. (2010) indicated that if a loop is predominantly heated by Alfvén waves, coronal rain is inhibited since they tend to heat the loop uniformly. Hence, coronal rain may not only point to the spatial distribution of the heating in coronal loops but also to the agent of the heating itself. They thus propose coronal rain as a marker for coronal heating mechanisms. Xia et al. (2011) pointed out that steady heating is not necessary to sustain the condensation. Once the condensation is formed, it keeps growing even after localized heating ceases. Luna et al. (2012) simulated a three-dimensional sheared double arcade with a large ensemble of 1D independent flux tubes and observed the formation of both prominence threads and coronal rain.

1.3.3 Footpoint heating

As we discuss above, the formation of thermal-instability usually involves a heating mechanism to evaporate the mass from the chromosphere into the corona. Parker (1988) suggested a corona heated by nanoflares uniformly distributed along braided and twisted coronal loops. However, in the last 10 years, observational evidence not only for uniform heating but also for footpoint heating (Aschwanden, 2001) has been found, thus generating a debate in the solar physics community. Footpoint heating in active region loops has received significant observational support in recent years. As stated previously, a significant number of loops is observed to be out of hydrostatic equilibrium (Aschwanden, 2001; Aschwanden and Tsiklauri, 2009), a state that is generally explained through footpoint heating.

A solution to this debate (uniform versus footpoint heating) seems to be that different families of coronal loops may exist in the Sun, as supported by recent studies of coronal loops (Ugarte-Urra et al., 2009). For instance, loops that are out of hydrostatic equilibrium seem to have in general temperatures below $2 - 3 \times 10^6$ K, and are thus denoted as warm loops. These show significant changes over relatively short timescales as compared to hot loops, which appear to be uniformly heated. Cool loops, with transition region temperatures, define a third branch of loops. Different lifetimes, dynamics and thermodynamic properties define each of these groups. Especially the coronal rain, being a direct manifestation of thermal non-equilibrium and of footpoint heating, can help estimate the importance of this mechanism in the solar corona.

1.4 Solar Flares

Solar flares are among the most explosive phenomena in the solar system, releasing up to 10^{32} ergs (10^{25} J) in hours or even minutes (Emslie et al., 2012) and in various forms such as radiative energy, kinetic bulk energy, thermal and non-thermal energy. They are intense bursts of electromagnetic radiation from the corona and are often associated with other events which include coronal mass ejections (CMEs), i.e. expulsions of vast volumes of plasma and magnetic field into the heliosphere, as well as solar energetic particles (SEPs), i.e. charged particles accelerated through the solar system to near relativistic speeds along open magnetic field lines. Because of their magnificent behaviour, flares have been one of the most fascinating scientific targets in solar physics since they were first observed in the 19th century. The spatial size of a flare depends on individual events; in the smallest event the height of a flaring loop is less than 10^4 km, whereas it reaches 10^5 km in the largest event. The size also affects the duration of a flare ($10^3 - 10^4$ s) and the amount of energy released during a flare mentioned above. A big flare known as a proton flare produces high-energy protons (> 10 MeV), and these high-energy particles travel through the interplanetary space to the Earth, having a huge impact on the polar region of the Earth (polar cap absorption, PCA). Predicting the occurrence of flares therefore becomes of great importance nowadays when human activity extends to space. This requires detailed investigations into the mechanism of such magnetically driven solar activity, and the nature of magnetic field transport via flux emergence into the solar atmosphere is key to a better understanding of the Sun-Earth system.

Flares are observed in a wide range of electromagnetic waves such as radio, visible light, X-rays, and gamma rays. Emissions in these wavelengths come from the atmospheric layers extending from the chromosphere to the corona. In the extreme case, even the photosphere responds to a big flare, observed as white-light brightenings. Also a flare produces high-energy particles which travel through the interplanetary space, sometimes having a severe impact on the environment of the Earth. The primary way of classifying a flare is via its soft X-ray (SXR) flux by GOES class (Thomas et al., 1985). This is based on the peak emission of the flare in the 1-8 Å channel of the Geostationary Operational Environmental Satellite X- Ray Sensor (GOES). The GOES class ranges from 10^{-8} to 10^{-4} W m^{-2} and a letter represents each dex, A, B,

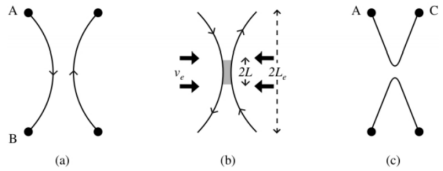

Figure 1.10: A simple diagram expression for magnetic reconnection. Credit: Scholarpedia.

C, M, and X, in ascending order. Each GOES class has ten times larger amount than the previous one. The letter is followed by a number which designates the coefficient. Thus an M3.7 flare has a peak flux of 3.7×10^{-5} W m^{-2}.

The majority of the radiative flare energy emerges at visible and ultraviolet wavelengths (Woods et al., 2006). Where a bolometric measurement is possible, i.e., in the most energetic flares, we find that the radiated optical luminosity is comparable to the kinetic energy of the coronal mass ejection, and also to the energy of the accelerated electrons as inferred from the hard X-radiation (HXR) (Fletcher et al., 2011) under the assumptions of the collisional thick-target model (Brown, 1971). A lot of emphasis has been placed on hard X-rays (HXRs) in understanding the flare energization process despite the fact that energetically, they represent only a small fraction of the total radiation. However, as HXRs result mainly from the well-understood bremsstrahlung radiation process, and the sources are optically thin, it is relatively straightforward to interpret them. The HXR emission is thus a powerful diagnostic for flare electrons, compared to longer wavelength, optically thick radiation, and the measurement of flare HXRs has been a primary goal of the Reuven Ramaty High Energy Solar Spectroscopic Imager (RHESSI). However, hard X-rays alone give only a restricted view of the overall configuration, development and energetics of a flare, and of its relationship to accompanying dynamical processes.

Solar flares are believed to be caused by magnetic reconnection, a process whereby stressed and sheared magnetic fields rapidly reorganise themselves into a lower energy configuration. Magnetic reconnection in flares is still not fully understood, despite numerous models and numerical simulations. However, many of the main aspects are common to most of the models as described in Fig 1.10. Magnetic reconnection occurs when oppositely directed magnetic field lines are arranged roughly anti-parallel with each other. Some models only require that the field lines be misaligned. This is called component reconnection. The efficiency of the reconnection then depends on the angle between the field lines, with the most efficient configuration being anti-parallel. In order for there to be a continuous gradient from positive to negative field strength, there must exist a region where the field is very small or zero. Normally the corona has a low plasma beta value which does not allow plasma to diffuse across magnetic field lines. However this very weak magnetic field strength creates a region of high plasma beta, known as the diffusion region. This is associated with a perpendicular current sheet due to the Lorentz force. The conditions in the diffusion region allow

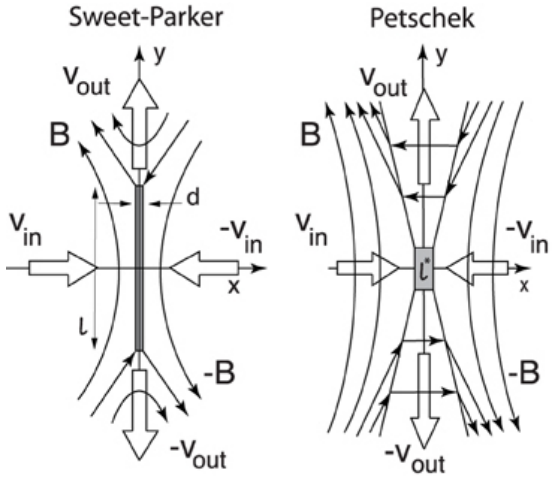

Figure 1.11: Schematic drawing showing the Sweet-Parker and Petschek model, highlighting the differences between them. From Shibata and Yokoyama (1999).

the magnetic field to reorient itself from, say, vertical opposing field lines to highly curved horizontal opposing field lines. The curvature of these field lines creates a high magnetic tension which accelerates the field lines and plasma away from the diffusion region. Thus magnetic energy is converted into kinetic energy which is believed to be capable of driving a solar flare.

Early attempts to model this process in 2D included the Sweet-Parker (Parker, 1953; Sweet, 1958) and Petschek (Petschek, 1964) models as shown in Fig 1.11. The Sweet-Parker model assumed a long thin diffusion region which however implied a too slow reconnection rate for flares. This problem was partially solved (Petschek, 1964) when slow magnetohydrodynamic (MHD) standing shock waves are introduced to the reconnection dynamics. Since then, the magnetic reconnection has been considered to be one of the promising mechanisms for producing a flare. Another promising ingredient for flare reconnection is that of tearing-modes (Kliem, 1994). A tearing-mode instability occurs when the diffusion region becomes too long. An instability occurs if the magnetic diffusion timescale is longer than that of the Alfvén transit time. Thus once an Alfvén disturbance occurs, magnetic diffusion cannot restore the system quickly enough and an instability is triggered. A coalescence instability then completes the task of reducing the current sheet by recombining these magnetic islands. This process liberates some of the free magnetic energy which then becomes available for driving a solar flare (Shibata and Yokoyama, 1999).

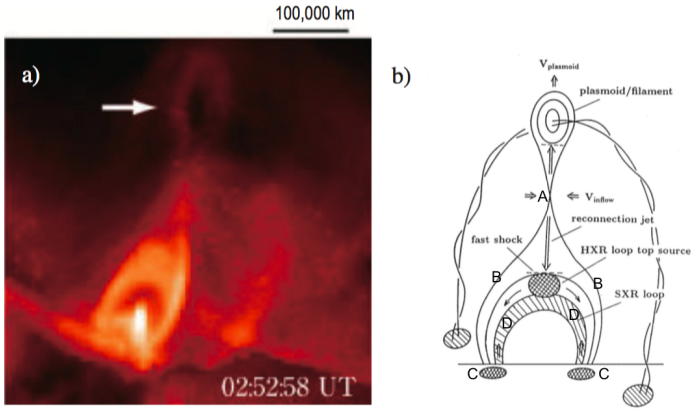

Figure 1.12: (a) Soft X-ray image of a long-durational-event (LDE) flare observed by Yohkoh. (b) Schematic picture of a modified version of the CSHKP model. (from Shibata et al., 1995)

1.4.1 The CSHKP Flare Model

The standard model of a solar flare is known as the CSHKP model after the authors of the principal studies upon which it is based (Carmichael, 1964; Sturrock, 1966; Hirayama, 1974; Kopp and Pneuman, 1976). These models assume more or less a similar configuration of magnetic field and its dynamic process, so these models are called with a single name, CSHKP model.

The basic characteristics and the processes of this model are illustrated in the right panel of Fig 1.12 along with an observational image obtained by Yohkoh in the left panel (Shibata and Yokoyama, 1999). The flare is assumed to be driven by a sizeable and sudden release of energy via magnetic reconnection. The energy release site can be seen marked as A. The topology illustrated in Fig 1.12 is highly simplified. In reality, this coronal loop may be part of an arcade of loops or may even be made up of a number of smaller entangled strands. As a result, the energy released may not be a single reconnection event but a rapid series of smaller events whose reconnection rate varies.

The energy release accelerates electrons and ions to near relativistic speeds. These accelerated particles spiral down along the magnetic field lines, emitting gyrosynchotron radio emission (B in Fig 1.12). This can cause direct heating of the coronal plasma via joule heating and shocks. However, due to the tenuous densities in the corona, most of the charged particles travel unhindered until they reach the transition region and chromosphere. These locations are called the footpoints (C in Fig 1.12). A small fraction ($\approx 10^{-5}$) of the accelerated particles undergoes bremsstrahlung, or braking radiation at the footpoints. This occurs via collisions between electrons and ions which

result in non-thermal hard X-ray (HXR) emission at the footpoints, naming the thick target model (Brown, 1971). Nevertheless the majority of the accelerated particles lose their energy via Coulomb collisions and heat the plasma around the footpoints to 10-40 MK high.

Once the chromospheric plasma has been heated by the accelerated particles, it conducts the gained heat to the cooler plasma below and leads to H_α footpoint brightenings. The rate of collisional heating from accelerated particles is so great that the footpoint plasma cannot radiate the energy away quickly enough to balance the temperature and the pressure. The overload pressure results in the expansion of the heated plasma rising back into the coronal loop where the pressure is much lower (D in Fig 1.12), which is known as chromospheric evaporation. Chromospheric evaporation can be classified into two categories: explosive one with upflows velocities of 200 km s^{-1} and gentle one with plasma upflow velocities of $10 - 100$ km s^{-1} (Milligan et al., 2006). Although normally the required heating for chromospheric evaporation is assumed from accelerated particle heating, Yokoyama and Shibata (1998) showed that it could be produced by thermal conduction front heating as well. Because the flaring plasma is at millions of Kelvin, it emits thermally at soft X-rays (SXR) and EUV (D in Fig 1.12).

1.5 Outline of the Thesis

From the previous sections it becomes evident that the detailed observations in the solar atmosphere of coronal phenomena (prominences, coronal rain, solar flares and so on) is a topic of great interest. However, the current theoretical models still need improvements in order to explain these coronal phenomena. The main aim of this thesis is trying to contribute to this theoretical model development. In this work we study the formation of coronal rain, the reflected waves and hard X-ray emission observed in solar flares by numerical simulations.

We first introduce, in Chapter 2, the equations of Magnetohydrodynamics, as well as their reasonable assumptions, which are the basis of coronal physics and will be useful in order to understand the different theoretical issues investigated in this thesis. Following in this chapter is the basic knowledge about computational magnetohydrodynamics. Then we briefly introduce the code we use in this thesis, MPI-AMRVAC and carry out a test run based on MPI-AMRVAC code.

In Chapter 3 we present the first 2.5D magnetohydrodynamic simulations which capture the initial formation and the long-term sustainment of the enigmatic coronal rain phenomenon. We demonstrate how thermal instability can induce a spectacular display of in-situ forming blob-like condensations which then start their intimate ballet on top of initially linear force-free arcades. We also present a preliminary result of our 3D simulation of coronal rain.

In Chapter 4, we perform a 2.5D magnetohydrodynamic simulation to imitate the chromospheric evaporation and the following reflected patterns in a flare loop. Quasi-

periodic propagating intensity disturbances have been observed in large coronal loops in EUV images over a decade, and are widely accepted to be slow magnetosonic waves. However, spectroscopic observations from Hinode/EIS revealed their association with persistent coronal upflows, making this interpretation debatable. We demonstrate that the quasi periodic propagating intensity variations captured by the synthesized *Solar Dynamics Observatory*/Atmospheric Imaging Assembly (AIA) 131, 94 Å emission images match the previous observations well.

In Chapter 5 we propose a model for the formation of loop-top hard X-ray (HXR) sources in solar flares through the Inverse Compton mechanism, scattering the surrounding soft X-ray (SXR) photons to higher energy HXR photons. We simulate the consequences of a flare-driven energy deposit in the upper chromosphere in the impulsive phase of single loop flares. We will investigate how the Kelvin-Helmholtz instability (KHI) is triggered by the chromosphere evaporation flows and introduce a possible method to generate HXR photons through the non-thermal particles accelerated and trapped by the KHI in the loop top.

A brief conclusion is drawn in Chapter 6 to depict the result of this thesis, as well as the expectation for the future development in MHD numerical simulations.

The differences between the models in Chapter 3, 4, and 5 include different magnetic field strengths and the most importantly heating terms. The different magnetic field strengths are used to model the different locations in the corona, e.g the quiescent regions in Chapter 3 with weak field and the active regions in Chapter 4 and 5 with strong field. The different heating terms express the different physical processes of the energy inputs. The continuous and gentle heating function in Chapter 3 is related to nano flare events, while the transient and explosive heating functions in Chapter 4 and 5 correspond to normal flare events.

Chapter 2

Magnetohydrodynamics and Numerical Methods

"Is it not pleasant to learn with a constant perseverance and application?"
—Confucius

The purpose of this thesis is to study coronal phenomena through numerical simulations, adopting a single fliud Magnetohydrodynamics (MHD) description. So this chapter begins with the introduction of the basic equations of the MHD system as well as briefly recall their assumptions. Following in this chapter, we introduce the basic knowledge about Computational Magnetohydrodynamics. Then we briefly introduce the code we use in this thesis, MPI-AMRVAC and carry out a test run for a solar prominence evolution.

2.1 The basic equations of Magnetohydrodynamics

The coronal temperature can heat the gas to gain energy beyond its atomic binding energy, and collisions strip off electrons from the atoms. However, freely moving electrons and ions may eventually recombine and become ionised again. The effects of these two competing processes cancel in equilibrium. An ionised gas is named a plasma if the free charges are so abundant that they can influence the properties of the plasma itself. The fraction of neutral atoms in equilibrium can be calculated through the Saha-Boltzmann ionisation equation, e.g. the ratio of ionised to neutral

atoms is around 2×10^{16} for a pure hydrogen plasma with density of 10^8 cm^{-3} at a temperature of 1 MK (10^6 K). These values are typical for the solar corona.

As the coronal dynamics is dominated by electromagnetic forces, the motion of any individual particle in the plasma is affected by the presence of the others. The macroscopic interaction between a medium in a plasma state and in the presence of a magnetic field is studied by Magnetohydrodynamics (MHD) which is a combination of electromagnetism and fluid mechanics.

2.1.1 Assumptions of the magnetohydrodynamic approximation

In the literature, the equations of this most extended physical theory are normally introduced from two different ways. The first one combines Boltzmann's kinetic theory and Maxwell's equations of electromagnetism to arrive at the basic MHD equations through several approximations and assumptions (see Goossens (2003)). The second method starts from the fundamental equations of fluid dynamics and combines them with Maxwell's equations, based on the assumption that a plasma is thought as a fluid consisting of charged and neutral particles, and permeated by electric and magnetic fields. The second approach is mathematically simpler and shorter. In this work we choose an intermediate way. We derive the basic MHD equations starting from the fundamental equations of fluid dynamics and electromagnetism as in Goedbloed and Poedts (2004); Goedbloed et al. (2010). We briefly summarize the fundamental assumptions made in order to derive the general equations to the final MHD expressions:

- The plasma is treated as a continuum which means that the length-scale of plasma processes is much larger than typical internal plasma lengths such as the ion gyroradius.
- The plasma is assumed to be in thermodynamic equilibrium. This means that the typical time-scales and length-scales are much larger than the collision time and the mean free path of particles, respectively.
- The plasma is treated as a single fluid. Global plasma properties are considered, which are computed as the sum of the magnitudes of each species (i.e., ions, electrons, and neutrals). In the derivation of global plasma properties, all remaining terms related with a single species are neglected based on several physical arguments.
- The equations are written in an inertial frame and relativistic effects are neglected because typical plasma velocities in the solar corona are much smaller than the speed of light.

As far as the solar corona is concerned, these assumptions are well chosen and in general sufficiently satisfied. However, one can ask why should a modern theoretical physicist be interested in ideal MHD? No quantum effects are taken into account,

neither are relativistic corrections considered, kinetic effects are removed and finally the neglect of the displacement current even removes electromagnetic waves from the system. All interesting modern physics seems to have been removed from the system so that we wind up with a derived field that could have been studied more than 137 years ago. So why then do we use MHD theory? Goossens (2003) gives three reasons:

- MHD respects the main physical conservation laws. Ideal MHD respects the conservation of mass, momentum, magnetic flux and energy.
- MHD has a decent mathematical structure.
- MHD is the simplest relevant theory available. It permits an in-depth analysis of various situations. Specifically, it is possible to study the plasma behaviour in finite geometries by supplying the equations with proper boundary conditions.

The MHD equations are different from the fluid dynamics equations since the extra magnetic field introduces several distinguished effects:

- It exerts a force which may guide plasma motions.
- It stores energy which may be released in solar flares.
- Due to the presence of magnetic fields, some of the plasma properties are highly anisotropic which means that it channels heat and thermally insulates the plasma.
- It provides support and stability in coronal loops, prominences and sunspots.
- Finally, it is elastic and so can support the propagation of magnetic waves, which is the main point of this Thesis.

2.1.2 Electromagnetic equations

The magnetohydrodynamic equations describe the motion of an ionised fluid interacting with a magnetic field. Hence, to derive these equations we need to combine Maxwell's equations with the equations of gas dynamics and equations describing that interaction. First, consider Maxwell's equations describing the evolution of the electric field $\mathbf{E}$(r,t) and the magnetic field $\mathbf{B}$(r,t) in response to the presence of electric currents with density $\mathbf{j}$(r,t) and electric charges, with density ρ_c(r,t),

$$\nabla \times \mathbf{E} = -\frac{\partial \mathbf{B}}{\partial t} \tag{2.1}$$

$$\nabla \times \mathbf{B} = \mu \mathbf{j} + \frac{1}{c^2}\frac{\partial \mathbf{E}}{\partial t} \tag{2.2}$$

$$\nabla \cdot \mathbf{E} = \frac{1}{\epsilon}\rho_c \tag{2.3}$$

$$\nabla \cdot \mathbf{B} = 0 \tag{2.4}$$

If we assume that l is a typical length for plasma variations and τ is a temporal scale, the typical velocity is then $v = l/\tau$. Hence we have $|\nabla \times \mathbf{E}| \sim E/l$, and $|\partial \mathbf{B}/\partial t| \sim B/\tau$.

After inserting these two relations into Eq. (2.1) we obtain $E = (l/\tau)B = vB$. Now apply to second term in the right of Ampére's law (2.2),

$$\frac{1}{c^2}\left|\frac{\partial \mathbf{E}}{\partial t}\right| \sim \frac{1}{c^2}\frac{E}{\tau} = \frac{v}{c^2}\frac{B}{\tau} = \frac{vl}{c^2\tau}\frac{B}{l} = \frac{v^2}{c^2}\frac{B}{l}$$

This means that in the limit $v^2 \ll c^2$ (non-relativistic velocities, as usually happens in the corona) the displacement current can be neglected. This approximation eliminates electromagnetic waves from the MHD equations.

The last electromagnetic equation is Ohm's law,

$$\mathbf{j} = \sigma\left(\mathbf{E} + \mathbf{v} \times \mathbf{B}\right) \tag{2.5}$$

where σ is the electrical conductivity. Ohm's law provides a link between the electromagnetic equations and the plasma fluid equations. In the MHD approximation it is used together with Ampére's law (Eq.(2.2) with the displacement current neglected) to lead to the induction equation,

$$\frac{\partial \mathbf{B}}{\partial t} = \nabla \times (\mathbf{v} \times \mathbf{B}) + \eta \nabla^2 \mathbf{B} \tag{2.6}$$

where $\eta = 1/(\mu\sigma)$ is the magnetic diffusivity, assumed constant. The ratio of the first to the second term in the right-hand side of the induction equation is, in order of magnitude, the magnetic Reynolds number, given by $\mathrm{R_m} = (vl)/\eta$. In typical coronal conditions we find $\mathrm{R_m} = 10^{14}$ and so the second term on the right-hand side of Eq. (2.6) is completely negligible and the situation is that of a perfectly conducting plasma. So we adopt $\eta = 0$ for the non-resistive ideal MHD.

Under such conditions the magnetic field lines behave as if they move with the plasma (Alfvén frozen-flux theorem). The induction equation determines the magnetic field once the velocity is known. In electromagnetism the electric current and electric field are primary variables and the magnetic field is a secondary variable produced by currents, but in MHD, the reserve is the case.

2.1.3 Fluid equations

We next consider the gas dynamic equations for the evolution of the mass density ρ and the pressure p. The first equation is mass continuity,

$$\frac{\partial \rho}{\partial t} + \nabla \cdot (\rho \mathbf{v}) = 0, \tag{2.7}$$

In the presence of a magnetic field, the total energy density can be written in the form

$$E = \frac{p}{\gamma - 1} + \frac{\rho v^2}{2} + \frac{\mathbf{B}^2}{2\mu} \tag{2.8}$$

and the total pressure is expressed as

$$p_{tot} = p + \frac{\mathbf{B}^2}{2\mu}. \tag{2.9}$$

Finally, the equation of motion for a fluid element, expressing conservation of momentum is

$$\rho(\frac{\partial}{\partial t} + \mathbf{v}\cdot\nabla)\mathbf{v} = -\nabla p + \mathbf{F} \tag{2.10}$$

The extra force, $\mathbf{F}$, consists of several terms whose relative importance depends on the particular situation being modelled. In a magnetised plasma such as in the solar corona, the dominant term is the Lorentz force, $\mathbf{j}\times\mathbf{B}$, which represents the force per unit volume exerted by the magnetic field upon the plasma. Replacing $\mathbf{j}$ from Eq. (2.2) the Lorentz force can be rewritten as

$$\mathbf{j}\times\mathbf{B} = (\mathbf{B}\cdot\nabla)\frac{\mathbf{B}}{\mu} - \nabla\left(\frac{B^2}{2\mu}\right), \tag{2.11}$$

In addition to the Lorentz force, the gravitational force, $\rho\mathbf{g}$, is frequently included in the equation of motion as well as a viscous force. On the contrary, the electric force can be neglected in comparison to the magnetic Lorentz force, as it is shown by the following dimensional analysis,

$$\frac{\rho_c E}{jB} \sim \frac{E^2\epsilon}{l}\frac{\mu l}{B^2} = \frac{\mu\epsilon E^2}{B^2} = \frac{v^2}{c^2} \ll 1.$$

Here we neglect the viscous force and the equation of motion becomes

$$\rho(\frac{\partial}{\partial t} + \mathbf{v}\cdot\nabla)\mathbf{v} = -\nabla p + (\mathbf{B}\cdot\nabla)\frac{\mathbf{B}}{\mu} - \nabla\left(\frac{B^2}{2\mu}\right) + \rho\mathbf{g}. \tag{2.12}$$

2.1.4 Summary of MHD equations

For most applications the MHD equations are taken as inviscid and include the effect of the gravity. The equations can be expressed in various mathematical forms, and the conservative form is preferred in the numerical models. Eq.(2.6), (2.7), and (2.12) are explicitly representing the conversation of mass, momentum, and energy. We adopt $\rho, \rho\mathbf{v}$, E, and $\mathbf{B}$ as the conservative variables in the form of the non-resistive MHD equations in conservative form as

$$\frac{\partial\rho}{\partial t} + \nabla\cdot(\rho\mathbf{v}) = 0, \tag{2.13}$$

$$\frac{\partial(\rho\mathbf{v})}{\partial t} + \nabla\cdot\left(\rho\mathbf{v}\mathbf{v} + p_{tot}\mathbf{I} - \frac{\mathbf{B}\mathbf{B}}{\mu}\right) = \rho\mathbf{g}, \tag{2.14}$$

$$\frac{\partial E}{\partial t} + \nabla\cdot\left(E\mathbf{v} + p_{tot}\mathbf{v} - \frac{\mathbf{v}\cdot\mathbf{B}}{\mu}\mathbf{B}\right) = \rho\mathbf{g}\cdot\mathbf{v} + L, \tag{2.15}$$

$$\frac{\partial\mathbf{B}}{\partial t} + \nabla\cdot(\mathbf{v}\mathbf{B} - \mathbf{B}\mathbf{v}) = 0, \tag{2.16}$$

with the rest equations as

$$E = \frac{p}{\gamma - 1} + \frac{\rho v^2}{2} + \frac{\mathbf{B}^2}{2\mu} \tag{2.17}$$

$$p = \frac{\rho}{\tilde{\mu}} RT, \tag{2.18}$$

$$\nabla \cdot \mathbf{B} = 0 \tag{2.19}$$

there L is the total energy loss function, γ is the ratio of specific heats, which is normally taken as $5/3$, R is the gas constant, T the plasma temperature and $\tilde{\mu}$ is the mean atomic weight (the average mass per particle in units of the proton mass). For a fully-ionised H plasma $\tilde{\mu} = 0.5$. The energy loss function has different terms which represent the rate of energy loss or gain. Heat flux due to particle conduction, radiation or ohmic dissipation and any other sources or sinks are included in the energy loss function.

In conclusion, magnetohydrodynamics, based on the principles of Maxwell and Lorentz, provides the basis for understanding the large-scale, slow dynamics of plasma in the solar corona.

2.2 Computational Magnetohydrodynamics

In astronomy, observers basically cannot influence the observed object by means of experiments. Analytical calculations and numerical simulations provide an excellent substitute for experiments. Due to the complexity of reality, the analytical method only can be used for limited cases with numerous approximations. Although, similarly the numerical simulations have their limitations as well, they still provide a complementary way to a deeper understanding of the physics behind observed phenomena.

Numerical simulations sometimes turn out to be more efficient and less expensive in cases where experiments can be done, e.g. the wind tunnel experiments in aerospace engineering. With the development of computer industries, the software and hardware for numerical simulations have been greatly improved in the last century. This significant progress provides the possibility to explore three-dimensional MHD simulations which require significant memory and CPU resources. In this section, we introduce the basic concepts of the numerical simulations, which are used in this thesis.

The following list is part of a method list used in the script of MPI-AMRVAC we use in the following chapters.

```
typeadvance= 'threestep'
typefull1= 'hllc'
typelimiter1= 'cada3'
coolcurve='JCcorona'
conduction=.true.
```

We are going to explain them one by one.

2.2.1 Time Integration

The array 'typeadvance' defines the procedure of the time integration and the one we use , 'threestep', is a third order Runge-Kutta type method. The Runge-Kutta methods are a family of implicit and explicit iterative methods, which includes the well-known routine called the Euler Methods, used in temporal discretization. These methods were developed around 1900 by the German mathematicians C. Runge and M. W. Kutta. The most widely known member of the Runge-Kutta family is generally referred to as "RK4", which is also implemented in MPI-AMRVAC. However, we use a slightly simple version RK3 (called 'threestep' here), as it can satisfy our needs and more importantly, saves the computing resources. RK3 is described as:

$$y = f(t)$$

$$\frac{\partial y}{\partial t} = g(t, y)$$

then

$$y_{i+1} = y_i + \frac{1}{6}(k_1 + 4k_2 + k_3)\Delta t$$

where

$$k_1 = g(t_i, y_i)$$

$$k_2 = g(t_i + \frac{1}{2}\Delta t, y_i + \frac{1}{2}k_1\Delta t)$$

$$k_3 = g(t_i + \Delta t, y_i - k_1\Delta t + 2k_2\Delta t)$$

The Taylor series expansion of RK3 is

$$y(t + \Delta t) = y(t) + \frac{1}{6}(k_1 + 4k_2 + k_3)\Delta t + o(\Delta t^4) \tag{2.20}$$

where $o(\Delta t^4)$ is the error term.

2.2.2 Spatial Discretization

The array 'typefull1' defines a spatial discretization method used for the time integration per activated grid level. A system of conservation laws like Eq.(2.13 - 2.16) with extra source terms can be written as

$$\partial_t \mathbf{U} + \partial_i \mathbf{F}_i(\mathbf{U}) = \mathbf{S(U)} \tag{2.21}$$

where $\mathbf{U}, \mathbf{F}_i$ and $\mathbf{S(U)}$ represents the conservative variables ($\rho, \rho\mathbf{v}$, E, and $\mathbf{B}$), the fluxes, and the source terms ($\rho\mathbf{g}, \rho\mathbf{g} \cdot \mathbf{v}$ and L) respectively. ∂_i means the spatial derivative in direction i and a summation over $i = 1, 2, 3$. We will give a quick overview of spatial discretization methods used in this thesis.

Total Variation Diminishing Type Schemes

The first spatial discretization method is called Total Variation Diminishing Type Schemes (TVD). Some of the most popular methods for solving a hyperbolic system of PDE are total variation diminishing (TVD) type numerical schemes. For a linear system of hyperbolic equations or for a single non-linear hyperbolic PDE, the total variation of the analytical solution

$$TV(U) = \sup \sum_{j=1}^{N-1} |U(x_{j+1}) - U(x_j)| \tag{2.22}$$

does not increase in time. The aim of the total variation diminishing (TVD) schemes is to ensure that the supremum in Eq.(2.22) does not increase with time, hence

$$\sum_j |U_{j+1}^{n+1} - U_j^{n+1}| \leq \sum_j |U_{j+1}^n - U_j^n|. \tag{2.23}$$

Although the MHD equations described in Sec 2.1.4 are a non-linear set of PDEs, many method based on TVD are found. These schemes behave well near discontinuities and are designed to suppress spurious oscillations. The disadvantage of the TVD schemes is the spatially first order representation of smooth local maxima and minima. There are dozens of variants in the TVD family, we are going to introduce one of the simplest variants in the following.

Courant-Friedrichs-Lewy condition

Before we move to details of the schemes, firstly we introduce a concept, the Courant-Friedrichs-Lewy (CFL) condition. In explicit time stepping schemes, the CFL condition is a necessary condition for stability while solving partial differential equations (usually hyperbolic PDEs). It arises in the numerical analysis of explicit time integration schemes, when these are used for the numerical solution. As a consequence, the time step must be less than a certain time in many explicit time-marching computer simulations, otherwise the simulation will produce incorrect results. For the one-dimensional case, the CFL has the following form:

$$C = \frac{u\Delta t}{\Delta x} \leq C_{\max} \tag{2.24}$$

where the dimensionless number C is called the Courant number, u is the maximal physical wave speed, Δt is the time step and Δx is the length interval. The value of $C_{\max}$ changes with the method used to solve the discretised equation. When an explicit (time-marching) solver is used, then typically $C_{\max} = 1$.

TVD Lax-Friedrichs scheme

The first order Lax-Friedrichs scheme is the simplest one in the TVD family and it follows the conservation discretization as

$$U_j^{n+1} = U_j - \frac{\Delta t}{\Delta x}(F_{j+1/2} - F_{j-1/2}) + \frac{1}{2}(\Phi_{j+1/2} - \Phi_{j-1/2}) \tag{2.25}$$

$$F_{j+1/2} = \frac{F_j + F_{j+1}}{2}; \Phi_{j+1/2} = U_{j+1} - U_j$$

This TVD Lax-Friedrichs (TVDLF) scheme is conditionally stable for Courant number $C < 1$. Numerical diffusion is caused by the last two terms in Eq.(2.25), and in TVDLF we use the expression,

$$\Phi_{j+1/2} = \frac{\Delta t}{\Delta x} c_{j+1/2}^{\max}(U_{j+1} - U_j)$$

where the maximal physical wave speed adjusts it. The numerical term Φ can also be thought of as a one-sided upwinded difference formula to modify the centered flux difference formula.

Second order spatial accuracy of TVDLF can be achieved by implementing a linear approximation of the term U and F at the boundary $x_{j+1/2}$ from left and right cell center values as

$$U_{j+1/2}^L = U_{j+1/2}^n + \frac{1}{2}\Delta U_j^n$$

$$U_{j+1/2}^R = U_{j+1/2}^n - \frac{1}{2}\Delta U_{j+1}^n$$

$$F_{j+1/2} = \frac{F(U_{j+1/2}^L) + F(U_{j+1/2}^R)}{2}$$

$$\Phi_{j+1/2} = \frac{\Delta t}{\Delta x} c_{j+1/2}^{\max}(U_{j+1/2}^L - U_{j+1/2}^R)$$

where the limited slopes ΔU is used to limit the conservative variables and ensure the TVD property. Many limited slopes existed, and one of them named cada3 limiter is third-order-accurate limited reconstruction Čada and Torrilhon (2009). TVDLF has the advantage of not using a Riemann solver and is therefore quite fast for heavy 3D simulations. It does not produce spurious oscillations at shock front. It has the downside to be more diffusive than other TVD schemes.

2.2.3 HLL and HLLC

The HLL method (Harten-Lax-van Leer) uses further approximations than the TVDLF Toro et al. (1994). The physical fluxes compute as

$$F_{j+1/2}^{HLL} = \frac{\lambda_F^+ F(U_{j+1/2}^L) - \lambda_F^- F(U_{j+1/2}^R) + \epsilon^{HLL}\lambda^-\lambda^+(U_{j+1/2}^R - U_{j+1/2}^L)}{\lambda^+ - \lambda^-} \tag{2.26}$$

where λ^+ are the fastest wave speeds in both directions and ϵ^{HLL} is used to control parameter against dissipation. When $\lambda^+ = -\lambda^-$ this reduces to the previous TVDLF scheme. The HLL scheme can be further improved by introducing an intermediate state at the contact discontinuity as developed in (Meliani et al., 2008) resulting in the HLLC scheme, which we use in this thesis. HLLC is a mixed prescription between a diffusive TVDLF and contact-resolving HLL.

2.2.4 Radiative Losses Of Solar Coronal Plasmas

The radiative cooling, or radiative loss, of the solar coronal plasma is an important quantity in solar physics as it is crucial in evaluating the plasma energy balance, especially considering the thermal instability mentioned in §1.3. In the coronal plasma with a temperature around MK, when radiative cooling dominates over heating, a density perturbation could lead to the onset of the thermal instability. To calculate the accurate radiative losses, we adapt the radiative losses table in Colgan et al. (2008) shown as the solid line in Fig 2.1. In their calculations, Colgan et al. (2008) used a complete and self-consistent atomic data set and an accurate atomic collisional rate over a wide temperature range. Below 10,000 K, we set $\Lambda(T)$ to vanish because the plasma there is optically thick.

At the start of the simulation, a subroutine called 'coolinit' reads in a cooling curve ($\log(\Lambda(T))$ and $\log(T)$), then transforms the data into a cooling table by a second order Lagrangian polynomial routine. Doing this interpolation in second order for a large number of points has the advantage that interpolation during the simulation can be done linearly without loss of accuracy. Another subroutine 'radcool' is called at each time step and could select the different methods you wish to use to calculate the cooling and calls the relevant subroutine. In this thesis, we use the exact integration method as introduced by Townsend (2009) to evaluate the radiative loss term. The exact integration method can be described by Eq.(2.27),

$$T_i^{n+1} = Y^{-1}[Y(T_i^n) + \frac{T_i^n}{T_{ref}} \frac{\Lambda(T_{ref})}{\Lambda(T_i^n)} \frac{\Delta t}{t_{cool}}] \tag{2.27}$$

$$Y(T) = \frac{\Lambda(T_{ref})}{T_{ref}} \int_T^{T_{ref}} \frac{\mathrm{d}T'}{\Lambda(T')} \tag{2.28}$$

$$t_{cool} = [\frac{(\gamma-1)\rho_i \mu \Lambda(T_i^n)}{k \mu_e \mu_H T_i^n}] \tag{2.29}$$

where T_{ref} is an arbitrary reference temperature; Eq.(2.28) is called the dimensionless 'temporal evolution function' (TEF) which represents a normalized measure of the total time taken to cool from T_{ref} to T; t_{cool} is the single-point cooling time; a monatomic gas ($\gamma = 5/3$) is assumed here and throughout.

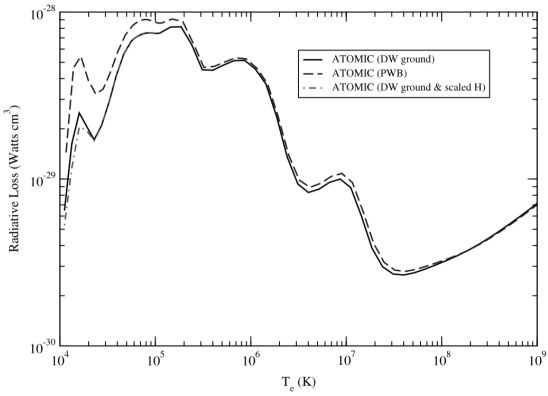

Figure 2.1: Radiative losses from a coronal plasma containing 15 elements from Colgan et al. (2008).

2.3 AMRVAC

The simulation code we are going to use in this thesis is MPI-AMRVAC. The original code, AMRVAC, was initiated in 2002 by Rony Keppens at Rijnhuizen and the MPI part was started in 2006 with Bart van der Holst at the Centre for Plasma-Astrophysics (CmPA) at KU Leuven. Afterwards, the code has been continuously improved by Zakaria Meliani and Oliver Porth, as well as Allard Jan van Marle, Peter Delmont, Chun Xia and others. MPI-AMRVAC is an MPI-parallelized Adaptive Mesh Refinement code and is able to advance partial differential equations by different numerical schemes which can handle discontinuities and smooth flows in shock-dominated problems with conservation laws.

MPI-AMRVAC is designed as a single versatile software with multiple options and switches for different problems (Keppens et al., 2012). This kind of general approach gives advantages as a reduction of overall time for software development, easier maintenance, compatibility of different parts, automatic extension of new features to all existing applications. Users are expected to understand how the different parameters change the behaviour of the code, and to be able to complete user written subroutines for source terms, special boundary conditions etc.

2.3.1 AMR

Here we briefly introduce the AMR features in MPI-AMRVAC (Keppens et al., 2012). MPI-AMRVAC adopts a standard block-based, octree AMR scheme. By fixing the refinement ratio to 2, we impose a gradual refined hierarchy of grid levels and use the same time step for all levels. We assume a hypothetical 2D domain of 4 by 3 blocks on level 1 as shown in Fig 2.2, in which local refinement is activated in 4 out of

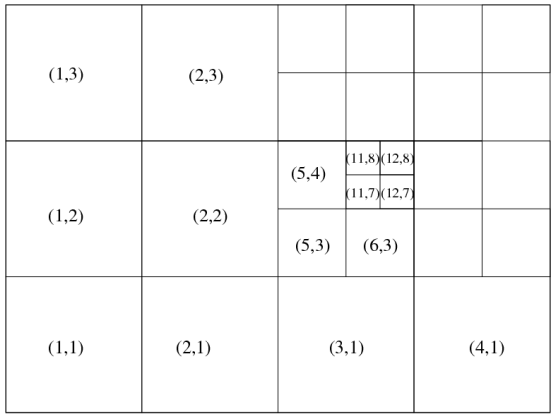

Figure 2.2: A generic AMR block skeleton (from homes.esat.kuleuven.be/ keppens/)

these level l=1 blocks in the top right domain corner, as well as in one level l=2 grid in the centre. The block-tree nature implies that a decision for refining/coarsening is to be made on a block-by-block basis. This automated block-based procedure of reconstruction of the grids takes 3 steps:

1 select all blocks at level 1< level < the maximal grid level;

2 in a certain grid block, quantify the local error at each gridpoint;

3 if any point has the local error exceeding a user-set level based tolerance, refine this block; if all points have their error below a user-set fraction of the level based tolerance, coarsen the block.

mxnest=6

nxlone1=128

nxlone2=80

The above list shows how to set up the parameter to control the AMR in the code. 'mxnest' means the maximal allowed lever, and 'nxlon21', 'nxlone2' shows the grid number at the level 1 in each direction. The grid number is divided in a number of blocks set by the user on the first level. Each block is in turn divided into a number of cells also defined by the user. This sets up the base resolution on our domain. In this example a domain of 8x5 blocks with 16x16 cells per block results in a base resolution on the first level of 128x80. The most evident way to increase the resolution is to augment the number of blocks in the domain, and/or the number of cells per block.

2.3.2 Test run: 2.5D Simulation of Prominence

Prominences, a common feature in active and quiet solar regions, represent huge structures of cold ($\approx 10^4$ K) and dense ($10^{10} - 10^{11}$cm^{-3}) plasma in the solar atmosphere (Tandberg-Hanssen, 1995). They are hosted by strong and complex dip-shaped magnetic field configurations, usually above the magnetic polarity inversion lines. However, the magnetic field topology of prominences is still poorly understood, although observations indicate it is mainly horizontal, with an acute angle with respect to the main axis of prominences (Bommier and Leroy, 1998). Prominences attracted plenty of theoretical studies to address different aspects of them, such as formation and eruption. Especially considering the formation of prominences, recently Xia et al. (2012) realized a 2.5D simulation of in situ formation of a filament in a sheared magnetic arcade, with chromospheric evaporation plus coronal condensation, using the MPI-parallelized Adaptive Mesh Refinement (AMR) Versatile Advection Code (Keppens et al. (2012)).

Here we present a test run and analysis. We follow the setup in Xia et al. (2012) as a 2.5D thermodynamic MHD model on a 2D domain of size 40 by 50 Mm (in $x - y$), but now adopt a linear force-free magnetic field characterized by a constant angle θ_0 (as in Fang et al. (2013)) as the initial magnetic field topology. The background heating rate decays exponentially with height, which helps to obtain a self-consistent thermally structured corona at first, and a relatively strong additional heating near the chromosphere injects energy and evaporates the plasma. We choose different angles ($\theta_0 = 30^\circ, 45^\circ$) for the initial linear force-free magnetic field topology. In the simulations, we regulate the energy input from additional chromospheric heating to reach the same value among the models with different angles. We also studied models with different magnetic field strength, different energy input heating scale and different spatial ranges of the additional chromospheric heating.

In the left panel of Fig 2.3, simulations of two representative models with different angles for the arcade magnetic field are compared, showing the evolution of the prominence mass. They indicate that after the appearance of cool plasma, an approximate linear relationship with time is found and the growth rates of the condensations in these models are similar. We infer this is because of the regulated same energy input from the additional chromospheric heating. By analyzing the growth rates of accumulated prominence mass in models with different parameters, we infer that these growth rates are basically determined by the energy input from additional chromospheric heating, although the time of formation and the heights of the first condensations can differ. Furthermore, by adopting different heating lengthscales and spatial ranges of the additional chromosphere heating with the same angle ($\theta_0 = 30^\circ$) of magnetic field topology, simulations still demonstrate that the growth of condensations display nearly linear relationship with time and positively correlate with total energy inputs from the additional heating. In models hosting different magnetic field strength, we did not find any obvious relationship between the growth rates of the condensations and the magnetic field strength.

Some of our modeled prominences develop additional internal structure, with the

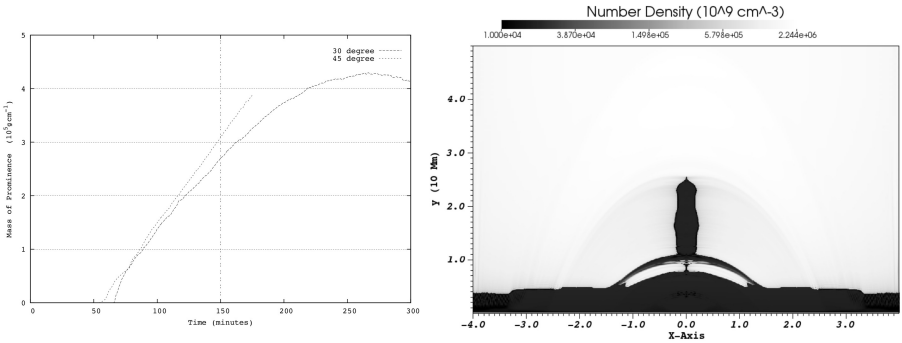

Figure 2.3: Left Panel: Temporal evolution of the prominence mass of models with two different angles of magnetic field. The vertical dashed line at t=150 min shows the moment when prominences begin to drag extra mass.; Right Panel: The density snapshot at t = 240 min.

side boundaries of the prominence resembling sawteeth, when the magnetic field of the arcade is strong. Indeed, when the lateral growing prominence can not bend the arched loops fast enough, segments of the prominence body residing in self-created magnetic dips fall down to the chromosphere along the arched loops. This drags extra mass from inside the magnetic dips to stream down until all prominence mass in the affected loops drains to the chromosphere. Consecutively, the evacuated loops reform condensations, and this phenomenon propagates from lower to higher loops. This realizes a down-streaming channel adjacent to an up-streaming channel, reforming the prominence as it rises, and we suggest these long-lived streams connecting the prominence and the chromosphere resemble the barbs of prominences (Fig 2.3, right panel). They also shed light on the mass recycling puzzle of prominences in general.

2.3.3 Convergence and Necessary Resource of the Simulations

One way to investigate the robustness of a code is testing the convergence of the simulations. In this section, we first present local box tests with different resolutions. Three rows of panels in Fig. 2.4 show the density maps of simulations at $t \approx 0$, 86, and 258 seconds. The two columns (left and right) mean two simulations with different resolutions, 14km for the left column and 3.5km for the right column. These simulations are 2D MHD models which are used to investigate the Kelvin-Helmholtz Instability. The top row shows the initial setup of the simulation areas. The central high density layer is assumed to have a wave configuration with a very small amplitude. The up and bottom layers with low densities have anti-parallel velocities. The second and third rows shows the consequent development of the Kelvin-Helmholtz Instability.

Table 2.1: CPUs Resources

Resolution (grid)	1024×640	2048×1280	4096×2560
CPUs Time (hour)	≈480 (4 nodes)	≈2200 (8 nodes)	≈13000 (128 nodes)

Fig. 2.4 indicates that the simulations with different resolutions show different details of the development of Kelvin-Helmholtz Instability. Although the low resolution run in the end shows numerical artifacts, no longer visible at the high resolution counterpart, both of them display the same physical phenomenon. In addition to Fig. 2.4, in Chapter 3, we run two simulations with different resolution (4 times higher in each directions), but we also get very similar physical results. This shows that the results of the numerical code converge for higher resolution. We have performed similar tests for the simulations in Chapter 3, 4 and 5. Tab. 2.1 shows CPU time consumption of the simulations with different resolutions in Chapter 3. We can find that the increment of the consumption is not linear, due to the increasing cost of communications between CPUs when the number of CPUs are large.

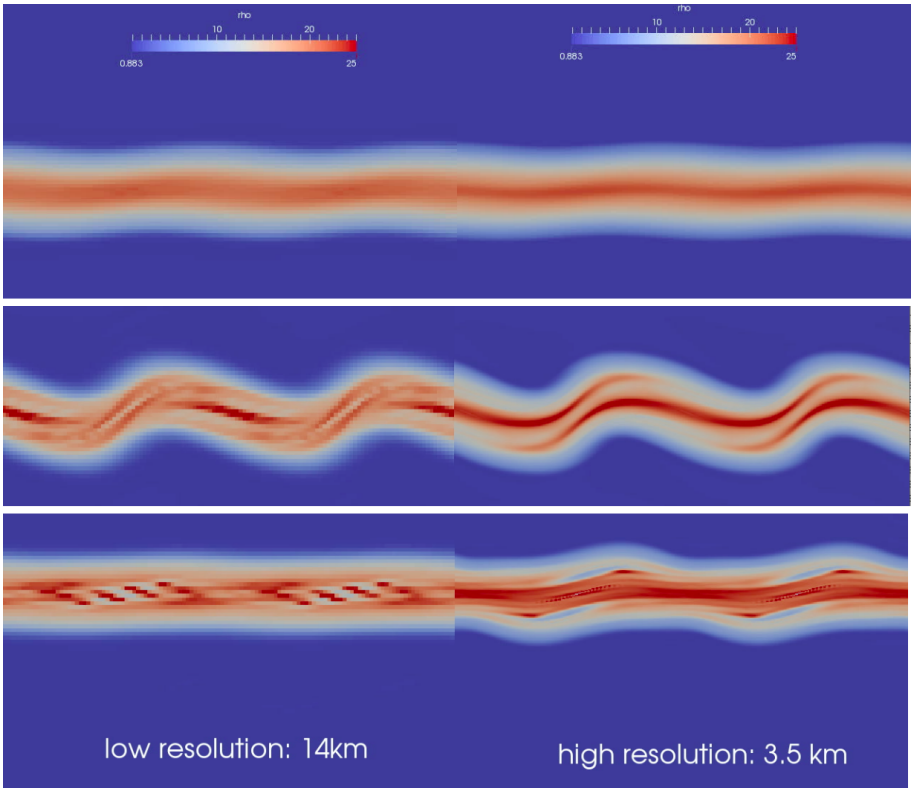

Figure 2.4: Local box tests of the Kelvin-Helmholtz Instability. The three rows show the density maps of the simulations at $t \approx 0$, 86, and 258 seconds. The two columns (left and right) display two simulations with different resolutions, 14km for the left column and 3.5km for right column.

Chapter 3

Modelling of Coronal Rain

"If the scholar be not grave, he will not call forth any veneration, and his learning will not be solid."

—Confucius

In this chapter we present the first 2.5 dimensional, magnetohydrodynamic simulations which capture the initial formation and the long-term sustainment of the enigmatic coronal rain phenomenon. We demonstrate how thermal instability can induce a spectacular display of in-situ forming blob-like condensations which then start their intimate ballet on top of initially linear force-free arcades. Our simulations pave the way for systematic surveys of coronal rain showers in true multidimensional settings, to connect parametrized heating prescriptions with rain statistics, ultimately allowing to quantify the coronal heating input. We also present a preliminary result of our 3D simulation of coronal rain. The results in this chapter appeared as Fang et al. (2013, 2015a). Unpublished results are discussed in §3.3.7 and §3.4.

3.1 Background

A recurrent finding in coronal loops is the coronal rain phenomenon, seen as intensity variations signaling cool blob-like downflows along the legs of loops (Kawaguchi, 1970; Leroy, 1972; Schrijver, 2001; O'Shea et al., 2007). Coronal rain forms part of the general phenomenon of thermal instability in a plasma, that takes place whenever radiative losses locally overcome the heating input (Parker, 1953; Field, 1965), and

is related to “catastrophic cooling" events (Schrijver, 2001). Meanwhile, numerical studies have significantly contributed to the understanding of these events, but typically adopted simplifying one-dimensional (1D) approximations meant to demonstrate the thermodynamic evolution along individual field lines (Goldsmith, 1971; Mok et al., 1990; Antiochos and Klimchuk, 1991; Antiochos et al., 1999; Xia et al., 2011). For coronal rain to occur in loops, the heating input is generally accepted to be concentrated at the loop footpoints. With footpoint heating, the loops rapidly get hotter and denser, due to evaporated chromospheric plasma invading the loops. The combined action of anisotropic thermal conduction and optically thin radiation causes these coronal hot loops to ultimately reach thermally unstable regimes on a timescale of hours. After that, “catastrophic cooling" sets in locally, leading to the rapid formation of condensations, as demonstrated in 1D models (Karpen et al., 2001; Müller et al., 2003, 2004, 2005; de Groof et al., 2005; Antolin et al., 2010; Xia et al., 2011).

From the observational side, the various stages of coronal rain formation have been analysed using *TRACE*, and were found to be recurring on timescales of days to weeks (Schrijver, 2001). Observations of coronal rain with *Hinode*/SOT have revealed a clear thread-like character in the coronal loops, and have started to provide statistical info on the number and velocities of blobs, while sizes reach down to the resolution limits (Antolin et al., 2010). High resolution instruments now reveal a scenario that coronal rain is a rather common phenomenon (Kamio et al., 2011; Antolin and Verwichte, 2011; Antolin and Rouppe van der Voort, 2012). The coronal rain can provide key info on the elusive coronal heating problem itself (Antolin et al., 2010). Realizing multi-dimensional numerical studies will be a prerequisite to unravel how coronal rain statistics encodes this heating input.

Recently, Fang et al. (2013) presented the first multidimensional, magnetohydrodynamic simulations which captured the initial formation and the long-term sustainment of the coronal rain phenomenon (§3.3.1 and §3.3.2). There we found that coronal rain in arcades is always accompanied by fast counter-streaming siphon flows in neighbouring flux bundles and we statistically analysed 80 minutes of virtual coronal rain in terms of sizes, mass, and velocity patterns. Our 2.5D simulations showed how blobs deform into V-shaped patterns, and levitate, evaporate in-situ, or fall into the transition region at speeds below free-fall. IRIS data recently revealed also many coronal rain impact events, with up to supersonic speeds above sunspots (Kleint et al., 2014).

We therefore revisited our MHD setup from Fang et al. (2013), at even further increased numerical resolution and for much longer time, going up to 6 hours in total (Fang et al., 2015a). We now analyse blob formation and blob impact into the transition region in more detail, focusing on multi-dimensional aspects not probed by 1D setups(§3.3.3 and §3.3.4). Furthermore, the High-resolution Coronal Imager (Hi-C) in July 2013 provided a much more detailed look at the fine structure and dynamics in the solar corona. With data from Hi-C, Alexander et al. (2013) reported that anti-parallel flows have been directly imaged along fundamental filament threads within the million degree corona. They measured relative flow velocities of similar magnitude as in our previous simulations, namely 70-80 km s^{-1}. Both observations and our simulations

hence suggest that such counter-streaming flows are likely commonplace. We observed that siphon flows establish naturally in a raining arcade, with velocity differences on adjacent field lines up to 80 km s^{-1} (§3.3.6 and §3.3.7). We thus also extended our simulations to further argue how our setup in a low field (order 12 G) magnetic arcade relates to the observed clumps of falling coronal rain (Antolin et al., 2010) and to unresolved fine-scale structure in solar coronal loop-tops (Scullion et al., 2014) (§3.3.5).

3.2 Numerical Setup of 2.5D Simulation

3.2.1 Governing Equations and Initial Setup

Our numerical setup is a 2.5D thermodynamic MHD simulation, which includes gravity, field-aligned heat conduction and radiative cooling and parametrized heating terms, on a rectangular plane with horizontal extension -40 Mm $\leq x \leq$ 40 Mm and vertical extension $0 \leq y \leq 50$ Mm. The governing equations are as follows:

$$\frac{\partial \rho}{\partial t} + \nabla \cdot (\rho \mathbf{v}) = 0, \tag{3.1}$$

$$\frac{\partial (\rho \mathbf{v})}{\partial t} + \nabla \cdot \left(\rho \mathbf{v}\mathbf{v} + p_{tot}\mathbf{I} - \frac{\mathbf{B}\mathbf{B}}{\mu_0} \right) = \rho \mathbf{g}, \tag{3.2}$$

$$\frac{\partial E}{\partial t} + \nabla \cdot \left(E\mathbf{v} + p_{tot}\mathbf{v} - \frac{\mathbf{v} \cdot \mathbf{B}}{\mu_0}\mathbf{B} \right) = \rho \mathbf{g} \cdot \mathbf{v} + \nabla \cdot (\vec{\kappa} \cdot \nabla T) - Q + H, \tag{3.3}$$

$$\frac{\partial \mathbf{B}}{\partial t} + \nabla \cdot (\mathbf{v}\mathbf{B} - \mathbf{B}\mathbf{v}) = 0, \tag{3.4}$$

where T, $\rho, \mathbf{B}, \mathbf{v}$, and $\mathbf{I}$ are respectively temperature, density, magnetic field, velocity, and unit tensor, with the ratio of specific heats γ=5/3, and a total energy density as $E = p/(\gamma - 1) + \rho v^2/2 + B^2/2\mu_0$; $p_{tot} \equiv p + B^2/2\mu_0$ is the total pressure, consisting of magnetic pressure and thermal pressure p; $\mathbf{g} = g_0 R_\odot^2/(R_\odot + y)^2 \hat{y}$ is the gravitational acceleration with the solar surface gravitational acceleration $g_0 = -274\,\mathrm{m/s^2}$ and the solar radius $R_\odot$; H and Q are respectively the heating and radiative loss rates; $\vec{\kappa}$ is the thermal conductivity tensor. Assuming a 10:1 abundance of hydrogen and helium of completely ionized plasma, we obtain $\rho = 1.4 m_\mathrm{p} n_\mathrm{H}$, where m_p is the proton mass and n_H is the number density of hydrogen. We use the ideal gas law $p = 2.3 n_\mathrm{H} k_\mathrm{B} T$, where k_B is the Boltzmann constant. We also adopt $Q = 1.2 n_\mathrm{H}^2 \Lambda(T)$ as the radiative cooling term, where $\Lambda(T)$ is the radiative loss function for optically thin emission, quantified by Colgan et al. (2008) using a recommended set of quiet-region element abundances, as used in previous work (Xia et al., 2011, 2012; Fang et al., 2013; Keppens and Xia, 2014). In calculations, Colgan et al. (2008) used a complete and self-consistent atomic data set and an accurate atomic collisional rate over a wide temperature range. Below 10,000 K, we set $\Lambda(T)$ to vanish because the plasma there is optically thick and no longer fully ionised. We use the exact integration method as introduced by Townsend (2009) to evaluate the radiative loss term as discussed in §2.2.4. The use of explicit,

(semi-)implicit, and exact integration methods in grid-adaptive simulations has been compared in van Marle et al. (2011). The term containing $\vec{\kappa} = \kappa_{||} \hat{\mathbf{b}} \hat{\mathbf{b}}$ quantifies the anisotropic thermal conduction along the magnetic field lines, composed by the unit vector $\hat{\mathbf{b}}$ along the magnetic field and the Spitzer conductivity $\kappa_{||}$ as $10^{-6} T^{5/2}$ erg cm^{-1} s^{-1} K$^{-3.5}$.

We employ a linear force-free magnetic field for the initial magnetic configuration, which is characterised by a constant angle θ_0 as follows:

$$B_x = -B_0 \cos\left(\frac{\pi x}{L_0}\right) \sin\theta_0 \exp\left(-\frac{\pi y \sin\theta_0}{L_0}\right) ,$$

$$B_y = B_0 \sin\left(\frac{\pi x}{L_0}\right) \exp\left(-\frac{\pi y \sin\theta_0}{L_0}\right) ,$$

$$B_z = -B_0 \cos\left(\frac{\pi x}{L_0}\right) \cos\theta_0 \exp\left(-\frac{\pi y \sin\theta_0}{L_0}\right) , \tag{3.5}$$

with $\theta_0 = 30^\circ$, the arcade makes a 30° angle with the neutral line ($x = 0, y = 0$). $L_0 = 80$ Mm is the horizontal size of our domain from -40 Mm to 40 Mm, and when adopting $B_0 = 12$ G, our magnetic arcade has a total box averaged field strength of 2.9 G.

For the initial thermal structure, we set a uniform temperature of 10000 K below a height of 2.7 Mm and choose a temperature profile with height ensuring a constant vertical thermal conduction flux (i.e., $\kappa \partial T/\partial y = 2 \times 10^5$ erg cm^{-2} s^{-1}) above this height, as also exploited by other authors (Fontenla et al., 1991; Mok et al., 2005). The initial density is then derived by assuming hydrostatic equilibrium with the number density of 1.2×10^{15} cm^{-3} at the bottom and the initial velocity field of all plasma is static. Since the corona needs to achieve a self-consistent thermal structure, we employ a background heating rate decaying exponentially with height into the whole system all the time,

$$H_0 = c_0 \exp\left(-\frac{y}{\lambda_0}\right) \tag{3.6}$$

where $c_0 = 10^{-4}$ erg cm^{-3} s^{-1} and $\lambda_0 = 50$ Mm. This heating is meant to balance the radiative losses and heat conduction related losses of the corona in its steady state. The small difference in heating scale height between 50 Mm in equation (3.6) above and 36 Mm in equation (2) in Fang et al. (2013) improves numerical stability at the top boundary and prevents it from cooling down during the longer timescale run performed here. With the above initial setup the whole system now is out of thermal equilibrium. We integrate the governing equations in time with heating $H = H_0$ active until the system achieves a quasi-equilibrium state. After 72 minutes, the above configuration reaches a quasi-equilibrium state shown in Fig. 3.1, which represents a 3D impression of the numerical box quantifying the temperature and number density profile and selected magnetic field lines. The $t = 0$ in Fig. 3.1 means that after reaching the quasi-equilibrium state, we reset the time of the system back to zero for the next stage of simulation. As seen in this Fig. 3.1, the numerical relaxation phase leads to some thermodynamic structuring in the final arcade. Some chromospheric plasma is quickly evaporated into coronal loops at the beginning of the relaxation, but this material gradually loses its kinetic energy. As a result, the final relaxed state

of the system is identified when the maximal residual velocity in the simulation is less than 5 km s^{-1}. In this end state, Fig. 3.1 shows a relatively thin transition region located at heights between 3 Mm and 5 Mm, which connects the chromosphere to corona. This transition region is higher above the neutral line, due to less downward thermal flux there because of the strong horizontal magnetic field. The plasma beta is 0.06 at 20 Mm height above the neutral line while the temperature and number density there are around 1.7 MK and $3.5 \times 10^8 \mathrm{cm}^{-3}$. The total mass (per unit length in the ignored dimension) of hot plasma in the corona is around 3.2×10^4 g cm^{-1}.

Following this equilibrated system, we turn on a relatively strong heating H_1. This extra heating is localized near footpoints in the chromosphere with formula as (Fang et al., 2013):

$$H_1 = \begin{cases} c_1 & \text{if} \quad y < y_c \quad \text{and} \quad A(x_1,0) < A(x,y) < A(x_2,0) \\ c_1 \exp(-(y-y_c)^2/\lambda^2) & \text{if} \quad y \geq y_c \quad \text{and} \quad A(x_1,0) < A(x,y) < A(x_2,0) \end{cases} \tag{3.7}$$

$$A(x,y) = \frac{B_0 L_0}{\pi} \cos\left(\frac{\pi x}{L_0}\right) \exp\left(-\frac{\pi y \sin\theta_0}{L_0}\right), \tag{3.8}$$

$$\lambda^2 = \frac{a\,(A(x,y) - A(x_2,0))}{A(x_2,0) - A(x_1,0)} + b \quad (\mathrm{Mm}^2), \tag{3.9}$$

where $c_1 = 10^{-2}$ erg cm^{-3} s^{-1}, $y_c = 3$ Mm, $x_1 = 26$ Mm, $x_2 = 14$ Mm, $a = 0.8$ Mm^2 and $b = 1.2$ Mm^2. This choice of strong base heating contrast ($c_1/c_0 = 100$) between H_1 and H_0 can mimic flare related chromospheric evaporation. However, this H_1 heating decreases with height to very small values and reaches one-tenth of H_0 heating at 10 Mm. As a result, the H_1 heating dominates heating in the chromosphere and the transition region, while the H_0 heating plays a more important role in the heating in the corona. The parameter $y_c = 3$ Mm represents the height of the transition region in the quasi-equilibrium system. $A(x,y)$ is the magnetic potential depending on the location and decaying exponentially with height into the whole system. Because the magnetic potential along a single magnetic field line is constant, we add extra heating at both feet of all magnetic field lines identified by $A(x,y)$ in the range of $x_1 < |x| < x_2$. Since catastrophic cooling is very sensitive to the heating decay scale and the length of magnetic field lines (Xia et al., 2011), the heating decay scale λ is set to larger values for longer field lines by the above formulae.

3.2.2 Discretization, AMR Settings and Boundary Treatment

We use the MPI-parallelized Adaptive Mesh Refinement (AMR) Versatile Advection Code *MPI-AMRVAC* (Keppens et al., 2012; Porth et al., 2014; Keppens and Porth, 2014) to run the simulation. Effective resolutions of 1024×640 and 4096×2560, or an equivalent spatial resolution of 80 km and 20 km in both directions are obtained through four or six AMR levels. The run with four AMR levels is studied in the following §3.3.1 and §3.3.2 and reports the results in Fang et al. (2013), and the one with six AMR levels is used for the rest of this chapter studying. This represents an effective fourfold improvement in resolution with respect to our earlier model (Fang

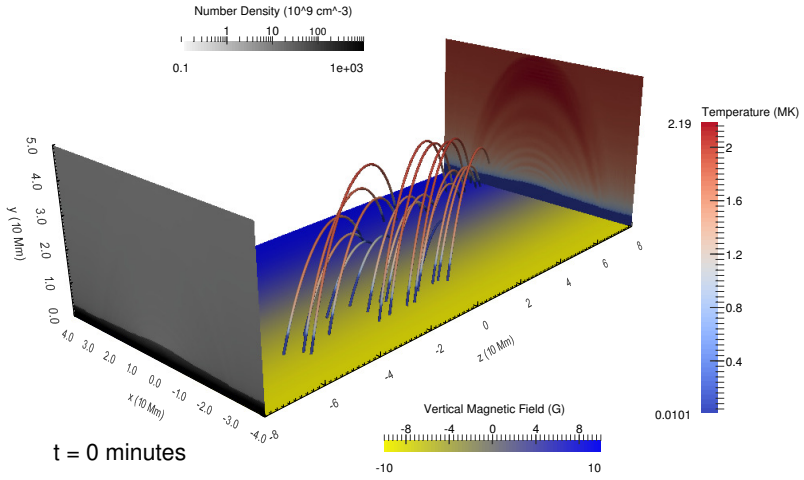

Figure 3.1: Around $t \approx 70$ minutes after relaxation, we show a 3D view on the quasi-equilibrium stage of our simulation, which serves as initial condition when extra localized heating is turned on. (the $t = 0$ minutes means the resetting of time to zero from now on.) The randomly selected field lines are colored by temperature, the back cross-section shows the temperature while the front $x - y$ cross-section shows the number density map.

et al., 2013). Our numerical strategy to advance the governing partial differential equations uses a three-step Runge-Kutta type scheme. For flux computations, a third-order-accurate limited reconstruction (Čada and Torrilhon, 2009) is introduced to calculate the variable evaluation from cell center to cell edge. We adopt a suitably mixed prescription between a diffusive total variation diminishing Lax-Friedrichs and contact-resolving Harten-Lax-van Leer with contact restored (HLLC) scheme (Meliani et al., 2008).

For boundary treatment, we employ 2 grid layers exterior to the domain as ghost cells to prescribe cell center values. Considering the left and right physical boundary, density, energy, y and z momentum components, B_y and B_z are set symmetrically, while v_x and B_x are adopted antisymmetrically to ensure zero face values. In bottom boundary ghost cells, we use the primitive variables $(\rho, \mathbf{v}, p, \mathbf{B})$ to set all velocity components antisymmetrically to enforce both no-flow-through (vertical) and no-slip (horizontal), while the $\mathbf{B}$ are fixed to the initial analytic expressions of equation (3.5), and the stratification of density is kept at pre-determined values from the initial

condition, as well as the pressure. We always resolve the bottom region up to $y = 0.5$ Mm at the maximal resolution. While for the top conditions, we set all velocity components as antisymmetric, and adopt a discrete pressure-density extrapolation from the top layer pressure with a maximal temperature $T_{top} = 2 \times 10^6$ K. For the magnetic field, we use a two-cell zero-gradient extrapolation to determine $\mathbf{B}$ in the ghost cells and improve B_y from a second order one-sided centered difference evaluation of $\nabla \cdot \mathbf{B} = 0$.

3.3 Results and Discussion

3.3.1 Coronal Rain Formation and Statistics

Because the heating formula for H_1 affects only a selection of loops fully contained interior to our simulation domain, this part of the arcade witnesses increased densities and temperatures, with maximum values of 2.1 MK after 9 minutes of added heating. Despite loop-aligned thermal conduction transporting energy to the dense coronal plasma around the apexes, temperatures then start to reduce slowly, while the densities still keep increasing. The locally heated arcade system continues to evolve, and only after about 100 minutes of sustained heating, the temperature at a height of 16.5 Mm suddenly declines drastically to 0.04 MK, slightly off-center. A small condensation segment with a density 5.6×10^{10} cm^{-3} suddenly comes forth around the apexes of a strand of magnetic loops. Figure 3.2 shows the velocity field, and the (signed) vertical total force with gravity, Lorentz force and pressure gradient in a zoomed view on the blob forming. The overall perturbed force field extends over 1 Mm in width, and has dominant about equal and in-phase pressure and Lorentz force contributions and induces field variations on neighboring fieldlines, which aid in triggering sympathetic condensations. Indeed, after this first localized condensation event, similar condensation processes continuously arise on both ends of the first condensation. Due to the broken symmetry, we observe this to extend into coronal loops on either side of the first affected loop strand, and this results into the larger scale condensation to look like a zigzag rope (like in panel (c) of Fig. 3.3). What happens next is a spectacular display of fragmenting, forming, relocating plasma blobs, since the cool plasma condensations spontaneously loose their balance between existing forces (gravity, magnetic, and gas pressure gradients), and start to slide down slowly along magnetic field lines. In movies, one can see how at about 118 minutes, the big zigzag condensation begins to split into several smaller blobs, descending along both rims of the magnetic field. After about 160 minutes, also due to the depletion of plasma in these loops, the subsequent phase seems less vigorous. Similar phases can be found in observations (Antolin et al., 2010; Antolin and Rouppe van der Voort, 2012), and are interpreted as 'limit cycles of loop evolution' by Müller et al. (2003).

Our simulation shows new features related to blob destruction. In particular, at 167 minutes, at a height of 10 Mm and horizontal position of $x = -21$ Mm, a small baby blob with a number density of 9.0×10^9 cm^{-3} and temperature 0.55 MK, forms in a

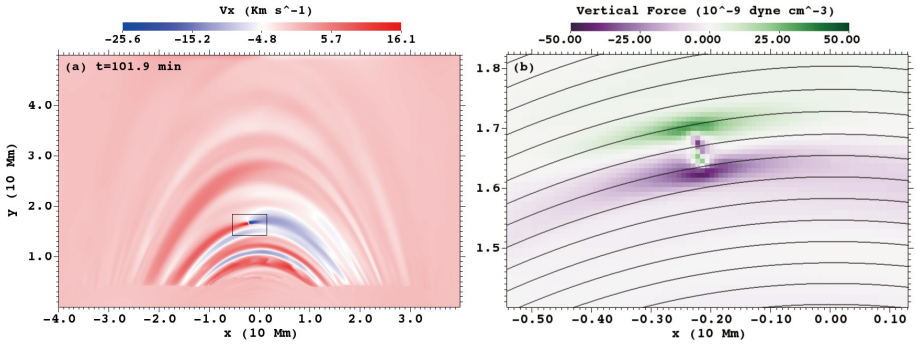

Figure 3.2: At $t \approx 100$ minutes, we show the x-velocity component at left. Right panel: zoomed view on the local signed vertical total force.

first slowly upflowing part of a strand of loops, where another bigger blob has just descended. This blob has an upward velocity of 10 km s^{-1}, but then gets destroyed by a hot inflow from the other side due to the heating-induced evaporation at the other loop footpoint.

At the overall effective resolution, any individual grid cell where the number density exceeds $7.0 \times 10^9 \mathrm{cm}^{-3}$, the temperature drops below 0.1 MK in the corona is labeled as in a coronal rain blob. These threshold values are suggested by observational findings (Hirayama, 1985) and other numerical simulations (Müller et al., 2005; Antolin et al., 2010). To count the instantaneous amount of blobs present at one time, we then identify the total number of blobs by assuming that all connected labeled pixels actually compose a single blob. In that way, we can report on the instantaneous amount of coronal rain blobs and the centroid (x_c, y_c) coordinates of each blob. The local magnetic field vector defines directions along and perpendicular to the field line. Along these directions, the length and width of the blob are quantified. However, since the resolution of our numerical simulation (78 km) is much higher than current observational resolutions, e.g., 150 km of CRISP (Antolin and Rouppe van der Voort, 2012), the number of identified blobs in the simulation is larger than that found in comparable observations. For the sake of direct comparison with the observations, we also do this at a resolution of 200 km. This operation combines neighboring blobs and occasionally overlooks blobs with sizes below this resolution.

Fig. 3.4(a) shows that the total mass of all blobs as function of time is nearly identical between the numerical resolution (dashed curve) and the observational resolution (solid curve), while the former slightly exceeds the latter. The difference between observations versus simulations is more pronounced in Fig. 3.4(b) showing the actual numbers of blobs. While actual blob numbers can go over 100 at certain times, still when viewing them with observational resolution as fewer (less than 20) blobs, the total mass basically remains the same between different resolutions. This means that while current coronal rain related mass estimates from observations are likely to be correct, there are still a great quantity of small unresolved blobs in present-day

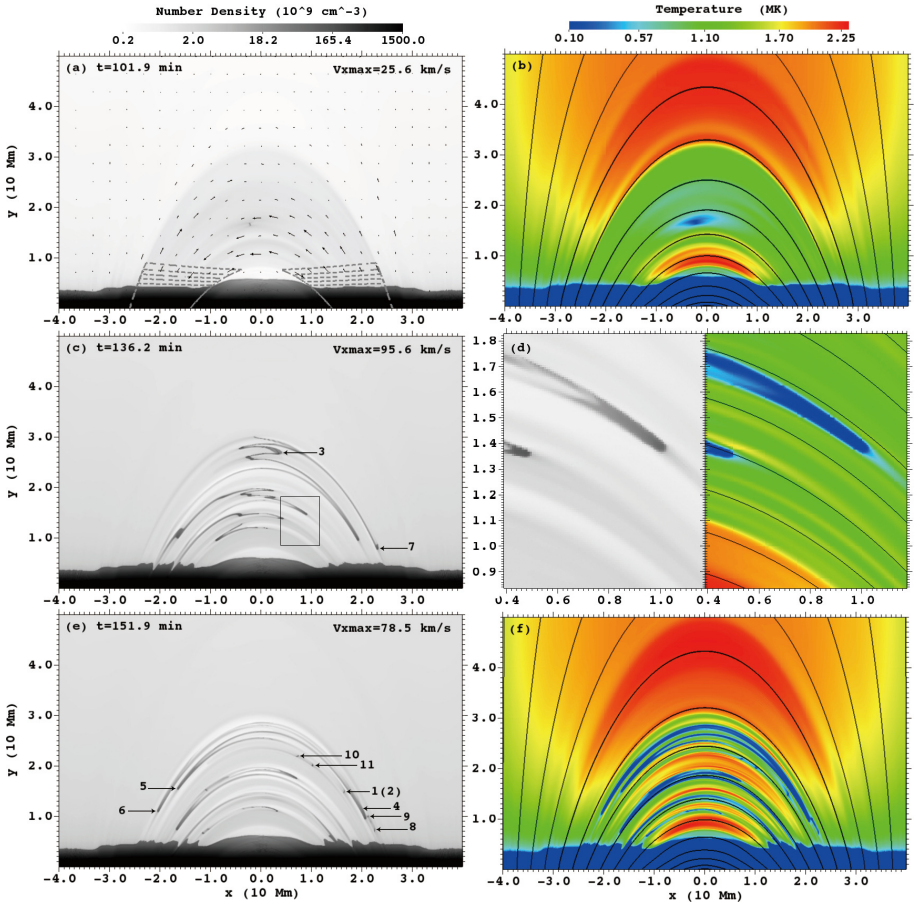

Figure 3.3: Snapshots at t=100 (first row), 136 (second row) and 152 minutes (third row). At left: density. At right: temperature and magnetic field lines. Localized heating is shown as contours in panel (a) and velocity arrows. Panel (d) shows the thermal stucture, zooming into blobs in panel (c).

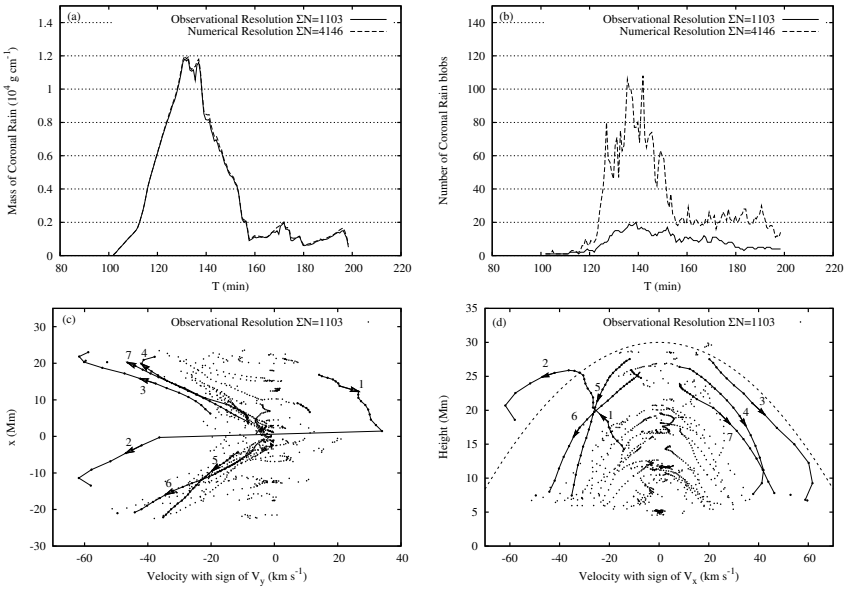

Figure 3.4: (a)Total mass versus time with numerical resolution (dashed curve) and observational resolution (solid curve); (b) number of blobs; (c) scatter plot of projected velocity with sign of v_y versus x-axis value; (d) scatter plot of projected velocity with sign of v_x versus height of blobs. The dashed curve denotes the path that a blob would follow if falling from a height of 30 Mm and subject to an acceleration of 0.18 km s^{-2}. All solid curves connecting points in (c) and (d) show the trace of several blobs, numbered from 1 to 7.

observations. After the first condensation seen at $t \approx 100$ minutes, Fig. 3.4(a) shows that in the next 29 minutes, still before the first descending blob crashes into the transition region, the mass accumulation of the blobs scales at a rapid rate of 6.7 g cm^{-1} s^{-1}. To quantify a true mass drain rate, we could adopt an average size in z of 400 km as the average width, making the mass drain rate about 3×10^9 g s^{-1}, very similar to observational results (Antolin and Rouppe van der Voort, 2012). Snapshots of density and temperature at times $t \approx 136$ and $t \approx 152$ minutes are shown in Fig. 3.3, where selected blobs are labeled by numbers, used in the further discussion.

A large variety of blob appearances are found during the whole coronal rain process. By treating every snapshot between $t \approx 100$ and $t \approx 200$ at a time interval of 43 seconds as an individual observation, we can easily obtain statistically meaningful distribution functions of blob width and length. This is quantified in Fig. 3.5 where we again contrast findings based on the numerical resolution with the observational resolution. The width of the blobs reveal the intrinsic cross section of a strand of

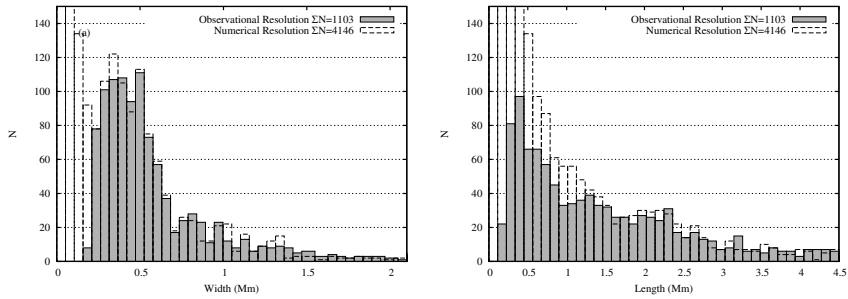

Figure 3.5: (a) and (b) show the distribution function of width and length, respectively, at numerical and observational resolution.

loops with nearly synchronous evolution. Recent results from triple-filter analysis of the finest coronal loops analyzed in TRACE images found elementary loop strands with isothermal cross sections of $\approx 1000 - 2000$ km (Aschwanden and Nightingale, 2005). Similar values of sympathetic loop strand widths can be seen in the horizontal velocity map in Fig. 3.2, are also seen in the perturbed force view and return in the distribution function of the obtained blob widths in panel (a) of Fig. 3.5. Although the width of such strands and blobs can reach the maximum value of 2000 km, these huge blobs will be separated during the propagation process into small fragments. This is again resulting from significant differences in the diverse forces acting along their body. The width histogram in Fig. 3.5(a) also shows that the vast majority of blobs possess widths like $\approx 200 - 1000$ km with an average 400 km, in direct correspondence with recent observational results from Antolin and Rouppe van der Voort (2012).

3.3.2 Dynamics of Blobs

The velocity structure at $t \approx 100$ minutes is shown in Fig. 3.2, at the same time as the density and temperature panels (a) and (b) of Fig. 3.3. In the velocity plot, one identifies the condensation where two strong opposite inflows with a maximum relative velocity of 68.7 km s^{-1} are siphoned towards the condensation site from both sides. This coincides with a dramatic evacuation of a loop strand caused by the catastrophic cooling. The thermodynamic evolution rapidly refills the local empty loops with hot and rarefied plasma. These fast inflows and the density variation they create, first realize a pressure difference across the two sides of the off-center blob, which levitates the newborn blob against gravity. This first phase impedes the descending process of newborn blobs. However, after a short time the inflows become slower, and while the blob density increases, this previous pressure difference gradually fades away. Therefore, they ultimately start to accelerate quickly downwards.

To explain how a full loop strand ultimately shows blobs that appear like comet-shaped or V-like features during propagation (Antolin et al., 2010; Antolin and Verwichte,

2011), we note that within a loop strand of finite extent (say few hundred km in width), a first small condensation functions like the seed for a larger blob. In this growth, the condensation process appears to extend from the first blob onwards due to the synchronous temperature evolution in a wider loop strand (Klimchuk et al., 2010). This means that while the firstly formed condensation may already have evolved beyond the phase where it experiences levitating pressure support, the condensation segments formed later at the edge of the blob are still locally supported against gravity by the pressure difference due to the fast siphon inflows. As a result, the large, growing blob gets deformed as a whole into a comet-shaped pattern, like the blobs labeled with numbers 3-7 of Fig. 3.3. During their propagation towards the arcade footpoints, catastrophic cooling further sets in in the tail of these blobs, and blobs will be elongated by continuously forming condensations on the way down. Furthermore, as the gravitational acceleration varies with height, an effect accounted for in our external y-stratified gravitational field, the blob will also become elongated due to being stretched by the differential component of gravity along the curved magnetic field. Therefore, the length histogram in panel (b) of Fig. 3.5 presents an average of 850 km for coronal rain blobs, but shows a wide range of lengths going from 200 km to exceeding 4500 km, a fact confirmed by observations (Schrijver, 2001; Antolin and Rouppe van der Voort, 2012). Zoomed views on selected blobs in Fig. 3.3 show the local temperature structure, with conduction-dominated regions around the blobs. The temperatures of these local transition regions are around 0.6 MK.

We obtain a broad distribution of projected velocities, ranging from few km s^{-1} to the high velocity of descending blobs going up to more than 60 km s^{-1}. Panel (c) of Fig. 3.4 shows a scatter plot of the horizontal centroid x_c-position of the blobs versus their in-plane projected velocity, signed by vertical velocity. This is done at the observational resolution, and in this view one can trace individual blobs appearing in multiple snapshots. Panel (d) of Fig. 3.4 shows a scatter plot of height y_c of the blobs versus their projected velocity, now signed with v_x. Since the velocities are generally height dependent, the dashed curve in panel (d) of Fig. 3.4 denotes the path that a blob would follow if it were falling from a height of 30 Mm, subject to an acceleration of 0.18 km s^{-2}, the average effective gravity for a loop whose height to half baseline ratio is 30 (Mm)/26 (Mm). We note that most of the measurements are located below the dashed curve, like those for blob 6 and 7. This scenario suggests a role for other forces than gravity, like gas pressure as suggested by previous 1D numerical simulations (Müller et al., 2003, 2004, 2005).

Close to the lower parts above the transition region of the arcade, strong deceleration of individual blobs is sometimes observed (Antolin and Rouppe van der Voort, 2012), which is explained by the increase of gas pressure there from the higher local densities. The solid lines connecting the points of individual blobs 3 and 4 in panels (c) and (d) of Fig. 3.4 show these strong decelerations happening right above the transition region. Decelerated by this pressure gradient, the leading descending blob part could be caught up by a later faster descending blob part (as in 1D studies from (Müller et al., 2005)) and merge to one heavier blob. At about 152 minutes, in panel (e) of Fig. 3.3, at a height of 7.1 Mm and horizontal position of $x = 22.5$ Mm, we find that in the trail of a formerly descending blob, a small blob (number 8) appears and

stays there supported by the large pressure gradient. Meanwhile, in the same strand, another blob (number 9) forms above the number 8 and moves towards it with velocity of 26 km s^{-1}. They collide, merge and produce a heavier blob, which finally falls down to the transition region 4 minutes later.

In panel (e) of Fig. 3.3, two blobs in the same flux loop strand, numbered 10 and 11, approach each other because of the significant pressure difference across them, as extremely low gas pressure is induced by catastrophic cooling in between them, and the gas pressure outside enforces their mutual approach. This kind of situation can even suck a blob upwards, ascending and crossing the apexes of loops, e.g. this is what happens to the blob number 1 in panel (e) of Fig. 3.3, which shares the same strand with blob number 5. In panels (c) and (d) of Fig. 3.4, the scatter velocity plots versus height and x-position show us this clearly when inspecting the traces of blob 1 and blob 5. When blob 5 descends to the footpoint, blob 1 is siphoned to ascend from the right rim and over to the left rim along the magnetic field lines.

3.3.3 Rebound Shocks and PCTR of Condensations

The forming process of the first condensation in our 2.5D simulation is shown by Fig. 3.6 which presents the temporal evolution of number density (left columns), temperature (middle columns) and gas pressure (right columns) at $t \approx 101.2$, 101.5 and 102.2 minutes. When we compare these results with the corresponding Fig. 5 and Fig. 7 of 1D hydrodynamic simulations in Xia et al. (2011), we conclude that all three parameters behave similarly in the forming process, as the number density increases rapidly from 10^8 cm^{-3} to 10^{10} cm^{-3}, while the temperature decreases down to 0.01 MK. Along each arched field line, this is analogous to the sudden thermal instability onset in 1D runs. This similarity confirms the applicability of restricted 1D model efforts which assume a rigid 1D loop under the prevailing plasma β conditions, which takes on a local value of around 0.06. The middle panel in the right column of Fig. 3.6 also shows a significantly increased gas pressure inside the condensation and a layer of low gas pressure surrounding it after its formation. In the bottom panels of Fig. 3.6, we notice that density, temperature and gas pressure all reveal a front propagating as expanding wings on both sides of the condensation. This phenomenon is because fast siphon inflows are driven into the forming condensation by a strong pressure gradient between the lower gas pressure around the condensation and relatively higher gas pressure away from the condensation, as seen in the middle panel in the right column of Fig. 3.6. These two siphon flows meet up with the blobs, and dynamically impact on the blob to generate two rebound shocks. Hence, while thermal instability and runaway cooling triggers a growing condensation, one also forms two rebound shock fronts that propagate away from the blob. The slightly different formation time at different parts of the condensation on adjacent magnetic field lines (Fang et al., 2013), which are due to gradual variations in length and chromospheric footpoint conditions, is the reason that these two expansion shock fronts display a fan-shaped structure, forming earliest in the blob center and spreading away from the blob. This fan-shaped structure of the rebound shocks is also clearly observed in Xia et al. (2012).

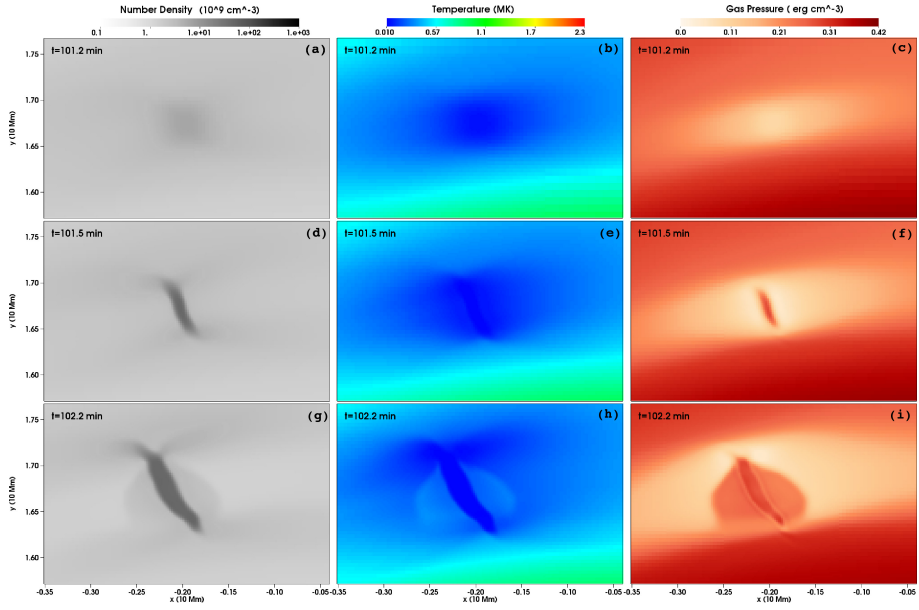

Figure 3.6: At $t \approx 101.2, 101.5$ and 102.2 minutes (top to bottom rows), we show the number density (left column), temperature (middle column) and gas pressure (right column) maps in a zoomed (about $3000 \times 2000\,\mathrm{km}^2$) area. This shows the formation process of the first condensation.

However, not every condensation realizes this nearly left-right symmetric situation as seen near the loop apex for this first condensation from Fig. 3.6. Due to slightly asymmetric conditions already prevailing after the numerical relaxation process and due to perturbations from existing condensations, most of the following condensations initiate in loop limbs (also shown in movies of Fang et al. 2013). The field-projected gravity force on the limbs leads to asymmetric plasma distributions, as seen e.g. in the number density map in panel a of Fig. 3.7 at $t \approx 113.3$ minutes, the moment when local catastrophic cooling begins there (about 10 minutes after the first condensation). The higher central gas pressure indicates the initial forming location of this condensation in panel b of Fig. 3.7. Due to its limb-loop location, the number density map points out that the right of the condensation holds a relatively denser (3×10^9 cm^{-3}) and wider plasma distribution than the left part (1.5×10^9 cm^{-3}). Still, strong pressure gradients drive siphon flows from both sides towards this condensation. After a short time at $t \approx 113.7$, the denser and heavier plasma at the right of this condensation realizes a (left-directed) siphon flow with a slower speed of 23 km/s, compared to the left siphon flow (which is right-directed) at a speed of 42 km/s, shown by the velocity magnitude map in panel c of Fig. 3.7. As discussed above, the impact of siphon flows on the condensation naturally generates rebound shocks, whose speeds are determined by the original speeds of the siphon flows and the mass contrast between the condensation

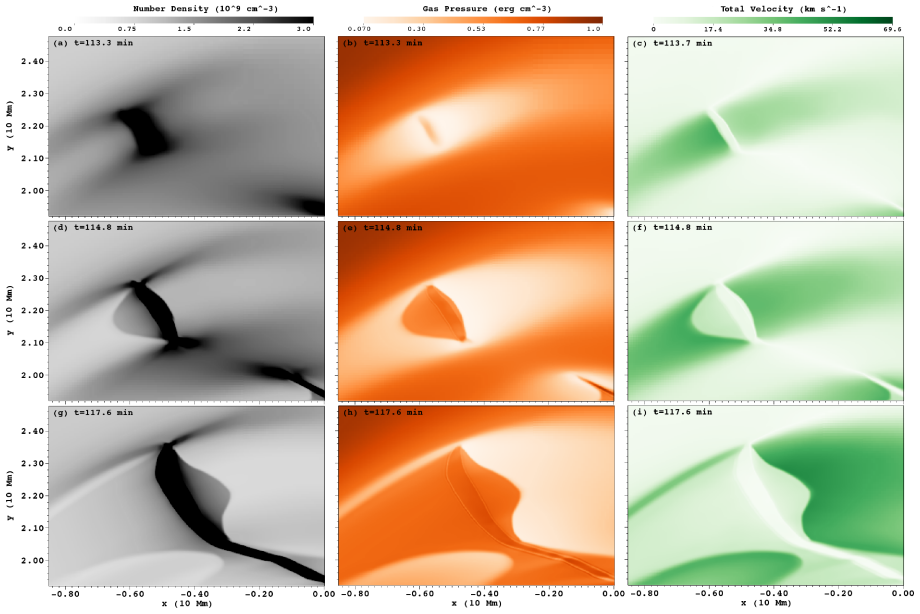

Figure 3.7: At $t \approx 113.3, 114.8$, and 117.6 minutes (top to bottom rows), we show evolutions of two-sided rebound shocks in number density (left column), gas pressure (middle column), and plasma velocity magnitude (right column) maps. The panel c shows the plasma velocity magnitude map at $t \approx 113.7$ minutes. This blob shows clear left-right asymmetric behaviour in its rebound shock pair pattern.

and the siphon flows. The slower and heavier siphon flow on the right of the blob here leads to a much slower rebound (right-directed) shock seen to separate at 7 km/s, while the left one (left-directed) travels at 21 km/s. These two rebound shocks are identifiable in the gas pressure map in panel e of Fig. 3.7 at $t \approx 114.8$ minutes. The condensation itself has a velocity of 5 km/s, meaning that basically the right rebound shock barely can sweep up and heat little siphon flow plasma. Because the central condensation keeps sucking in plasma from nearby and the rebound shock at the right of the blob is too slow to sweep and heat up plasma, the gas pressure there does not rise to a higher value and keeps a strong pressure gradient at the right of the blob, as shown in panel e of Fig. 3.7. About 3 minutes later at $t \approx 117.6$ minutes, this persistent pressure gradient at the right of the blob accelerates the left-directed siphon flow to a higher speed of 52 km/s (shown in panel i of Fig. 3.7), therefore the corresponding right-directed rebound shock finally speeds up to 28 km/s and begins to sweep and shock-heat the plasma on its way. In short, initial asymmetric situations on the condensation can lead to a complicated thermal and dynamical evolution and result in a delay of rebound shocks spreading at one side of the condensation.

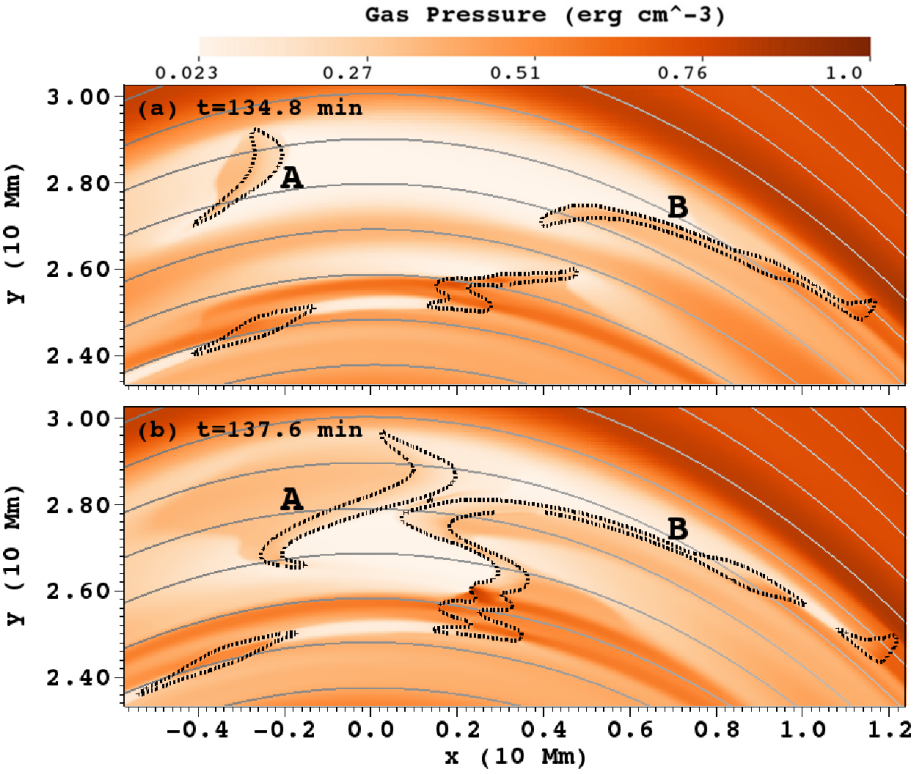

Figure 3.8: At $t \approx 134.8$ and 137.6 minutes, we show the gas pressure map (a) and (b) at times indicated, with a dotted isocontour of the number density at 7×10^9 cm^{-3}. The thin grey lines are magnetic field lines. There are two blobs A and B in the same loop, with consequences for the way siphon flows can induce or prevent rebound shock patterns.

Additionally, we also find another special case, namely blob A in Fig. 3.8, which has only one rebound shock on its left side. Fig. 3.8 shows the gas pressure map (a) and (b) at $t \approx 134.8$ and 137.6 minutes, with a dotted isocontour of the number density at 7×10^9 cm^{-3} overplotted. This density contour at 7×10^9 cm^{-3} is one of the criteria which identifies whether a cell contains cool plasma belonging to coronal rain, as used further on. Panel a in Fig. 3.8 indicates a similar situation for blob A as in the second row of Fig. 3.7 in which only the left rebound shock spreads out. In contrast to what happens in the third row of Fig. 3.7, for blob A we do not find a right rebound shock in Fig. 3.8 until the collision and merging of blob A with blob B. The reason is that when the thermal instability triggers the condensation labeled there as blob A, another existing condensation labeled as blob B in the same coronal loop already depleted the plasma between these two blobs. Therefore the small pressure gradient in the emptied loop between the two blobs can not drive a fast siphon flow to create a strong rebound shock for blob A, even though the gas pressure on the right of blob A is low enough (panel a in Fig. 3.8), Afterwards, when blob A catches up and merges with blob B because of the strong pressure gradient outside these two blobs, the rebound shock at the right side of blob A is still not fast enough to show clear separation and propagation.

We also observe the details of a gas pressure substructure within these shock-bounded regions around the condensation in the simulations. These reveal the establishment of a prominence-corona-transition-region (PCTR) like structure around all blobs. The gas pressure substructure around the first condensation consists of three components shown in panel a of Fig. 3.9 and panel i of Fig. 3.6, namely a high gas pressure outside of the condensation, a low gas pressure at the boundary of the condensation, and a higher gas pressure in the center of the condensation. Actually not only this first condensation in Fig. 3.6 has this kind of gas pressure substructure, but also all the blobs which establish a dynamic equilibrium around themselves have it, e.g. all the blobs in Fig. 3.7 and Fig. 3.8. To better quantify this, we identify a field line crossing the centre of the blob shown in panel a of Fig. 3.9 and plot gas pressure, temperature and radiative loss along this field line in panel c of Fig. 3.9. The temperature declines from a coronal temperature of 0.35 MK to a cool plasma temperature of 0.01 MK in 200 km and density increases from 1×10^8 cm^{-3} to 1×10^{10} cm^{-3}, therefore basically this 200 km area could be considered as a PCTR. Within this area, we find that two highly radiative loss peaks exist, introduced by a temperature around 0.02 MK. This corresponds to the two dips of gas pressure at the boundary of the blob. These two strong radiation areas also indicate the location in which catastrophic cooling takes place that ensure that the condensation keeps growing. Indeed, the two dips in gas pressure always relocate with the boundary of the blobs, coincident with the strong emissive loss. Although the temperature of 0.01 MK inside the blob is lower than in the surrounding coronal plasma, a much higher density at the center of the condensation (5×10^{10} cm^{-3}) leads to a little higher gas pressure there. The high gas pressure outside of the condensation reflects the post shock conditions prevailing there after the rebound shocks run against the condensation inflows. Note that our resolution is such that we have about 7 grid points along the field line through the PCTR at each side of the blob in Fig. 3.9, clearly resolving the PCTR around the

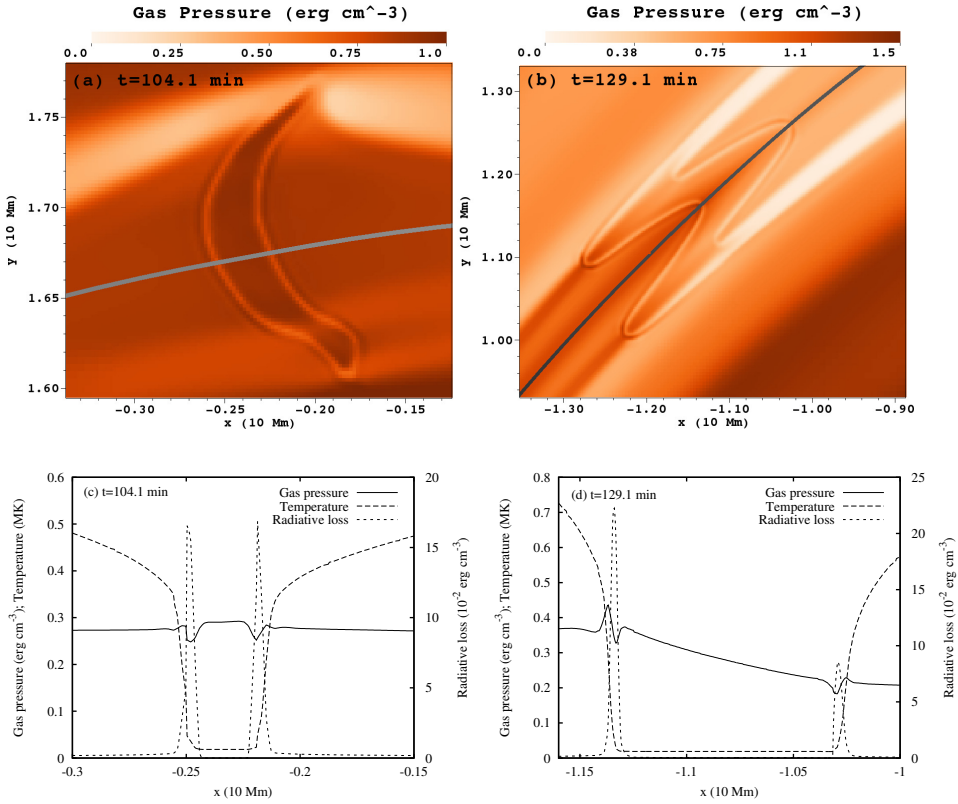

Figure 3.9: At $t \approx 104.1$ (left) and 129.1 minutes (right), we show in the top row panels (a) and (b) the gas pressure maps. Panels (c) and (d) plot gas pressure, temperature, and radiation loss along the selected field line crossing the blob center.

blob in our simulation.

The gas pressure difference between inside and outside the condensation is found to persist throughout the lifetime of the blobs and plays a role in the movement of the blobs. Especially when the blobs fall along the field lines toward footpoints, the gas pressure and temperature ahead of the descending blob increase as shown in panel b of Fig. 3.9, due to the blob compressing the plasma ahead of it in the loop and the strong evaporation at the loop footpoints. We also identify a field line crossing the center of the blob shown in panel b of Fig. 3.9 and plot gas pressure, temperature and radiation loss along this field line in panel d of Fig. 3.9, which shows also an obvious PCTR. Due to the gravity variation and the strong gas pressure gradient between the two sides of the blob, the lower part of this blob has a higher density distribution,

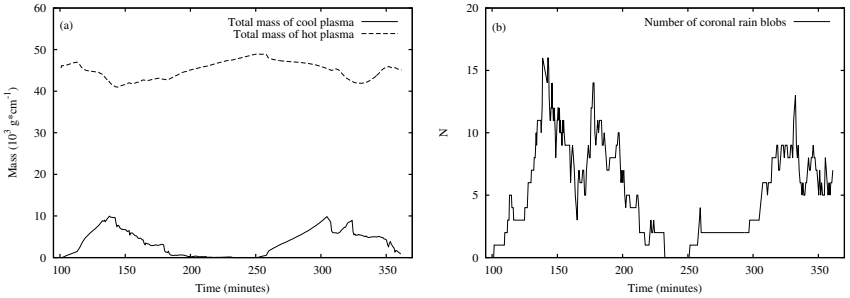

Figure 3.10: (a) Total mass of cool and of hot plasma in the corona versus time. (b) Number of blobs versus time.

which naturally leads to a higher radiative loss. This strong gas pressure gradient slows down the acceleration of the blob in its descent. This was also pointed out in Fang et al. (2013), and in section 3.3.2 where we stated that sometimes, it can even lift lighter blobs to cross the loop apex.

3.3.4 Coronal Rain Limit Cycle and Condensation Rate

Panel a of Fig. 3.10 shows the temporal evolution of total mass of cool (solid) and hot (dashed) plasma in the corona, and panel b of Fig. 3.10 represents the number of blobs for the entire time interval of our 2.5D simulation. The criteria to identify whether a cell contains cool plasma belonging to coronal rain are that (i) the number density is higher than 7×10^9 cm^{-3}, (ii) the temperature is lower than 2×10^4 K, and (iii) the location is above the chromosphere-corona-transition-region. We dynamically locate the height of the transition region at each x-position as $y^{tr}(x,t)$ by searching the vertical position of the (first) maximum gradient value of temperature from the bottom boundary. Each blob is defined as a collection of neighbouring cells which hold cool plasma. However, if the number of grid cells in one blob is smaller than 10 at our highest resolution, we remove this blob from the blob list to avoid counting spurious transient features that do not collect into a clearly resolvable blob, and also to mimic the observational resolution. As stated before, we adopt a 4 times higher resolution than in Fang et al. (2013), and in section 3.3.1 & 3.3.2, but also extend the simulation to a two times longer time of around 370 minutes (previously 190 mins). By running our 2.5D simulation for these much longer times, we find that the whole coronal rain process shows limit cycles, which has been discussed in earlier 1D simulations (Müller et al., 2003), as well as in observational work (Antolin and Rouppe van der Voort, 2012). This is the first time that we can report limit cycles of coronal rain in a multidimensional simulation, which confirms that constant heating conditions which provide enough energy, can form secondary (or even more) coronal rain cycles in a single arcade. From panel a and b of Fig. 3.10, we find the time interval between the

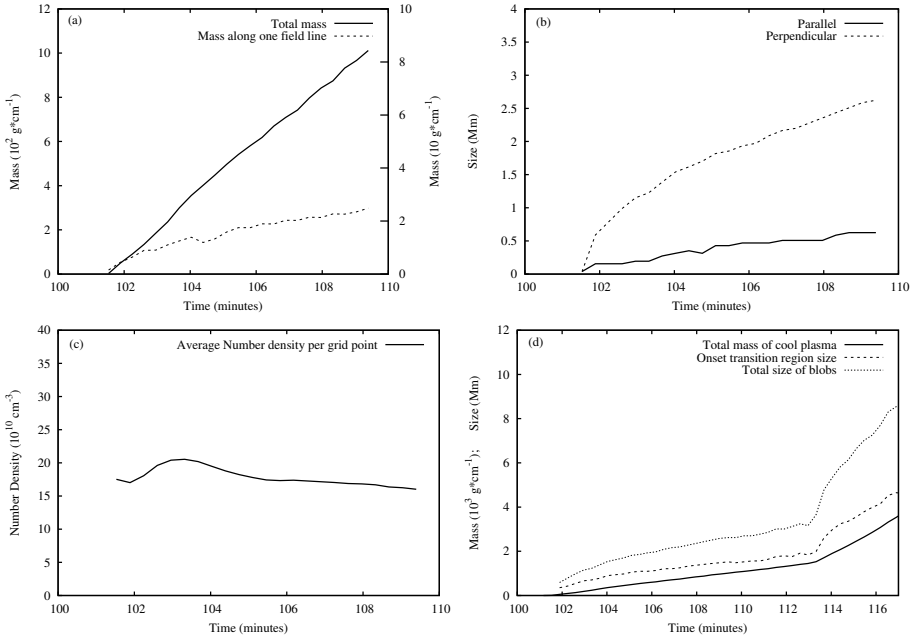

Figure 3.11: (a) Mass in the first condensation versus time. The dashed line shows a measurement performed along one field line only. (b) Lengths versus time of the first condensation (solid: length parallel to the magnetic field lines; dashed: length perpendicular to the magnetic field lines). (c) Average density evolution of the first condensation. (d)Total mass of cool plasma in the corona (solid), onset transition region size (long dashed) and total size of blobs (short dashed) versus time within the range from 100 minutes to 117 minutes.

first and secondary cycle to be around 175 minutes, when measured between successive maxima in cool mass matter.

Panel a of Fig. 3.10 shows the temporal evolution of total mass of hot coronal plasma which is the mass in the corona, excluding the cool plasma identified by the above criteria. We find that at $t \approx 140$ minutes, the total mass of cool plasma reaches its peak in the first cycle in panel a of Fig. 3.10, while at $t \approx 143$ minutes the catastrophic cooling process has cooled down most of the hot plasma in the corona shown in panel a of Fig. 3.10. From about $t \approx 133$ minutes, blobs begin to fall into the transition region, then the evaporation of plasma in the chromosphere driven by the extra heating H_1 fills the evacuated loops left by blobs which already sank into the chromosphere. From this moment, until the onset of the secondary cycle of our coronal rain shower at $t \approx 250$ minutes, it takes about 120 minutes, which is of similar duration as the time for the first cycle to reach its onset (about 100 minutes). So although we infer from

the total mass evolution of cool plasma in panel a that there is only about 50 minutes between the ending of the first and the beginning of the second cycle, actually the continued heating at the chromosphere spontaneously begins to fill the empty corona already 70 minutes before. We also see that the total mass of hot plasma before the onset of the secondary cycle is higher than in the first cycle (panel a), which leads to a longer lasting secondary cycle with more mass in condensations. Panel a of Fig. 3.10 indicates that at $t \approx 130$ minutes (before the first blob falls into the chromosphere), there is at least 9×10^3 g cm^{-1} cool plasma in the corona, which originally was hot plasma. Meanwhile panel a of Fig. 3.10 also suggests that compared with the corona before the onset of catastrophic cooling at $t \approx 100$ minutes, the decrement in the same time of total mass of hot plasma at $t \approx 140$ minutes is only 5×10^3 g cm^{-1}. The difference between the increase in cool plasma and the decrease in hot, indicates that during these 30 minutes since onset at $t \approx 100$ minutes, the evaporation in the chromosphere evaporates 4×10^3 g cm^{-1} into the corona, i.e. at an evaporation rate of 2.2 g cm^{-1} s^{-1}. We can similarly estimate an evaporation rate of 2.3 g cm^{-1} s^{-1} between the onset of the secondary cycle and the moment its first blob falls into the transition region.

Till the onset of the first cycle at $t \approx 100$ minutes, the increment of total hot plasma from turning on the extra heating H_1 is about 13.2×10^3 g cm^{-1} in total, further confirming this evaporation rate of 2.2 g cm^{-1} s^{-1}. Based on these estimates, we infer that anywhere in both simulated cycles, the constant extra heating H_1 leads to a nearly constant evaporation rate. We can thus extrapolate to even more cycles expected further on, and interpret these limit cycles as a chronological sequence of mass recycling between chromosphere and corona: heating in the chromosphere brings plasma to the corona by evaporation, where it ultimately triggers catastrophic cooling, the cooling process manages itself into a coronal rain where plasma drains back to the chromosphere, and persistent heating causes the chromospheric material to evaporate again towards the corona.

Although the duration and peak value of the total mass in both computed cycles are similar, their initial condensation rates (in contrast to the previously discussed evaporation rate) computed from the temporal variation of their total mass curve work out to be 6.7 and 4.5 g cm^{-1} s^{-1}, respectively and thus are different. It is known from linear thermal instability theory (Field, 1965) and 1D simulation results in Xia et al. (2011), that this initial condensation rate in catastrophic cooling depends on parameters controlling the energy input from heating. One notices that the condensation rate (the local derivative of the solid curve in panel a of Fig. 3.10) varies dramatically even within one cycle, despite a constant heating energy input in our multidimensional simulation. We now will interpret the reason for the changes seen in the condensation rate, by surveying especially the process of growth for the first condensation which forms under a relatively simple and almost symmetric condition.

The solid line in panel a of Fig. 3.11 shows the temporal evolution of the mass accumulation for this first condensation (the one from Fig. 3.6) from $t \approx 100$ to 110 minutes. Its near linear behavior quantifies that the condensation rate remains almost constant in this time interval at a value of about 2.3 g cm^{-1} s^{-1}. We deliberately

do not discuss what happens to the first condensation after $t \approx 110$ minutes, since afterwards it breaks into two smaller blobs. In the same figure panel a, the dashed line displays the growth of the total mass of cool plasma as seen on a single field line through the center of the first condensation, i.e. in a 1D fashion. To show this, we identify the group of grid points which are passed by the field line. The total mass of cool plasma determined on the single field line keeps growing in time, but its growth rate is much smaller than that for the whole 2D condensation. Panel b of Fig. 3.11 quantifies the temporal evolution of typical lengths for the first condensation, where we quantify both the length parallel to the magnetic field lines and the length perpendicular to the magnetic field lines. This indicates that blob growth in the perpendicular direction is much faster than in the parallel one, which can be seen visually as well in all columns in Fig. 3.6 and Fig. 3.7. As discussed in Fang et al. (2013), the low pressure region surrounding the first condensation onset leads to magnetic restoring forces on adjacent loops. These in turn influence in which location the catastrophic cooling will take place on the adjacent loops, which are all close to the thermal instability onset. The different growth rates found for blob sizes in these two directions then relate to the fairly fast 'growth' along the perpendicular direction due to sympathetic runaway cooling onset, versus the slower growth seen in the parallel one, which is the only one found in 1D setups. The average density of each cell of the condensation is quantified in panel c of Fig. 3.11, and this density stays basically the same in the forming process, meaning that the total mass of the condensation is just proportional to the increasing number of neighbouring grid cells that contain cool plasma. While the number of cells in the condensation increases in both directions, the larger condensation rate of the whole blob in panel a of Fig. 3.11 again directly reflects the faster growth in size in the perpendicular direction. We conclude that the growth of total mass of individual blobs in our simulation is mainly determined by the onset of catastrophic cooling in neighbouring loops rather than the growth along the loops in which catastrophic cooling gets triggered. We can indeed verify this 2D growth aspect by further showing a correlation between the total mass of cool plasma and two other measures, which holds up even for a longer time than the first 10 minutes, i.e. when several blobs have started to form. This is shown in panel d in Fig. 3.11 where we plot the temporal evolution of total mass of cool plasma, the size of the onset transition region, and the total blob region width. The total blob region width indicates the total width of all magnetic loops where catastrophic cooling takes place on. The size of onset transition region means the corresponding width as found at the transition region height, of all the loops undergoing catastrophic cooling. Because the magnetic arcade configuration adopted, these size measures for the affected loops give higher values for higher locations, i.e. the total blob region width always exceeds the (field aligned remapped) onset transition region size. The latter size of the onset transition region shows a nice correlation with the total mass of cool plasma evolution.

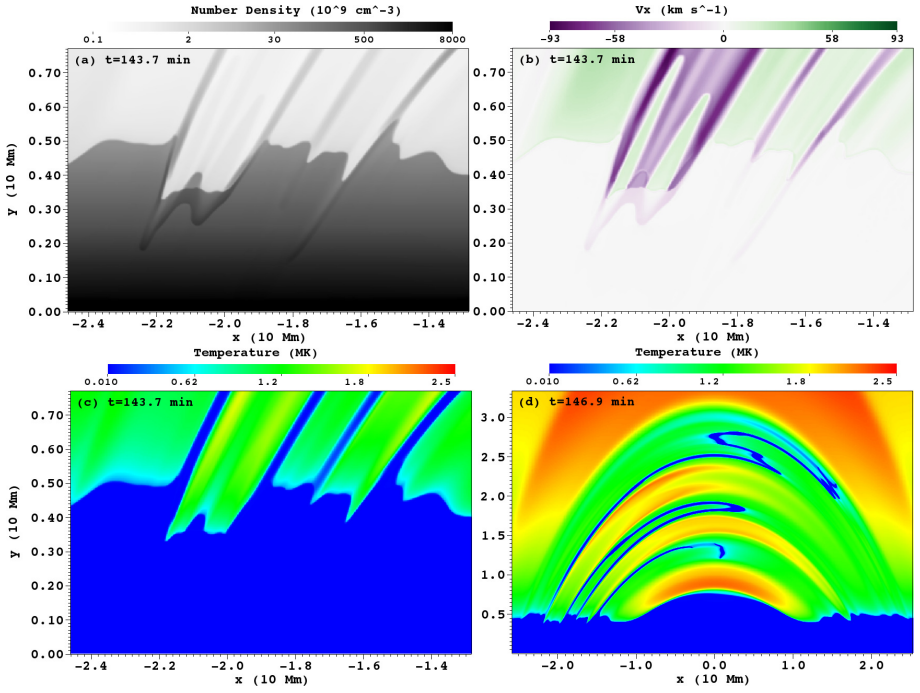

Figure 3.12: (a) The number density map at $t \approx 143.7$ min; (b) The horizontal velocity component map; (c) The temperature map. These three panels show the same local area with chromosphere and transition region variations, while a larger area view is shown in panel (d), giving a later temperature map at $t \approx 146.9$ min.

3.3.5 The Fate of Blobs Hitting the Transition Region

In the simulation, we observe plenty of blobs hitting the transition region and disappearing into the lower chromosphere, as also known to occur in observations (Antolin et al., 2010; Antolin and Rouppe van der Voort, 2012). Tripathi et al. (2009) observed high-speed downflows and concurrent upflows in coronal loops close to the footpoints and argue in favor of upflows in coronal loops at higher temperatures. Antolin et al. (2010) confirmed that the high-speed downflows represent the cool plasma, which is corresponding to the falling blobs in our simulation (see once more also the movie of Fang et al. 2013). Meanwhile, our 2.5D simulation also shows the possibility of triggering concurrent upflows as observed by Tripathi et al. (2009) and Kleint et al. (2014). Panel a in Fig. 3.12 shows the number density map at $t \approx 143.7$ at a moment when falling blobs sink into the transition region and compress the plasma on its way (at about $x \approx -2.1$ Mm). Panel b in Fig. 3.12 shows the vertical velocity map at the same location and instant, which clearly displays the concurrent

upflows rising at the tails of the declining blobs in the same field line bundles. Hence, this answers the question in Kleint et al. (2014) whether the upflows can flow along the same field lines as the downflows. These upflows in our simulation are actually rebound shocks from the impact of the blobs on the transition region (TR). They arise immediately when the blobs impact on the TR, and spread from one footpoint to another footpoint in around 5 minutes with a velocity of around 50 km s^{-1} . From Panel a we can see the enhanced density left after passage of these rebound shocks. However, panel c in Fig. 3.12 which quantifies temperature indicates that the temperature in the loop already increases before the rebound shocks have reached far into the loop, since the parametrized background heating H_0 heats the low density loops left by falling blobs very efficiently. Panel d shows also the temperature, but now on a larger domain and at a later time. It shows that afterwards the rebound shocks heat the low density loops to an even higher temperature of 2.0 MK. After the rebound shocks reach the other footpoint, the loops are at high temperature of about 2 MK but with a low number density of 1×10^8 cm^{-3}. We distinguish this from further upflows coming from evaporation due to the extra strong heating H_1 located in the chromosphere. This enhances the density to 1×10^9 cm^{-3} again and the temperature to 2.3 MK. However, these upflows from evaporation rise with a much slower velocity of around 15 km s^{-1}.

To quantify even further the detailed fate of a blob when it hits and descends into the TR, Fig. 3.13 shows the temporal evolution of the mass, density, velocity, kinetic energy, momentum, and temperature of the first coronal rain blob to hit the transition region from the corona and to sink down into the chromosphere. The vertical dashed line in each panel of Fig. 3.13 points at $t \approx 132$ minutes when this blob hits the transition region. Because the density and temperature of plasma in the transition region is comparable with those of the blobs, we can not use only the density and temperature as a criterium to distinguish blobs when they are near or partially below the transition region anymore. In order to identify plasma belonging to the blob as it hits and descends in the transition region after $t \approx 132$ minutes, we change our criteria to require the local velocity to be larger than 3 km s^{-1} and the location are below the transition region line $y^{tr}(x,t)$ after $t \approx 132$ minutes. Since the velocity of plasma in the transition region is almost zero, this velocity-based criterion captures the location of sinking blobs. In panel a of Fig. 3.13, we find that the mass identified as blob material by the above criteria begins to increase at t$\approx$ 132.7 minutes. This is because the mass detected not only includes the blob itself, but also counts mass compressed and accelerated by the blob impact. At $t \approx 136$ minutes, the total mass affected reaches its peak at six times the original blob mass. After $t \approx 136$ minutes, due to the combined influence of reflection-transmission processes at the transition region, and the higher gas pressure from the impact, the velocities in much of the blob impacted area decrease to values smaller than the criterion 3 km s^{-1}. This is then seen as a mass decrease in our panel a. In panel b of Fig. 3.13, the density versus time profile keeps rising while the blob hits the transition region. As we know, this blob impact compresses the transition region plasma swept up by the blob and transfers momentum from the sinking blob to the impacted plasma, and therefore in panel c of Fig. 3.13 we find that the average velocity of the region identified keeps decreasing

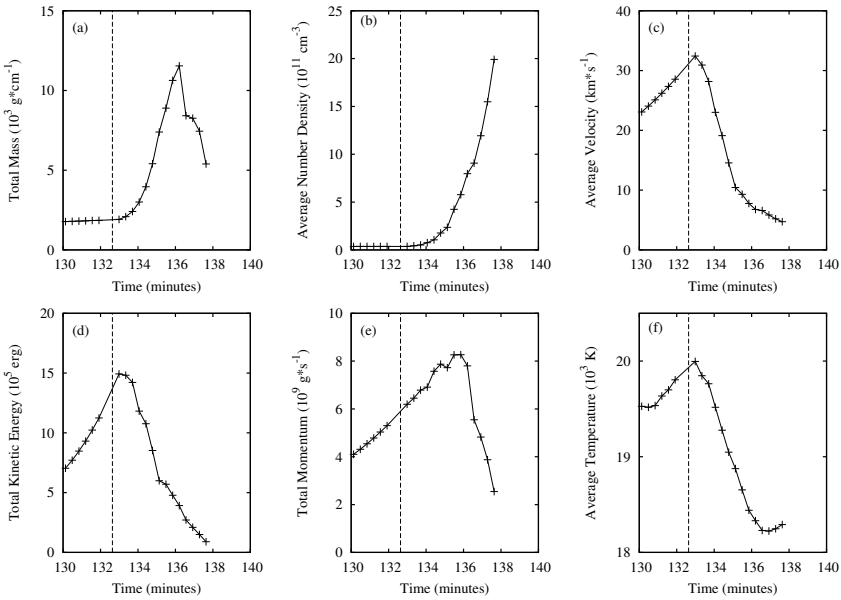

Figure 3.13: We show the total mass, average number density, average velocity, total kinetic energy, total momentum and temperature evolution of the blob which first impacts and sinks into transition region, during this time period. Vertical dashed line indicates the time when this blob hits the transition region.

during the whole process, as well as the kinetic energy shown in panel d. Panel e of Fig. 3.13 shows the total momentum of the mass identified. Due to the gravitational acceleration, the blob momentum keeps increasing until it reaches its maximum value at $t \approx 136$ minutes, then it reduces quickly. This is a combination of the mass evolution in panel a and the velocity info from panel c. The momentum and velocity decreasing after the impact relate to momentum transfer to the surrounding transition region and upper chromosphere plasma, until the regions selected by the velocity-based criteria vanishes: the local conditions settle to static chromosphere conditions. Panel f of Fig. 3.13 shows the average temperature evolution during the blob impact. The temperature increases before hitting the TR due to the compressional heating when the blob descends through the higher gas pressure region just above the transition region. After the impact, since also more cooler material gets identified as impacted matter, one settles back to upper chromospheric temperature values.

The impact speed of blobs in Fig. 3.13 is around 30 km s^{-1}, and the highest impact speed of all blobs in our simulation is around 60 km s^{-1} and number densities range from 4 to $6{\times}10^{10}$ cm^{-3}. Our maximum impact speed is much lower than the falling speeds reported in Kleint et al. (2014) which went up to 200 km s^{-1}. They report that these coronal rain events with high impact speeds are correlated with local

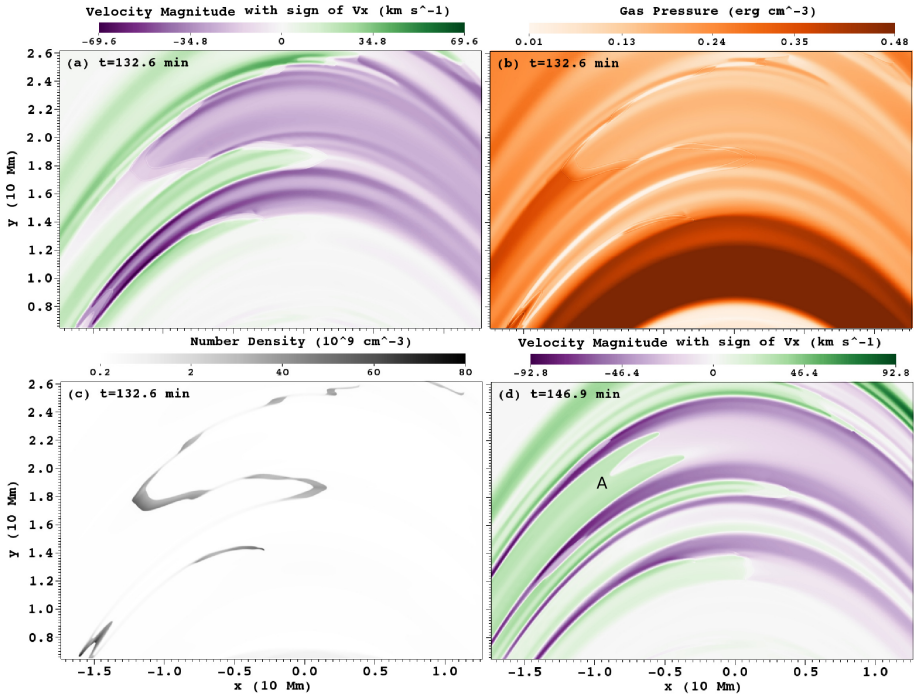

Figure 3.14: (a) shows the velocity magnitude map signed with horizontal velocity component at $t \approx 132.6$ minutes. Panel (b) shows the gas pressure map and panel (c) shows the number density map at the same time. In panel (d), the signed velocity magnitude map is shown later at $t \approx 146.9$ min, where the label A points to the upflows resulting from the rebound event shown in detail in Fig. 3.12.

brightenings which probably indicate an increase of density and temperature in the transition region. Panel b of Fig. 3.13 and panel a of Fig. 3.12 confirm the expected increase of the number density of impacts in our simulation.

3.3.6 Counter-streaming Flows

We also find another interesting phenomenon in our numerical simulation, namely the self-consistent establishment of counter-streaming flows. Such anti-parallel flows are very commonly found in solar observations, especially also in prominences (Alexander et al., 2013). Panels a, b and c in Fig. 3.14 respectively show the signed velocity magnitude map (with the sign taken from the horizontal velocity component), the gas pressure map and the number density map at $t \approx 132.6$ minutes. Panel d shows

the signed velocity magnitude map as in panel a, but at a later time, namely at $t \approx 146.9$ minutes. These four panels in Fig. 3.14 display many cases of counter-streaming flows established on neighbouring field line bundles in our simulation and allow to explain the origins of counter-streaming flows. After thermal instability inducing a runaway catastrophic cooling and initial growth in an almost static state, the condensations lose their delicate force balance and begin to slide towards one footpoint along magnetic field lines. Whether a particular condensation segment slides to the left or right is influenced by its initial location and local total force balance (gravity, gas pressure gradient and magnetic field force). Once in motion, they are accelerated by the field-projected gravitational force, meanwhile catastrophic cooling keeps taking place around the condensations. As discussed in Section 3.3.3, the initial catastrophic cooling process depletes the local plasma and sucks in fast inflows, then the spontaneous rebound shocks heat the plasma and increase the gas pressure. Afterwards, no stronger inflows are driven again due to the increased gas pressure. However, there can be several blob pairs lying in the same or neighbouring field line bundles, as shown in panel c of Fig. 3.14. Fig. 3.15 shows gas pressure maps with magnetic field lines at $t \approx 109.4$ and 113.0 minutes. The black contour relates to the temperature distribution and is an isocontour at 0.1 MK. Both the gas pressure and temperature in panel a in Fig. 3.15 indicate the clear PCTR around the blob as previously discussed in Fig. 3.9. After 3 minutes, the panel b of Fig. 3.15 shows two white (low) pressure sections after the blob breaks into three segments. These low pressure sections slant through the field lines and they are the elongated PCTR cross sections from the original parts of the whole blob in panel a of Fig. 3.15. Because the strong radiation in the PCTR, the temperatures inside these elongated regions stay low during their deformation. As a result, we could consider these cross sections to undergo an isothermal expansion. Because the condensed mass in these narrow regions grows much slower than their areal growth due to elongation, the densities inside these elongated cross sections decrease faster as well as the gas pressure. This leads to blob sequences with low pressure sections in between them. This is also seen in panel b of Fig. 3.14 where a sequence of blobs show up with white (low) pressure sections in between them. The depleted areas trigger siphon inflows to refill these regions. Then this pair of siphoned fast inflows establish the counter-streaming flows between the pair of neighbouring blobs. Panels a and b in Fig. 3.14 also show that falling condensations with larger velocities induce larger density depletions and lower gas pressure areas on their way down, which leads to faster inflows than those found for more static condensations.

Panel d in Fig. 3.14 indicates another different origin of counter-streaming flows at $t \approx 146.9$ minutes. As we discuss in Section 3.3.5, we observe that after blobs decline into the transition region, concurrent upflows rise up towards the loop apex. Upflows labeled as A in panel d in Fig. 3.14 are the concurrent upflows shown in panel b of Fig. 3.12, but about 3 minutes later (concurrent with the later temperature panel d of Fig. 3.12). Upflows arising from blob impacts also have the chance to establish a counter-streaming flow if there is an opposite flow pattern in the neighbouring loops. The difference between these two different origins for counter-streaming flows is that the one based on depleted sections between a pair of blobs lying on neighbouring field

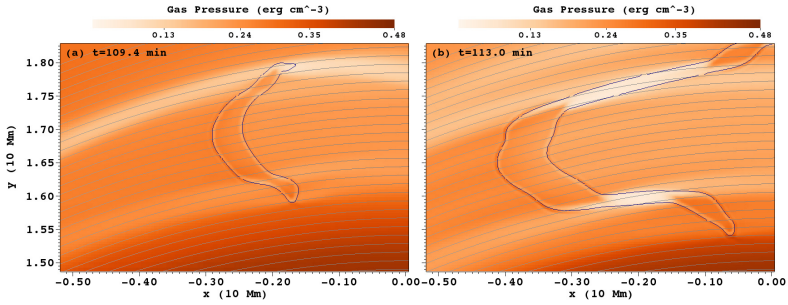

Figure 3.15: Panel a and b show the gas pressure maps with magnetic field lines at $t \approx 109.4$ and 113.0 minutes. The black contour relates to the temperature distribution with level at 0.1 MK.

line bundles can last through the whole falling process of blobs, or on time scales of about 10 minutes, while the other ones will vanish after the upflows refill the loops, typically in a shorter time scale of about 5 minutes.

The sheared flows that are established by the detailed blob dynamics could also in return influence the further evolution of the condensations. An example is shown in panel a of Fig. 3.16, where we show a signed velocity map, with overlaid contours of the density distribution of condensations at levels of 7, 25 and 50 $\times 10^9$ cm^{-3} at $t \approx 123.7$ minutes. Concentrating on the density feature labeled with A, after its initial formation, sheared flows already begin to take shape. About 10 minutes later, this segment A is seen as segment A1 and A2 in panel b of Fig. 3.16 and the condensation has broken into two distinct segments with increasing separation between them. Segment A2 is also going to break into two segments a little later. At the $t \approx 123.7$ minutes in panel a of Fig. 3.16, this segment A feature is more like one whole elongated condensation. However, by $t \approx 132.6$ in panel b in Fig. 3.16, several condensations behave totally separate to each other. Another example is the one of segment B in panel a and panel b. This breaks up into segment B1 and segment B2 in panel c at $t \approx 136.2$ minutes. Then segment B1 further breaks into segment B1 and B3 in panel d at $t \approx 139.8$ minutes. This gradual change from one elongated dense blob or strand breaking into several segments, surrounded by fast sheared flows, hints at the influence of Kelvin-Helmholtz instabilities (KHI). However, there is no clear vorticity pattern emerging in our simulation that would clearly identify KHI development, which may not have enough time to develop. We speculate that other KHI related substructure may well arise under different parameter settings (field strength, heating scale height), but already establish that sheared flows contribute to the breaking up of elongated condensations into smaller fragments.

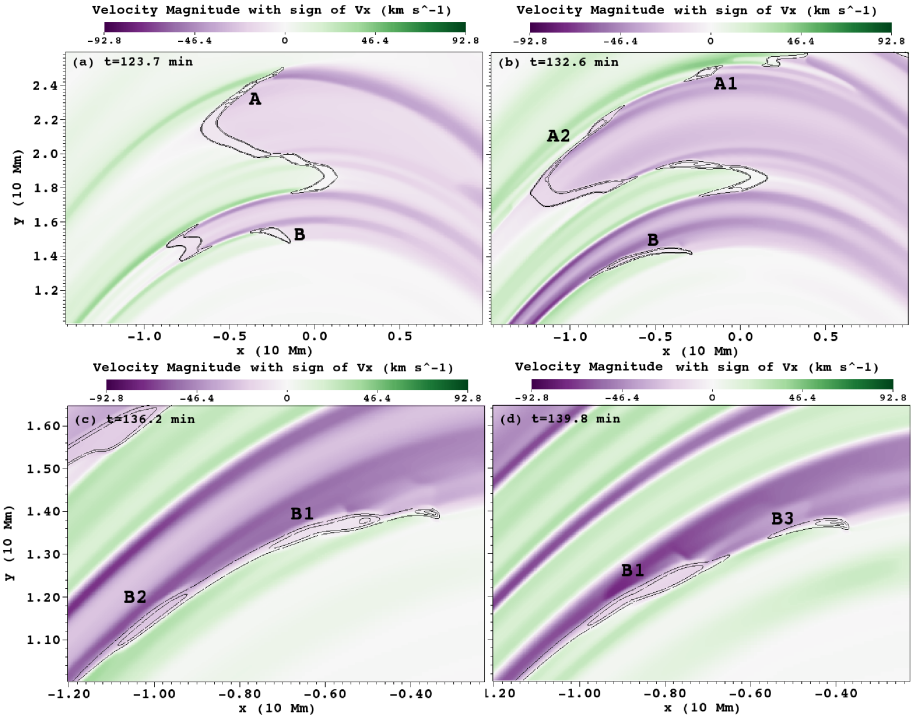

Figure 3.16: Color maps show the velocity magnitude map with the sign of the horizontal velocity component at $t \approx 123.7$ (a), 132.6 (b), 136.2 (c) and 139.8 (d) minutes. The black contours relate to the number density distribution with levels at 7, 25 and 50 $\times 10^9$ cm^{-3}. This clearly shows how shear flow effects induce blob fragmentation and evolution.

3.3.7 Blobs Trailed by Repeated Patterns

In our simulation, we find that some blobs emit repeated patterns while they fall and break. Panel b, c and d in Fig. 3.16 represent a clear segment labeled by B where blobs are trailed by patterns as seen in the velocity component maps. These patterns propagate along the field lines that host the falling blobs. In order to study these patterns, we identify one magnetic field line through the center of the blob as seen in segment B in Fig. 3.16 and quantify physical properties along this field line.

Panel a in Fig. 3.17 shows distributions of plasma velocity magnitude (solid line), sound speed (dashed line), and number density (dotted line) along the central field line at $t \approx 132.6$ minutes, while panel b shows distributions of plasma β (solid line) and Mach number (dashed line). The horizontal axis of Fig. 3.17 marks the length calculated from the left footpoint along the field line. The solid line (plasma velocity)

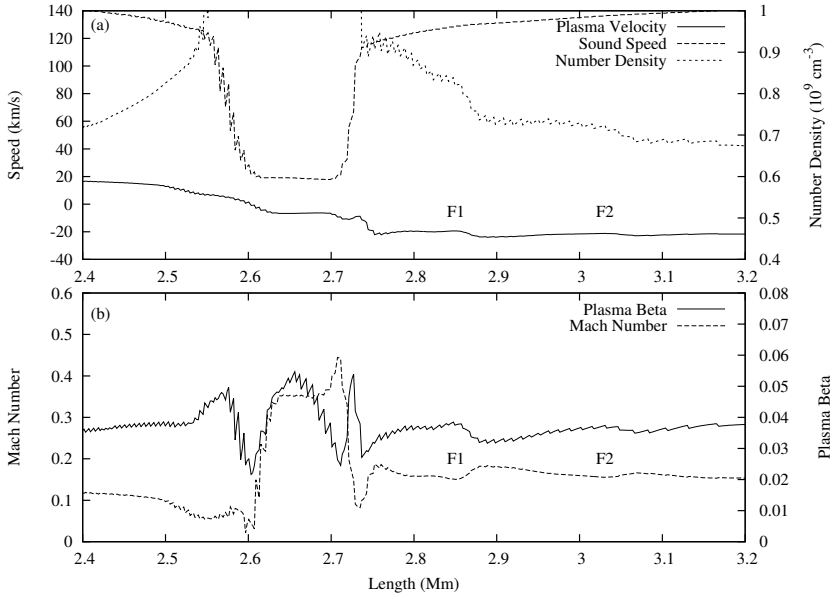

Figure 3.17: At $t \approx 132.6$ minutes, top panel shows distributions of plasma velocity (solid line), sound speed (dashed line), and number density (dotted line) along the field line, while bottom panels show distributions of plasma beta (solid line) and Mach number (dashed line). This is for blob B as shown in Fig. 3.16, along its central field line.

and the dotted line (number density) in panel a both present two patterns shown as F1 and F2 to the right of the blob. We can also find the corresponding pattern structure in the Mach number (dashed line) in panel b in Fig. 3.17 where the distinct variation is clearly seen at position 2.85 and 3.02 Mm, roughly. Since the signed velocities (sign v_x) of the plasma in panel a are both negative inside and at the right side of the blob, the whole structure moves to the left, meanwhile these patterns propagate to the right. The panels in Fig. 3.18 show distributions of Mach number along this field line by chronological order with a 1.7 minute interval. From these panels in Fig. 3.18, we can infer that the blob keeps emitting patterns behind it while it slides towards the left. The panels in Fig. 3.17 show that local variations in number density and local extrema in Mach number match.

Using that correspondence with local extremum values in Mach number, we can make an x-t plot identifying pattern dynamics. Fig. 3.19 shows the location of the minimum value of patterns in Mach number versus time. This diagram suggests the speed of the patterns to have a constant value, around 39 km/s from the slope in this x-t diagram, giving a relative speed between blobs and patterns of about 60-80 km/s. This constant relative speed suggests that these pattern trains are generated by the sliding blob. We

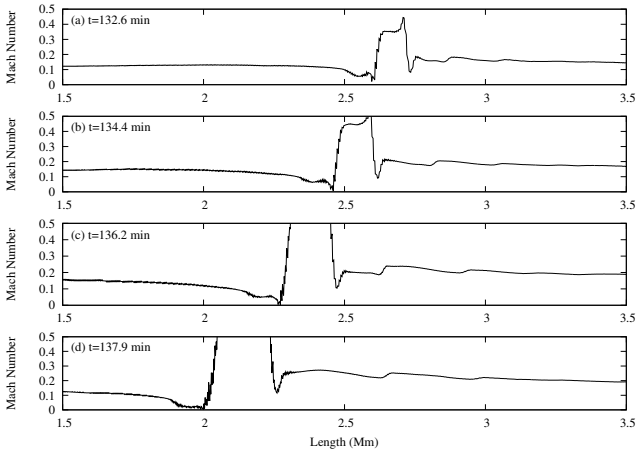

Figure 3.18: Panels show distributions of Mach number along the field line also analysed in Fig. 3.17 by chronological order with a roughly 1.7-1.8 minute interval.

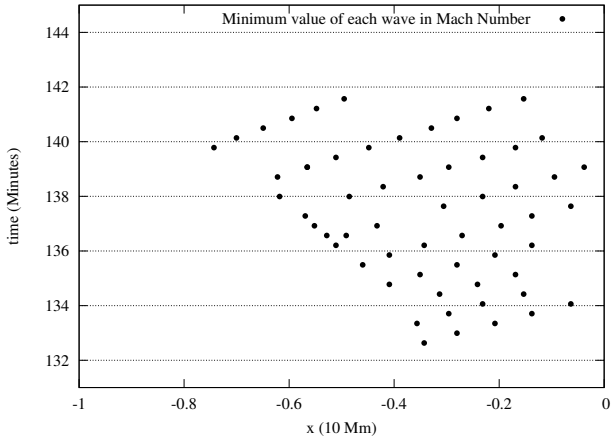

Figure 3.19: We show the x-t plot (x axis versus time) map for minimum Mach number locations of wave trains.

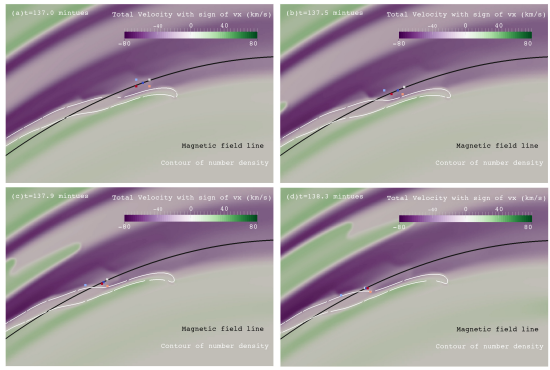

Figure 3.20: Color maps show the velocity magnitude map with the sign of the horizontal velocity component at $t \approx 137.0$ (a), 137.5 (b), 137.9 (c) and 138.3 (d) minutes. Five square symbols with different colors represent the evolution of five advected test particles in the simulation. The white contours relate to the number density distribution with levels at 7×10^9 cm^{-3}. The black line shows one selected magnetic field line through the blob.

can also obtain the time intervals between patterns, which increases from 40s to 110s during the falling of the blob.

Since the local sound speed in panel a of Fig. 3.17 is around 145 km/s which is about double the relative speed (60-80 km/s) between the patterns and the local plasma, these patterns are not pure sound waves or ideal slow magnetosonic waves. In order to verify whether these patters are instead mass flows, we put five test particles in one pattern front at $t \approx 137$ minutes as shown in panel a of Figure 3.20. If these patterns are mass flows, we expect to see that these test particles move with the patterns for a while, to then probably decelerate and change to the direction of the local plasma. However, from the panels in Figure 3.20, we find that the advected particles pass through the patterns. They show how plasma travels along the field line and approaches the blob. Therefore we infer these patterns are not mass flows either.

Figure 3.21 shows the temporal evolution of total velocity maps obtained by temporarily turning off the thermal conduction (first row) or radiative loss (second row) between $t \approx$ 137 and 138.4 minutes. The black contours relate to the number density distribution with levels at 7, 25 and 50 $\times 10^9$cm^{-3}, which represent the structure of the blob in each panel in Figure 3.21. Panel b and c in the first row indicate that except the already existing patterns, the blob stops to emit more patterns without thermal conduction, while we still identify the outline of the blob based on the total velocity maps in the first row of Figure 3.21. However, panel e and f in the second row of Figure 3.21 show that without the radiative loss, not only the blob stops to emit more patterns, but also the fast hot plasma at the right side of the blob decelerates and we are unable to recognise the shape of the blob from total velocity maps anymore. In section §3.4 we

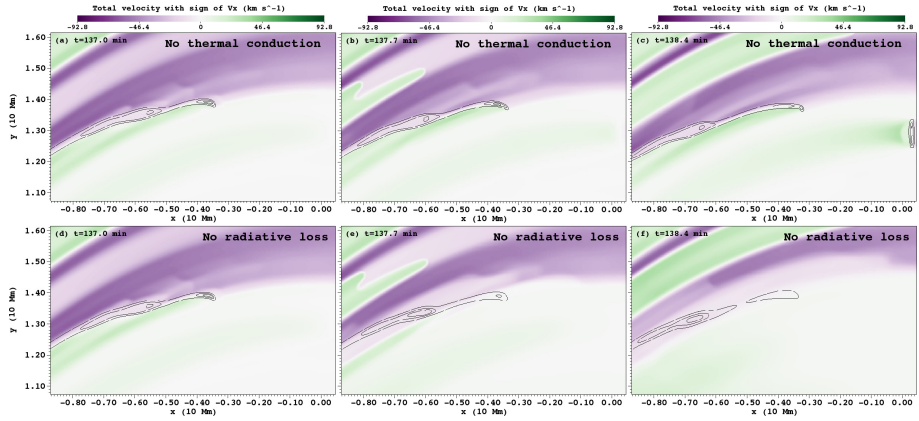

Figure 3.21: Color maps show the velocity magnitude map with the sign of the horizontal velocity component at $t \approx 137.0$ (a,d), 137.7 (b,e), and 138.4 (c,f) minutes. The first row represents the simulation without thermal conduction, while the second row shows the simulation without radiative loss. The black contours relate to the number density distribution with levels at 7, 25 and 50 $\times 10^9$ cm^{-3}.

interpreted the elongated PCTR between neighbouring blobs to be the reason for the high speed hot flow following the blob all the way. Here we deduce that the reason why the high speed hot flow does not decelerate in the simulations with radiative loss is that the PCTR around the blob efficiently cools down and decelerates the head of the fast hot flow by strong radiative losses as shown in panel c and d of Figure 3.9. This could avoid the fast hot flow to impact the blob and cause deceleration of this fast flow. We infer that the elongated PCTR between neighbouring blobs not only triggers the fast siphon flows by low pressure inside PCTR, but its presence also is mediated by strong radiative losses impacting the siphon flows.

Since no more new patterns appear in panel b and panel c in the first row of Figure 3.21, we can imply that the thermal conduction in our simulation is a crucial ingredient for triggering repeated patterns. Considering the similar shapes between patterns and the blob outline (as shown in Figure 3.16), we infer that the huge temperature gradient at both sides of the PCTR (as shown in Figure 3.9) may trigger thermal conduction fronts propagating along the field line. Based on the thermal conduction equation

$$\frac{\partial(2.3 n_{\rm H} k_{\rm B} T/(\gamma-1))}{\partial t} = \kappa_{||} T^{2.5} \nabla^2 T \tag{3.10}$$

we estimate the thermal diffusivity as $\alpha = (\gamma-1)\,\kappa_{||} T^{2.5}/2.3 n_{\rm H} k_{\rm B}$. When we use the width L of the PCTR as a specific length, we can calculate the speed of the thermal conduction front triggered in the PCTR as $v_T = \alpha/L$. For $L = 150$ Km, $n_{\rm H} = 2 \times 10^9$ and $T = 0.5$ MK we obtain v_T around 80 km/s, which agrees with the above relative

pattern speed. Since we find that blobs can emit patterns after a fast flow passes by in a neighbouring loop, the patterns trigger may be pressure disturbances from fast flows in neighbouring loops. The fact that non-adiabatic processes play a key role in triggering wavelike (repeating) patterns calls for further detailed studies of how the full linear MHD wave spectrum can give intricate coupling between thermal and slow magnetosonic modes, and no longer clearly distinguish between entropy, slow, Alfvén and fast modes as in ideal MHD cases. van der Linden and Goossens (1991a) point out that, when non-adiabatic terms are included in the energy equation, but the perpendicular thermal conduction is neglected, a third continuum arises as the 'thermal' continuum.

3.4 3D Coronal Rain Simulation

Although in the previous sections in this chapter we present results from our 2.5D simulations, the ultimate aim of our work is a more realistic full 3D numerical simulation of the coronal rain formation and its dynamics. There is no doubt that comparison between observations and 3D simulation of coronal rain could reveal the physics. In this section we present a preliminary result of our 3D simulation and compare it with the observational results from SDO/AIA.

Panels of Fig 3.22 exhibit a clear evolution process of filamentations and its dynamics in coronal loops by observations from SDO/AIA. Panel (a) shows the full view of the Sun at 08:30 at April 27th, 2013 in 304 Å channel, which represents relative cool plasma with the temperature around 0.5 MK, and panel (b) shows the zoom-in view of the top left margin of the Sun. Half hour later at 09:00 in panel (c), a small filament appears which keeps growing later on in the panel (d). Meanwhile, the filaments start to slide down along the loops in panel (e) to the right side footpoint. Suddenly in the panel (f), the whole big filament splits into many small filaments which slide down along another side leg of the loop in panel (g). After the majority of these filaments fall into the underlying chromosphere as shown in panel (h), there is no filament any more in the same area in the corona. This transient phenomenon demonstrates the fast dynamical evolution of coronal loops in almost 5 hours.

In order to compare our model with the above realistic observation, we proceed from our previous 2.5D numerical setup into a full 3D MHD numerical simulation realm. The governing equations are the same as in the 2.5D simulation as Eq.(3.1-3.4) in Section 3.2.1, as well as the initial linear force-free magnetic field for the initial magnetic configuration (Eq.(3.5)) and initial profile of the temperature and the number density. The difference is that we expand the 2.5D simulation box to a 3D cube with each extension as -30 Mm to 30 Mm for x and y axises, 0 Mm to 40 Mm for z axis. Besides, we also adapt the localized footpoint heating H_1 as

$$H_1 = \begin{cases} c_1 & \text{if} \quad z < z_c \\ c_1 \exp(-(z - z_c)^2/\lambda^2) & \text{if} \quad z \geq z_c \end{cases} \tag{3.11}$$

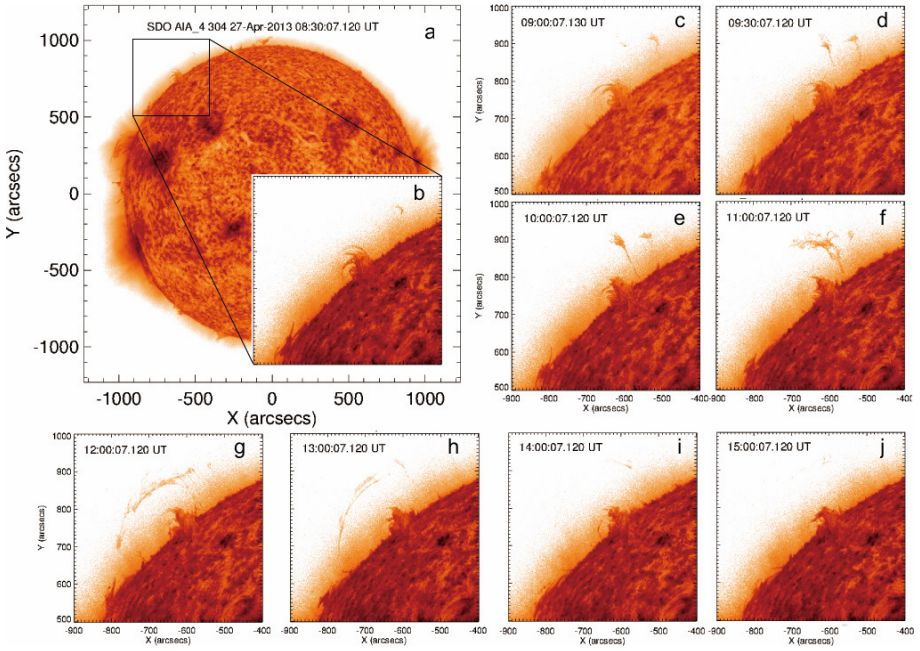

Figure 3.22: Panel (a) shows the 304 Å channel view of the full Sun at 08:30 at April 27th, 2013, and panel (b) shows the zoom-in view of the top-left area where we are interested in panel (a). In the same view as the panel (b), the rest panels (c) to (j) represent a fantastic evolution of filamentation and dynamics from 09:00 to 15:00 at April 27th, 2013.

with the condition as

$$((x < 0 \quad \text{and} \quad y < 0) \quad \text{or} \quad (x > 0 \quad \text{and} \quad y > 0)),$$

$$\sqrt{\{A(x,z) - A_{\text{center}}(x_1)\}^2 + \{A(y,z) - A_{\text{center}}(x_1)\}^2)} \leq A_{\text{radius}}(x_1, x_2),$$

$$A(x,z) = \frac{B_0 L_0}{\pi} \cos\left(\frac{\pi x}{L_0}\right) \exp\left(-\frac{\pi z \sin\theta_0}{L_0}\right),$$

$$A(y,z) = \frac{B_0 L_0}{\pi} \cos\left(\frac{\pi y}{L_0}\right) \exp\left(-\frac{\pi z \sin\theta_0}{L_0}\right),$$

$$A_{\text{center}}(x_1) = \frac{B_0 L_0}{\pi} \cos(\frac{\pi x_1}{L_0}),$$

$$A_{\text{radius}}(x_1, x_2) = A_{\text{center}}(x_1) - \frac{B_0 L_0}{\pi} \cos(\frac{\pi x_2}{L_0}),$$

where $c_1 = 2.5^{-2}$ erg cm^{-3} s^{-1}, $z_c = 3$ Mm, $x_1 = 20$ Mm, $x_2 = 23$ Mm, $L_0 = 60$ Mm and $\lambda = 0.4$ Mm. Fig 3.23 shows the initial setup of our 3D simulation box.

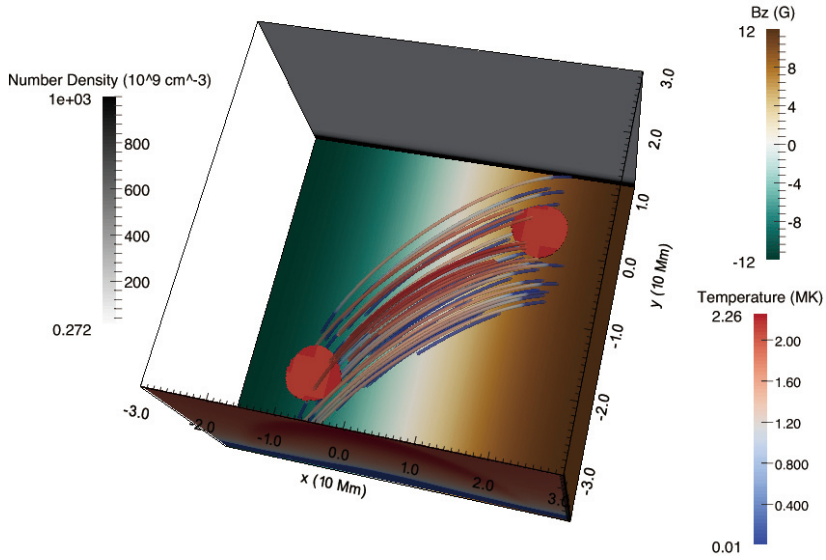

Figure 3.23: 3D demonstration of the initial setup of the simulation cube. The extension is -30 Mm and 30 Mm for x and y axis, 0 Mm to 40 Mm for z axis. The grey slice at y=30 Mm shows the number density profile, while the blue-red slice at y=-30 Mm shows the temperature profile. The bottom green-yellow slice shows the distribution of the vertical magnetic filed (Bz). The tubes indicate the magnetic field lines which are coloured by the local temperature. The two dark pink circles are the localized heating H_1.

The grey slice at y=30 Mm represents the profile of the stratified number density from chromosphere (dark bottom), transition region and corona (light grey). The bottom slice at z=0 Mm indicates the vertical magnetic field distribution at upper chromosphere, in which the white exhibits the neutral line. The blue-red slice at y=-30 Mm shows the profile of the temperature which goes from the cold chromosphere (blue) to the hot corona (red). The tubes form the distribution of magnetic field, and they are coloured by the temperature distribution. This arcade is the same as in the 2.5D simulation except the angle to the neutral line is 45 degree instead of 60 degree in the 2.5D simulation. The two dark pink circles located at two side footpoints of coronal loops present the localized extra heating H_1.

We still use MPI-AMRVAC to run this 3D setup, with an effective resolutions of $384 \times 384 \times 256$, or an equivalent spatial resolution of 156 km in all directions through three AMR levels. Our numerical strategy keeps the same as the 2.5 simulation, with a three-step Runge-Kutta type scheme, a third-order-accurate limited reconstruction (Čada and Torrilhon, 2009), and a suitably mixed prescription between a diffusive total variation diminishing Lax-Friedrichs and contact-resolving Harten-Lax-van Leer

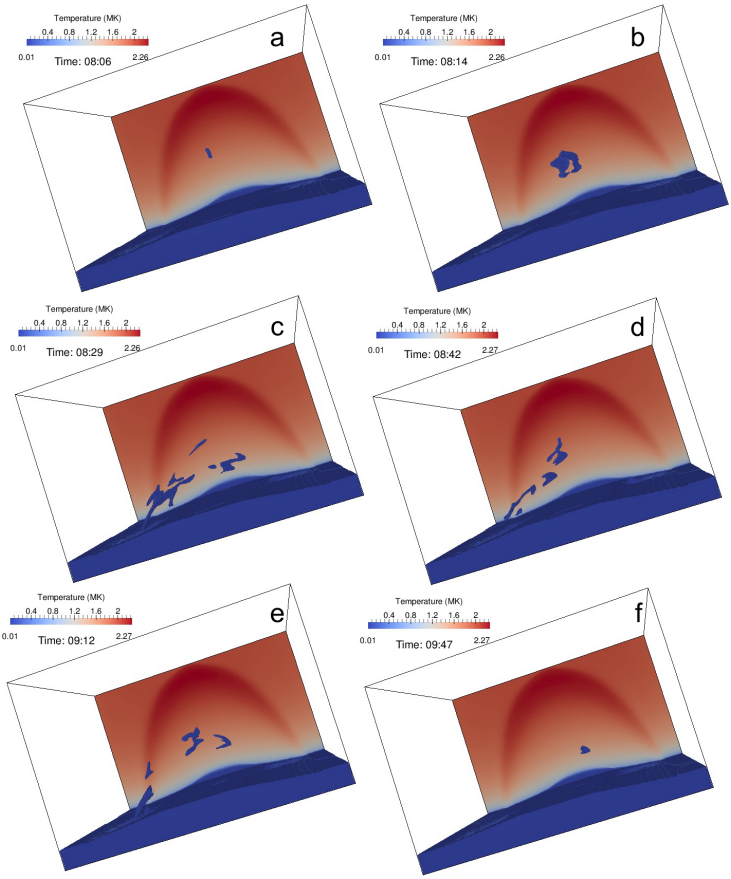

Figure 3.24: Panels show the cells in the box with a threshold of the number density larger than 15×10^9 cm^{-3} and these cells are coloured by the local temperature at different time slots. These panels represent the whole process of the condensation and the evolution of its filamentation and dynamics.

(HLL) scheme (Meliani et al., 2008).

After the system reached its equilibrium state by running 2 hours, we turn on the extra heating H_1 to mimic the footpoint heating to evaporate the cool chromosphere plasma into the coronal loops and reset the system time back to zero. Just like the 2.5D simulation, the number density in the loops increases while the temperature slowly decreases, till meeting the criteria of the onset of the thermal instability. Panels in Fig 3.24 show cells with the threshold of the number density larger than 15×10^9 cm^{-3} and these cells are coloured by the local temperature. After heating around 8

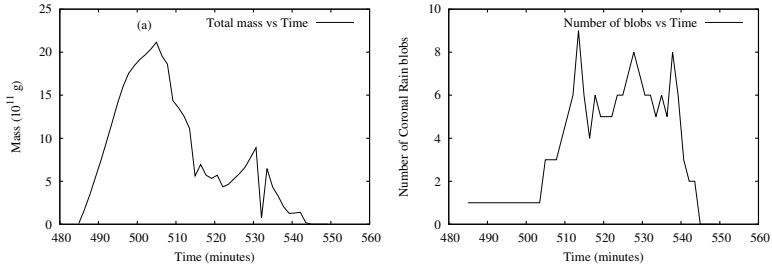

Figure 3.25: (a) Total mass of cool and of hot plasma in the corona versus time. (b) Number of blobs versus time.

hours, panel (a) in Fig 3.24 displays the first condensation formation near the apex of the heated loops, just like the small and faint blob observed in panel (c) of Fig 3.22. Very shortly after around 8 minutes later, the condensation grows rapidly and begins to drift and split in panel (b) of Fig 3.24 as the observations shown in panel (d) of Fig 3.22. With 15 minutes more running, panel (c) and even later panel (d) of Fig 3.24 exhibit a violent filamentation and the blobs slide down along two legs, displaying all kinds of dynamics. We observed this dynamics and filamentation as well in panel (f) and panel (g) of Fig 3.22. Panel (e) in Fig 3.24 shows the following formation of condensations and their movement to the chromosphere, as observed in Panel (h) of Fig 3.22. At time around 9 hours and 47 minutes, the majority of the cool plasma already fell into the underlying chromosphere and diminished in the corona like panel (f) of Fig 3.24.

Although the time of the total duration of the event in our 3D simulation is around two hours, less than half of the duration in the above observation, the filamentation and dynamics of both are rather similar. The difference in duration could be caused by different length by the coronal loops, which strongly affect the descending time of the blobs, or differentaspects of the actual magnetic topology could also affects the duration time, e.g dips at the apex, and height of the loops. Our 3D simulation depicts a highly similar event as observed in the reality. It allows to study the details of the filamentation, condensation and dynamics of the cool plasma in the corona. Fig 3.25 shows some preliminary results about the statistics, e.g the total cool mass of the condensation in panel (a) and the number of filaments in panel (b). The time evolution of the curve of the mass in panel (a) of Fig 3.25 is similar to the one of 2.5D simulation in panel (a) in Fig 3.10, while the total mass in 3D simulation is twice of the 2.5D simulation. However, the numbers of blobs in panel (b) of Fig 3.25 are only half of the one in panel (b) of Fig 3.10. The reason of this difference is that the blobs thought as detached in the 2.5D simulation are actually unseparated in the third dimension in the 3D simulation. Although they look like undergoing nonstop filamentation during the event, they are still connected. In short, the similarity of the overall process of the 3D simulation to the observation ensure that it is worth to study details of the 3D simulation in future work.

3.5 Conclusions

In this chapter we simulate the initial formation and the long-term sustainment of the enigmatic coronal rain phenomenon for the first time in a realistic multi-dimensional magnetic configuration. In the over 80 minutes physical time, we collect enough statistics to quantify blob widths, lengths which average 400 km, 800 km, and the velocity distribution from small values to 65 km s^{-1}. Our virtual coronal rain display features the deformation of blobs into V-shapes, interactions of blobs due to mostly pressure-mediated levitations, and gives the first views on blobs which evaporate in situ, or get siphoned over the apex of the background arcade.Then we extended our earlier simulations of coronal rain to a much longer time with higher resolution. The main new results can be summarized as follows.

1. We find that after the initial formation stage of condensations, expansion rebound shock fronts introduced by fast siphon inflows display a fan-shaped structure, typically. The local conditions of where condensations form influences the detailed dynamics and expansion of these rebound shocks, and can lead to asymmetric expansion fronts or only one-sided expansion shock fronts.
2. We discussed the process of establishing a structured prominence-coronal-transition-region (PCTR) around coronal rain condensations. The strong radiation loss at the boundary of blobs results in local dips in the gas pressure structure at the blob boundary where the temperature sharply rises from 0.01 MK to a coronal temperature of 0.5 MK.
3. By extending our 2.5D simulation to a longer time of 6 hours, we obtain a secondary cycle of coronal rain in the simulation. This secondary cycle confirms the deductions from previous 1D simulations and observations that by providing consistent and enough energy, coronal rain can form a secondary cycle or even more.
4. We study the condensation rate in our 2.5D simulation and find the growth of cool mass in the corona to show a good correlation especially with the faster growth rate in the length of condensations in the direction perpendicular to the field lines. This indicates that the growth of cool mass is dominated by the onset of runaway cooling in neighbouring loops. This significantly exceeds the rates obtained in studies of this growth rate in 1D models, purely along field lines, as we also need to understand the expansion speed of onset of runaway cooling in neighbouring loops. By performing detailed quantitative analysis, we also find that no matter what happens in the corona, a constant heating in the chromosphere keeps on evaporating a certain amount of hot plasma into the corona, establishing a mass cycle.
5. We look into the impact of declining blobs on the transition region, and find that their rebound shocks can spread as upflows from one footpoint to another footpoint. Following the rebound shocks, evaporation driven upflows with a slower velocity refill the loops and heat them to 2.3 MK again.
6. Plenty of counter-streaming flows are found in our simulation, and we demonstrated several reasons for forming these flows. One is that the extremely

low gas pressure area between two neighbouring coronal rain blobs drives strong siphon flows towards it. These shear flows accompany the blobs until they fall into the transition region.

7. The counter-streaming flows also in return influence the deformation of the blobs, which can break into several segments, starting from an elongated one.

At the end we also show a preliminary result of our 3D simulation which still needs further analysis but shows an overall agreement with the real coronal rain.

Chapter 4

Modelling of Reflective Propagating Slow-mode Wave in a Flaring Loop

"He who aims to be a man of complete virtue in his food does not seek to gratify his appetite, nor in his dwelling place does he seek the appliances of ease; he is earnest in what he is doing, and careful in his speech; he frequents the company of men of principle that he may be rectified: such a person may be said indeed to love to learn."
—Confucius

Quasi-periodic propagating intensity disturbances have been observed in large coronal loops in EUV images over a decade, and are widely accepted to be slow magnetosonic waves. However, spectroscopic observations from Hinode/EIS revealed their association with persistent coronal upflows, making this interpretation debatable. In this chapter, we perform a 2.5D magnetohydrodynamic simulation to imitate the chromospheric evaporation and the following reflected patterns in a flare loop. Our model encompasses the corona, transition region, and chromosphere. The results appeared as Fang et al. (2015b).

4.1 Background

The study of magnetohydrodynamic (MHD) waves in the solar atmosphere is an independent tool to understand the energy release processes, particle acceleration or heating mechanisms and to diagnose the plasma parameters indirectly by coronal seismology (Roberts, 2000; De Moortel and Nakariakov, 2012; Liu and Ofman, 2014). MHD seismology was successfully applied in estimating the coronal magnetic field (Nakariakov and Ofman, 2001), transverse loop structuring (Goossens et al., 2002; Aschwanden et al., 2003), polytropic index and thermal conduction coefficient (Van Doorsselaere et al., 2011b), and the magnetic topology of sunspots (Yuan et al., 2014a,b).

Standing longitudinal slow-mode oscillations were first discovered in the Doppler shift of hot emission lines with formation temperature greater than 6 MK, by the Solar Ultraviolet Measurements of Emitted Radiation (SUMER) spectrograph onboard the Solar and Heliospheric Observatory (SOHO) (Wang et al., 2002, 2003a,b; Wang, 2011). Similar Doppler-shift oscillations have been detected by Yohkoh/BCS in even hotter emission lines of S XV and Ca XIX, with formation temperature 12∼14 MK (Mariska, 2005, 2006). The oscillations are strongly damped within a couple of periods and are usually observed in association with the soft X-ray brightenings or even up to M-class flares (Wang et al., 2007).

Excitation of slow magnetoacoustic oscillations in hot coronal loops has been intensively studied theoretically. The compressible nature of the longitudinal oscillations and their long periods led to their interpretation in terms of standing slow magnetoacoustic oscillations damped due to thermal conduction (Ofman and Wang, 2002). In order to explain the observed damping time of the oscillations and demonstrate the robustness of this interpretation, several authors included other physical effects (Nakariakov et al., 2004; Tsiklauri et al., 2004; Taroyan et al., 2005; Selwa et al., 2005, 2007; Taroyan et al., 2007; Gruszecki and Nakariakov, 2011), accounting for viscosity, multi-dimensional geometry, stratification, nonlinear steepening, and mode coupling.

Quasi-periodic pulsations (QPP) observed in solar and stellar flares have been intensively studied for several decades (Nakariakov and Melnikov, 2009; Anfinogentov et al., 2013). The origin of QPPs still remains unclear, but one of the widely accepted theories is the modulation of QPP by magnetohydrodynamic (MHD) oscillations. Short period (sub-minute) oscillations are believed to be induced by fast mode waves, while those with periods of tens of seconds are ascribed to modulations by slow mode MHD waves (e.g. Van Doorsselaere et al., 2011a). Coronal MHD oscillations are directly seen in various bands with modern instruments with high temporal and spatial resolution, which provide researchers with MHD wave diagnostics to identify physical conditions in flaring sites and mechanisms operating in them.

Recently, the Solar Dynamics Observatory (SDO)/Atmospheric Imaging Assembly (AIA) provided high temporal and spatial resolution observations of slow waves in the solar corona. The first simultaneous observations of the electron density and EUV intensity oscillations were reported by Kim et al. (2012) through Nobeyama 17 GHz

and AIA 335Å channels, respectively. Kumar et al. (2013) reported the first direct observation of a propagating EUV disturbance (i.e., slow mode wave) in hot coronal arcade loops captured only in the AIA 131 and 94 channels. The wave was excited by an impulsive flare which occurred at one of the footpoints of the arcade loops. It showed multiple reflections between the opposite footpoints of the arcade loops (Kumar et al., 2013, 2015).

The observed properties of these oscillations match the SUMER Doppler-shift oscillations associated with slow magnetoacoustic waves. However, Wang (2011) interprets the SUMER Doppler-shift oscillations as standing slow waves due to the associated intensity variations, which show roughly a quarter-period phase delay to the Doppler signal in some cases.

4.2 Governing Equations and Initial Setup

Our numerical setup includes gravity, anisotropic thermal conduction and radiative cooling and parametrized heating terms, in a domain of -40 Mm $\leq x \leq$ 40 Mm and 0 $\leq y \leq$ 50 Mm. The governing equations are as follows:

$$\frac{\partial \rho}{\partial t} + \nabla \cdot (\rho \mathbf{v}) = 0, \tag{4.1}$$

$$\frac{\partial (\rho \mathbf{v})}{\partial t} + \nabla \cdot \left(\rho \mathbf{v}\mathbf{v} + p_{tot}\mathbf{I} - \frac{\mathbf{B}\mathbf{B}}{\mu_0} \right) = \rho \mathbf{g}, \tag{4.2}$$

$$\frac{\partial E}{\partial t} + \nabla \cdot \left(E\mathbf{v} + p_{tot}\mathbf{v} - \frac{\mathbf{v} \cdot \mathbf{B}}{\mu_0}\mathbf{B} \right) = \rho \mathbf{g} \cdot \mathbf{v} + \nabla \cdot (\vec{\kappa} \cdot \nabla T) - Q + H, \tag{4.3}$$

$$\frac{\partial \mathbf{B}}{\partial t} + \nabla \cdot (\mathbf{v}\mathbf{B} - \mathbf{B}\mathbf{v}) = 0, \tag{4.4}$$

where $T, \rho, \mathbf{B}, \mathbf{v}$, and $\mathbf{I}$ are respectively temperature, density, magnetic field, velocity, and unit tensor. The total energy density is $E = p/(\gamma - 1) + \rho v^2/2 + B^2/2\mu_0$ and the total pressure is $p_{tot} \equiv p + B^2/2\mu_0$; $\mathbf{g} = g_0 R_\odot^2/(R_\odot + y)^2 \hat{y}$ is the solar surface gravitational acceleration with g_0 as $-274\,\mathrm{m/s^2}$; H and Q are respectively the heating and radiative loss terms; $\vec{\kappa}$ is the thermal conductivity tensor. Assuming a 10:1 abundance of hydrogen and helium of completely ionized plasma, we obtain $\rho = 1.4 m_\mathrm{p} n_\mathrm{H}$, where m_p is the proton mass and n_H is the number density of hydrogen. We use the ideal gas law $p = 2.3 n_\mathrm{H} k_\mathrm{B} T$ with the ratio of specific heats $\gamma = 5/3$. We adopt $Q = 1.2 n_\mathrm{H}^2 \Lambda(T)$ as the radiative loss function for optically thin emission (Colgan et al., 2008). Below 10,000 K, we set $\Lambda(T)$ to vanish because the plasma there is optically thick. The term containing $\vec{\kappa} = \kappa_{||} \hat{\mathbf{b}}\hat{\mathbf{b}}$ quantifies the anisotropic thermal conduction along the magnetic field lines with the Spitzer conductivity $\kappa_{||}$ as $10^{-6} T^{5/2}$ erg cm^{-1} s^{-1} K$^{-3.5}$. The flux of anisotropic thermal conduction has a ceiling, -sign$(\nabla T) 5 \phi \rho c_s^3$ as the saturated flux, and c_s is the isothermal sound speed. The correction factor $\phi = 1$ is set according to the values suggested for the coronal plasma (Giuliani, 1984, Fadeyev et al., 2002, and references therein).

We employ a linear force-free magnetic field for the initial magnetic configuration, which is characterised by a constant cut-of-plane angle θ_0 as follows:

$$B_x = -B_0 \cos\left(\frac{\pi x}{L_0}\right) \sin\theta_0 \exp\left(-\frac{\pi y \sin\theta_0}{L_0}\right) ,$$

$$B_y = B_0 \sin\left(\frac{\pi x}{L_0}\right) \exp\left(-\frac{\pi y \sin\theta_0}{L_0}\right) ,$$

$$B_z = -B_0 \cos\left(\frac{\pi x}{L_0}\right) \cos\theta_0 \exp\left(-\frac{\pi y \sin\theta_0}{L_0}\right) , \tag{4.5}$$

with $\theta_0 = 30^\circ$, the angle between the arcade and the neutral line ($x = 0, y = 0$). $L_0 = 80$ Mm is the horizontal size of our domain, and we adopt $B_0 = 50$ G.

For the initial thermal structure, we set a uniform temperature of 10,000 K below a height of 2.7 Mm and choose a temperature profile with height ensuring a constant vertical thermal conduction flux (i.e., $\kappa \partial T/\partial y = 2 \times 10^5$ erg cm^{-2} s^{-1}) above this height as used in Fang et al. (2013) and Xia et al. (2012). The initial density is then derived by assuming hydrostatic equilibrium with a number density of 1.2×10^{15} cm^{-3} at the bottom and the initial velocity field of all plasma is static. We employ a background heating rate decaying exponentially with height into the whole system all the time, $H_0 = c_0 \exp\left(-\frac{y}{\lambda_0}\right)$ where $c_0 = 10^{-4}$ erg cm^{-3} s^{-1} and $\lambda_0 = 50$ Mm. This heating is meant to balance the radiative losses and heat conduction related losses of the corona in its equilibrium state. With the above initial setup, the whole system now is out of thermal equilibrium. Therefore, we integrate the governing equations until the above configuration reaches a quasi-equilibrium state at 72 minutes after initialisation. Then we reset the time of the system back to zero for the next stage of simulation. As a result, the final relaxed state of the system is identified as the time when the maximal residual velocity in the simulation is less than 5 km s^{-1}. Panel (a), (b) and (c) in Fig. 4.1 show the number density, temperature and AIA 131 Å of the relaxed system, respectively.

We use the MPI-parallelized Adaptive Mesh Refinement Versatile Advection Code *MPI-AMRVAC* (Keppens et al., 2012; Porth et al., 2014; Keppens and Porth, 2014) to run the simulation. An effective resolution of 1024×640 or an equivalent spatial resolution of 79 km in both directions is obtained through four AMR levels. Considering the left and right physical boundary, density, energy, y and z momentum components, B_y and B_z are set as symmetric, while v_x and B_x are taken antisymmetric to ensure zero face values. In the bottom boundary ghost cells, we use the primitive variables $(\rho, \mathbf{v}, p, \mathbf{B})$ to set all velocity components antisymmetric to enforce both no-flow-through (vertical) and no-slip (horizontal), while the $\mathbf{B}$ are fixed to the initial analytic expressions of equation (4.5), and the stratification of density is kept at pre-determined values from the initial condition, as well as the pressure. For the top conditions, we set all velocity components as antisymmetric, and adopt a discrete pressure-density extrapolation from the top layer pressure with a maximal temperature $T_{top} = 2 \times 10^6$ K.

4.2.1 Imaging and Spectroscopic Modelling

To synthesize the observational features of SDO/AIA channels, we calculated the AIA temperature response function $K_a(n_e, T)$[DN cm^5 s^{-1}]. The detail of the forward modelling method, can be found in Yuan et al. (2015). The source of the forward modelling code (FoMo) is available at https://wiki.esat.kuleuven.be/FoMo. Then we assume that the flux $F_\alpha(x, y)$[DN s^{-1}] will be integrated along the LOS for a width of W =1 Mm,

$$F_\alpha(x, y) = K_\alpha(n_e, T)n_e^2 \times \mathrm{W}. \tag{4.6}$$

We synthesized the AIA 94, 131 Å channel emission which could image the flare loop at 6.4 MK and 10 MK, respectively, and the AIA 304 Å channel emission line which would represent the transition region and top chromosphere (0.05 MK).

Furthermore, we synthesized the extreme ultraviolet (EUV) emission intensity I_{λ_0} [ergs cm^{-2}] of a specific spectral line λ_0 for optically thin plasma along LOS for a width of W =1 Mm. The details of the method can also be found in Yuan et al. (2015) and Antolin and Van Doorsselaere (2013), and the intensity is given by

$$I_{\lambda_0} = \frac{A_b}{4\pi} G_{\lambda_0}(n_e, T)n_e^2 \times \mathrm{W}, \tag{4.7}$$

where A_b is the abundance of the emitting element relative to hydrogen, and G_{λ_0} [ergs cm^{-3} s^{-1}] is the contribution function that contains the terms relative to atomic physics, as a look-up table for SUMER Fe XIX 1118.1 Å line in which most spectroscopic observations of standing slow waves were performed (Wang, 2011).

4.2.2 Triggering the Flare and Chromosphere Evaporation

The flare is triggered by a finite duration heat pulse defined by the function H_1 located at the right footpoint between $x = 22, 24$ Mm as the formula below (note that the heating rate H in Eq.(4.3) is $H = H_0 + H_1$). In our simulation, the heat pulse is controlled by $f(t)$, which starts at time $t = 0$ and switches off at $t = 180$ seconds. The energy input by H_1 is around 3×10^{28} erg s^{-1}, with an assumed thickness of 1 Mm along the third axis. This energy input is suitable for a normal solar flare energy release. The energy of H_1 is quickly transported by thermal conduction to plasma at the footpoints.

$$H_1 = c_1 \exp(-(y - y_c)^2/\lambda^2) f(t) \quad \text{if} \quad A(x_1, 0) < A(x, y) < A(x_2, 0) \tag{4.8}$$

$$A(x, y) = \frac{B_0 L_0}{\pi} \cos\left(\frac{\pi x}{L_0}\right) \exp\left(-\frac{\pi y \sin\theta_0}{L_0}\right), \tag{4.9}$$

$$f(t) = \begin{cases} t/30 & 0 \le t < 30 \quad \mathrm{s} \\ 1 & 30 \le t < 150 \quad \mathrm{s} \\ (180 - t)/30 & 150 \le t < 180 \quad \mathrm{s} \end{cases} \tag{4.10}$$

where $c_1 = 16$ erg cm^{-3} s^{-1}, $y_c = 3$ Mm, $\lambda^2 = 10$ Mm^2, $x_1 = 24$ Mm, and $x_2 = 22$ Mm. The heat pulse is located close to the loop footpoint, i.e. ≈ 0.3 Mm above

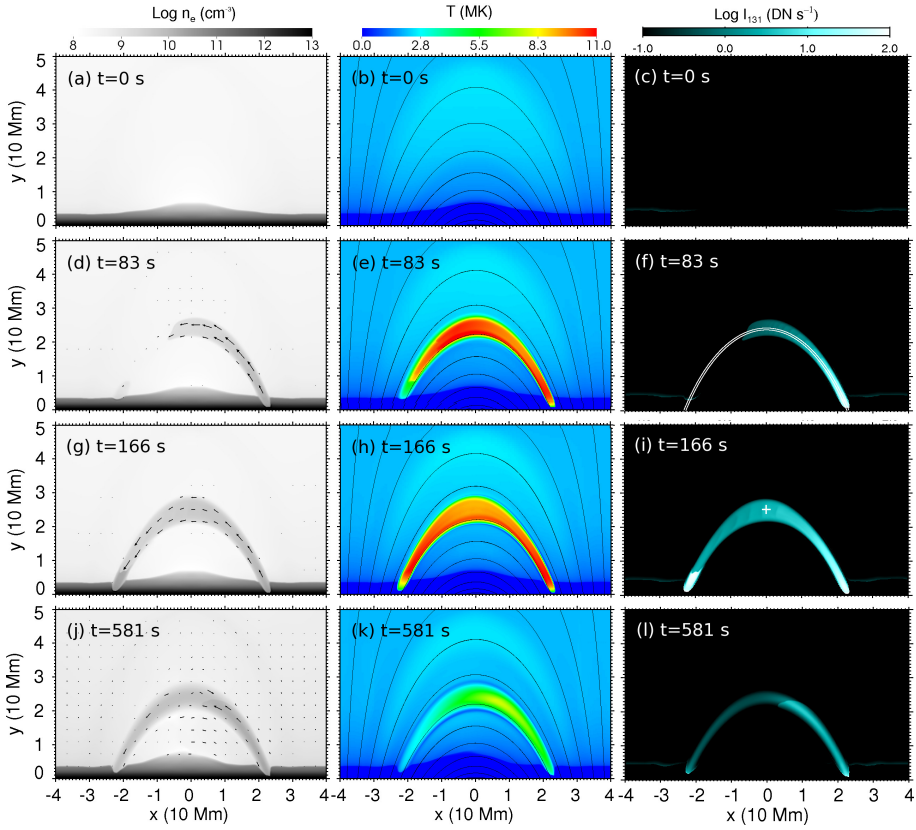

Figure 4.1: Temporal evolution of number density (left column), temperature (middle column), and synthesized AIA 131 Å emission (right column) images at $t \approx 0$, 83, 166 and 581 seconds, respectively. The arrows in the left column mark the velocities and directions of the local plasma. The white lines in panel (f) denotes a fixed loop, defined by a field line with a fixed width of 1200 km. The cross in the panel (i) illustrates the initial location of the particle tracer ($x = 0$ Mm, $y = 25$ Mm).

the transition region mimicking the footpoint heating by dissipated non-thermal particles. $A(x, y)$ is the magnetic potential depending on the location and decaying exponentially with height. Because the magnetic potential along a single magnetic field line is constant, we only add extra heating H_1 at one foot of a magnetic flux tube consisting of the magnetic field lines identified by $A(x, y)$ in the range of $x_1 < x < x_2$. The large ratio between c_1 and c_0 as 1.6×10^5 highlights the extremely violent energy release of the solar flare.

4.3 Results and Discussion

With the number density and temperature maps from the simulation, and the methods briefly presented in §4.2, we can calculate the synthesized emission maps for both AIA and SUMER. We now discuss this simulation in more details. The three columns in Fig. 4.1 display the temporal evolution of number density, temperature and synthesized AIA 131 Å emission intensity maps at $t \approx 0$, 83, 166 and 581 seconds, respectively. The extra flare heating H_1 at the right footpoint ($x = 23$ Mm) imitates the explosive energy release with accumulated relativistic particles, suddenly dissipated in the upper chromosphere and transition region. This enormous energy heats the cold chromospheric plasma (around 0.02 MK) to an average temperature around 10 MK, as presented by the panel (e). The heated plasma is strongly evaporated into the confined loop as shown in panel (d). The velocities of the plasma are represented by the arrows in panel (d), (g) and (j), which show the directions of plasma movement. Compared with panel (d) and (e), panel (f) indicates that the synthesized emission in AIA 131 Å channel is dominated by the density distribution rather than the temperature distribution. The front of the evaporated hot flow violently impacts the left footpoint ($x = -23$ Mm) at $t \approx 163$ seconds with a speed up to 600 km/s. After the violent impact on the chromosphere, a reflected pattern rises up towards the loop apex as shown in panel (g), (h) and (i) at $t \approx 166$ seconds. The AIA 131 Å emission is mainly sensitive to 10 MK plasma. Still, there are subtle effects noted from comparing panel (h) and (i): the left footpoint of the loop has a strong synthesized AIA 131 Å emission in panel (i), but this would not be expected from the local temperature in panel (h). This strong emission is caused by the high compression and heating in the left footpoint, due to the wave impact. At $t \approx 446$ seconds, the reflected pattern spreads back to the right footpoint ($x = 23$ Mm). Then panel (j) at $t \approx 581$ seconds represents the second reflection rising from the right footpoint and shows that the average density in the whole confined heated loop is clearly higher than at the beginning (panel (a)). Although the maximum of temperature in panel (k) decreases to around 8.5 MK, we still could observe the reflected pattern in AIA 131 Å emission in panel (l).

In order to quantify and study these reflected patterns, we extracted a loop drawn by the white lines in panel (f) of Fig. 4.1. This fixed loop is defined by a field line identified at the start of the simulation, with a fixed width of 1200 km. We plot average values of the number density, temperature and synthesized AIA 131 Å emission inside this loop to time-distance maps in panel (a), (b) and (c) of Fig. 4.2, respectively. The zero and end points along s (vertical) axis in Fig. 4.2 mean the left footpoint ($x = -23$

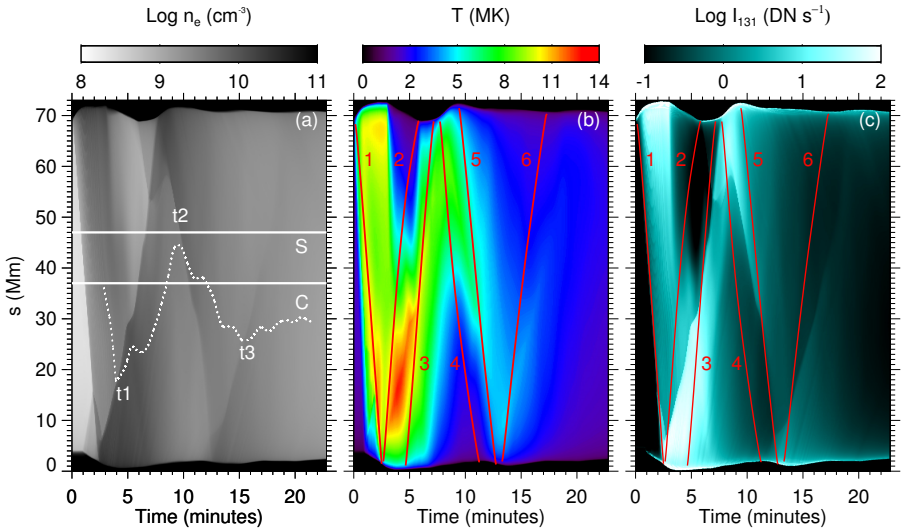

Figure 4.2: Values of number density, temperature and the synthesized AIA 131 Å emission inside the loop shown as time-distance maps are displayed in panel (a), (b) and (c) , respectively. The six red solid lines in panel (b) and (c) show the paths of virtual particles propagating at the local sound speed. The dotted line in panel (a) shows the temporal evolution of the actual Lagrangian particle tracer. Position S and C are used to analyse the light curves in Fig. 4.4 and 4.6, respectively. t1, t2 and t3 indicate the times at which the tracer particle changes its direction.

Mm) and right footpoint ($x = 23$ Mm) in the domain, respectively. The reflected patterns are clearly seen as ridges in all three panels. We add a particle tracer at $t \approx 166$ seconds to trace and observe the movement of the plasma, especially when the reflected patterns sweep over it. The location of the particle tracer ($x = 0, y = 25$ Mm) is marked by a white cross in panel (i) of Fig. 4.1. The temporal evolution of the particle tracer movement is shown as the dotted line in panel (a) of Fig. 4.2. Because the third row of Fig. 4.1 shows the moment when the front of the initial excited flow impacts the left footpoint ($s = 2$ Mm) and the particle tracer is on the tail of the flow, the initial velocity of the particle tracer is towards the left footpoint ($s = 2$ Mm). The particle moves downwards in panel (a) of Fig. 4.2 until it is swept over by the reflected pattern at $t \approx 235$ seconds (this is t1), then it turns around towards the right footpoint ($s = 70$ Mm). As shown in panel (a), the path of the particle displays three turnings (t1, t2 and t3), meaning that it is swept over by the reflected patterns three times. Although the particle is clearly in sync with the reflected patterns, the speed of the tracer is slower than the reflected patterns. The particle tracer behaves like a pendulum, where it is seen to oscillate back and forth, induced by the reflected

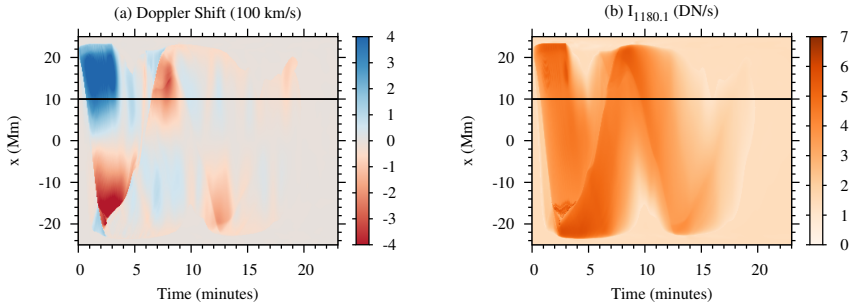

Figure 4.3: Doppler shift oscillations revealed by the synthesized SUMER Fe XIX line emission maps: Panel (a) shows time series of Doppler shift in Fe XIX along a top view slit and panel (b) shows time series of the Fe XIX line intensity. The black full lines show the location of position S used in Fig. 4.2 in this top slit view, and are used to analyse the light curves in Fig. 4.4.

patterns.

One important characteristic used by observational studies to identify this kind of solar propagating disturbances as a slow mode magnetosonic wave is the agreement between the estimated coronal sound speeds and speeds of the reflected propagating disturbances. Based on our simulation, we use a more accurate method to verify this agreement. The six red solid lines in panel (b) and (c) of Fig. 4.2 show the paths of an imaginary particle propagating with the local sound speed, calculated by the local plasma temperature. We could consider these lines as paths of sound waves. In panel (c), line 1 represents the route of a sound wave initiated from the right footpoint ($s = 70$ Mm) at the same time when the extra heating H_1 starts. We find that line 1 has a perfect agreement with the initial excited flow from the right footprint ($s = 70$ Mm) to the left footpoint ($s = 2$ Mm) in panel (c). This agreement indicates that the initial excited flow propagates with the sound speed. However, in panel (b) we find that the temperature rises earlier than the arrival of the flow (line 1). That is because of the faster propagation speed of the thermal conduction discontinuity, which also introduces a weak evaporation to slightly increase the density at the left footpoint ($s = 2$ Mm) around $t \approx 1$ minutes as shown in panel (a). Line 2 represents the path of a sound wave propagating from the left footpoint ($s = 2$ Mm) to the right footpoint ($s = 70$ Mm), assumed to set out when the excited flow propagating along line 1 impacts the left footpoint ($s = 2$ Mm). Fig. 4.2 show that there are AIA 131 Å emission, density and temperature changes at the top end of line 2, the right footpoint ($s = 70$ Mm). These increments indicate that a reflected wave propagates along line 2, and impacts to trigger another reflected wave rising from the right footpoint ($s = 70$ Mm). The analysis of line 1 and line 2 confirm that these reflected patterns have a wave component.

However, unlike line 1, the synthesized AIA 131 Å emission of the reflected pattern

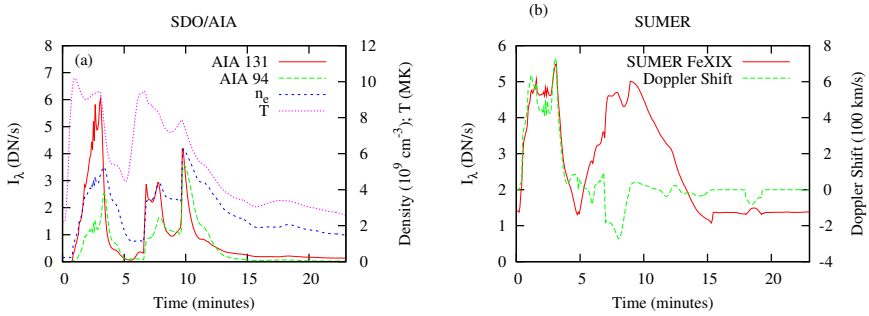

Figure 4.4: Panel (a) shows the temporal evolution of the synthesized AIA 131, 94 Å channel emission, number density and temperature for position S in Fig. 4.2; Panel (b) represents temporal evolution of the synthesized Doppler shift velocity and intensity of SUMER Fe XIX line for the black line in Fig. 4.3.

from the bottom end of line 1 does not behave similarly with line 2 in panel (c) of Fig. 4.2. The reflected pattern propagates slower than the sound wave along line 2, especially the part from the left footpoint ($s = 2$ Mm) to $s = 30$ Mm. Because the initially excited flow from the right footpoint ($s = 70$ Mm) is triggered by a finite duration heating pulse, it relates to flows initiated within the same time range of H_1 from $t = 0$ to $t = 180$ seconds, which is clearly observed in all panels of Fig. 4.2. As a result, the rising reflected pattern at the left footpoint ($s = 2$ Mm) from $t \approx 161$ seconds encounters the rest part of the initially excited flow which still propagates towards the left footpoint ($s = 2$ Mm). Panel (c) shows that this collision delays the propagation of the reflected pattern, indicating that both the excited flow and the reflected pattern contain a mass flow component. Line 3 in panel (c) is another path of a sound wave which arrives at the right footpoint ($s = 70$ Mm) simultaneously with the main part of the reflected pattern. The middle piece of Line 3 shows that after passing through the “collision" region, the reflected pattern propagates with the sound speed again. As well as for line 1, line 3 in the panel (b) temperature map shows that the thermal conduction discontinuity propagates faster than the sound wave. The behaviours of lines 1, 2 and 3 in panel (b) and (c) indicate these reflected patterns contain both wave and mass flow component. This is also confirmed by the line 4, 5 and 6. All of them tell the same story that the patterns observed in the synthesized AIA 131 Å channel emission is dominated by a repeatable wave component, and modulated by the mass flows where collisions can temporally retard or redirect actual mass flows. Another interesting phenomenon is that the highest temperature in our simulation is not produced initially by the flare heating H_1, but by the collisional compression of two patterns as shown in panel (b).

The slow magnetoacoustic waves observed by Kumar et al. (2015) are thought to be propagating waves, rather than standing waves as observed by Wang (2011). The standing waves have a unique characteristic, a quarter-period phase delay between the associated intensity variations and the Doppler signal. In Fig. 4.3, panel (a) shows a

top slit view of the Doppler shift in the synthesized SUMER Fe XIX line, and panel (b) shows a top slit view of the intensity of the synthesized SUMER Fe XIX line emission. A top slit view means visual LOS from the top of the system ($y = 50$ Mm) to the bottom of the system ($y = 0$ Mm). The top view of the Doppler shift in panel (a) shows clear reflected patterns, and so does the intensity map in panel (b). We extract the black line ($x = 10$ Mm) in Fig. 4.3 to compare the synthesized Doppler signal and the associated intensity variations and identify which kind of wave we have in the simulation. Although the top slit views of the synthesized SUMER Fe XIX line emission integrate the quantities from the top to the bottom, the synthesized SUMER Fe XIX line only observes plasma with temperature greater than 6 MK, which only exists in the heated loop. So we extract position S in panel (a) of Fig. 4.2 to compare with the black line in Fig. 4.3, which is located at the same position in the confined loop length. Panel (a) of Fig. 4.4 shows the temporal evolution of the synthesized AIA 131, 94 Å channel emission, number density and temperature of position S, and panel (b) represents the temporal evolution of the synthesized Doppler shift velocity and intensity of SUMER Fe XIX line of the black line, which is close to the right footpoint. So the second and third peaks of light curve in panel (a) do not mean peaks of the exactly second and third periods of waves, actually they indicate the time before and after the wave impact. The reason why the third peak is stronger than the second peak in AIA channels is that I_{λ_0} of AIA channels are remarkably affected by the density. Since after the impact, the front of wave-flow reflects back and collides with the tail of itself and the density at position S increases as shown in panel (a) as well as by the third peak of AIA channels. We find that the number density, temperature and both AIA channels emission have an in-phase relationship as seen in panel (a), while the same is quantitatively true for Doppler shift and intensity in SUMER Fe XIX line in panel (b). This suggests that these reflected patterns are propagating waves which show an in-phase relationship (Sakurai et al., 2002), rather than standing slow waves which show a quarter-period phase lag between velocity and intensity disturbances (Wang et al., 2003a; Yuan et al., 2015). The difference between AIA 131, 94 Å channel emission is because AIA 131 Å emission is more sensitive to higher temperatures around 10 MK, while AIA 94 Å emission is sensitive to the temperature around 6.5 MK. This also explains the reason why AIA 94 Å emission increases more than AIA 131 Å emission at the third peak in panel (a) of Fig. 4.3, because at that moment the temperature decreases below 9 MK, while the density increases.

Fig. 4.5 shows the plasma speed (red solid line), number density (blue dotted line), and local sound speed (green dashed line) at $t \approx$83, 166, 250, 332 seconds along the loop defined by two white lines in panel (f) of Fig. 4.1. The left end on the X-axis means the left footpoint and the right end of X-axis counterpart to the right footpoint of the loop. As shown in Fig. 4.1, the excited waves travels from the right footpoint to the left footpoint, then reflects back to the right footpoint. In panel (a) of Fig. 4.5, the plasma speed (red solid line) shows a clear steep profile at its front. In addition, the speed of the downstream is faster than the local sound speed, while the speed of the upstream is slower than the local sound speed. We can infer the first excited pattern in panel (a) is a shock wave. Panel (b) shows the moment shortly after the

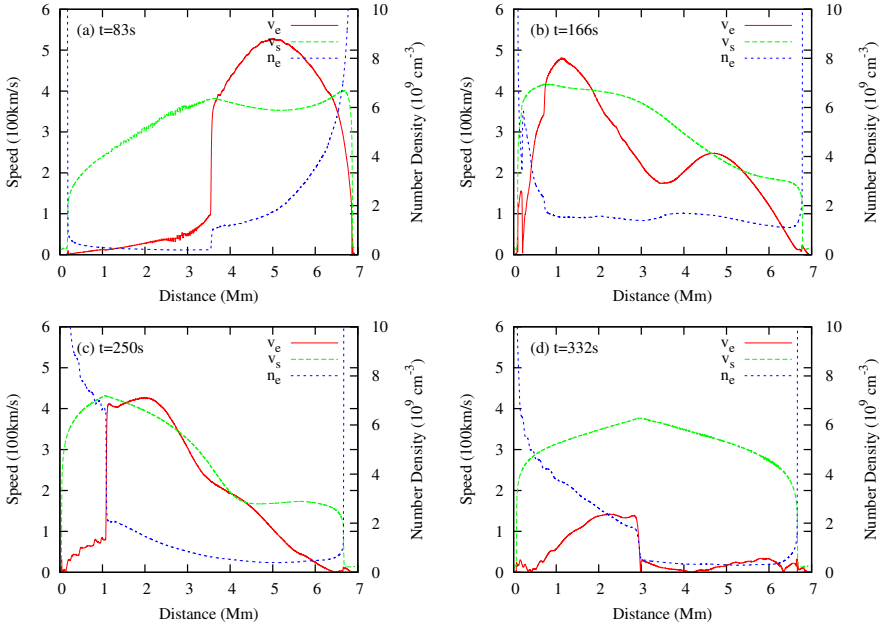

Figure 4.5: The plasma speed (red solid line), number density (blue dotted line), and local sound speed (green dashed line) at $t \approx$83, 166, 250, 332 seconds along the loop in panel (f) of Fig. 4.1.

first excited pattern hits the left footpoint. Later on in panel (c), the pattern starts to reflect back to the right footpoint along the loop.

In panel (b) and (c), the speed of downstream is no longer faster than the local sound speed. This indicates these patterns in panel (b) and (c) are waves, not shock waves anymore. Finally in panel (d), the plasma speed is slower than the local sound speed everywhere. The panels in Fig. 4.5 demonstrates that the first excited pattern is a shock wave, and the following reflected patterns are not shocks anymore. In any case, the wave is highly non-linear, and thus shock dissipation may play a role (Verwichte et al., 2008).

In order to calculate the period of the reflected patterns, we extract another position C shown in panel (a) of Fig. 4.2. The position C is located at the apex of the loop, so the light curve of AIA 131, 94 Å emissions of slice C in panel (a) of Fig. 4.6 can reveal the more correct half period of the reflected patterns rather than panel (a) of Fig. 4.4. We identify three peaks of the reflected patterns based on the light curves of AIA 131, 94 Å emission which all show strong damping afterwards. The time intervals between the three peaks are 285 and 360 seconds, so the total period would be 570 seconds and 720 seconds. Compared with the observational result in Kumar et al. (2015), with

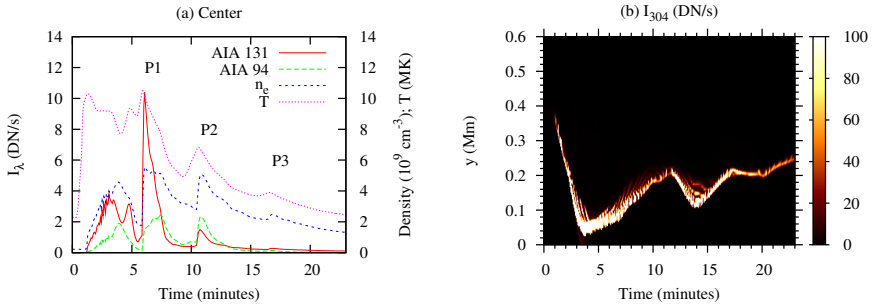

Figure 4.6: Panel (a) shows the temporal evolution of the synthesized AIA 131, 94 Å channel emission, number density and temperature for position C which locates at the loop apex as shown in Fig. 4.2; Panel (b) a Time-Distance plot illustrates the height and intensity variation of the plasma at the left footpoint (x= -23 Mm) imaged by the AIA 304 Channel.

409 seconds for the period, the period in our simulation is longer. There are plenty of factors which could influence the period, such as the length and structure of the loop, the temperature inside the loop, etc. One possible reason for the longer period is the slower sound speed in our simulation, indicating that the reality should have even higher temperatures (greater than 10 MK). The period increase in our simulation is mainly affected by the large cooling, i.e the strong thermal conduction which is mainly responsible for the quick loop temperature decreases (Ofman and Wang, 2002; Wang et al., 2003b) and little leakage of waves across the loop when the wave-flows impact the footpoint. When the temperature decreases during the propagation, and so does the sound speed, the period of the reflected patterns increases. The transition region at $x = -23$ Mm, shown by the AIA 304 Å emission in panel (b) of Fig. 4.6, also displays an oscillation. This oscillation indicates the height variation of the transition region, due to the impact from reflected patterns. The height variation actually traces the energy and momentum exchange between coronal and chromospheric regions as leaked by the reflected patterns. Yu et al. (2013) reports that quasi-periodic wiggles of microwave zebra pattern (ZP) structures can be associated with fast magnetoacoustic oscillations in a flaring active region. This oscillation of transition region associated with slow mode waves in our simulation may be observed in the future as well.

4.4 Conclusion

In this chapter, we performed a 2.5D MHD simulation to imitate the chromospheric evaporation and the following reflected patterns in a flare loop. We demonstrated that the periodic intensity variations captured by the synthesized AIA 131 and 94 Å emission images match well with previous observations (Kumar et al., 2013, 2015).

With a particle tracer, we confirmed that these reflected patterns contain a clear wave component, in their sound speed like propagation. Through predicted paths of sound waves, we also found that these reflected patterns are dominated by the wave component while modulated by mass flows. To sum up, the reflected patterns observed in our simulation contain both slow waves and mass flows.

With the synthesized Doppler shift velocity and intensity maps in SUMER Fe XIX line emission, we confirmed that these reflected patterns are propagating slow mode waves rather than standing slow mode waves in our simulation, due to the in-phase relationship between Doppler shift and intensity.

From the light curves of the synthesized AIA 131, 94 Å emission, we estimated the period of oscillations which increases from 570 seconds to 720 seconds during the observed three periods. The increase of the period was due to the decreasing loop temperature and sound speed, caused by the strong cooling. The height variation of the transition region shown in the synthesized AIA 304 Å map may exhibit similar oscillations, correlated with the reflected patterns. This could be searched for in future observations.

4.5 Another Run in Mandal et al. (2016)

We also collaborate with Mandal et al. (2016) by performing a new run with different parameters from the real observational case (Mandal et al., 2016). From the observations we obtained an estimate about the speed of the wave propagating through the loop. The density and temperature values of the loop plasma are also calculated using DEM analysis using the AIA data. Now we use a numerical simulation with the obtained loop length, density and temperature as the input parameters, to model the observations. Our simulation uses a 2.5D thermodynamic magnetohydrodynamic model as in Fang et al. (2015b) which includes gravity, anisotropic thermal conduction and radiative cooling. The box domain in the simulation is taken as -60 Mm $\leq x \leq$ 60 Mm and $0 \leq y \leq 80$ Mm in order to obtain a comparable loop length of ≈140 Mm as estimated from our observations.

The energy release from the flare is mimicked by a finite duration heat pulse H_1 located at the right footpoint between $x = 39, 40$ Mm.

$$H_1 = c_1 \exp(-(y - y_c)^2/\lambda^2) f(t) \quad \text{if} \quad A(x_1, 0) < A(x, y) < A(x_2, 0) \tag{4.11}$$

$$A(x, y) = \frac{B_0 L_0}{\pi} \cos\left(\frac{\pi x}{L_0}\right) \exp\left(-\frac{\pi y \sin\theta_0}{L_0}\right), \tag{4.12}$$

$$f(t) = \begin{cases} t/30 & 0 \leq t < 30 \quad \text{s} \\ 1 & 30 \leq t < 150 \quad \text{s} \\ (180 - t)/30 & 150 \leq t < 180 \quad \text{s} \end{cases} \tag{4.13}$$

where $\lambda^2 = 10$ Mm^2, $x_1 = 40$ Mm, $y_c = 3$ Mm and $x_2 = 39$ Mm. The pulse is switched on only for a time $t = 0$ to $t = 180$ seconds. We set the c_1 to 12 erg cm^{-3} s^{-1} in

our simulation input. We introduced the anisotropic thermal conduction along the magnetic field lines with the Spitzer conductivity $\kappa_{||}$ defined as $10^{-6}T^{5/2}$ erg cm^{-1} s^{-1} $K^{-3.5}$. We use radiative loss function of the form Q=1.2$n_H^2\Lambda$(T) above 10,000 K (optically thin plasma) (Colgan et al., 2008). Below that value, we set Λ(T) to be zero. Density, energy, momentum components (y and z), magnetic field (B_y and B_z) are set as symmetric, while v_x and B_y are taken antisymmetric at the left and right boundaries.

To synthesize the observational features of SDO/AIA channel we use the FoMo code[1] to perform forward modelling. Using the AIA temperature response function (Boerner et al., 2012) the FoMo code converts the density to the intensity. We have synthesized the AIA 94 Å channel emission which has a characteristics log(T) ≈6.8 .

4.5.1 Analysis of the synthesized data

From views on Fig 4.7 we see that the wave propagates back and forth before fading out of the loop. Figure 4.7 shows the time evolution of the density,temperature and the AIA 94 Å channel intensity. To see the wave propagation along the loop we put an artificial slit tracing the loop (red dashed line in the left panel of Fig. 4.8) to generate the time-distance map (right panel of Fig. 4.8). From the map we see clear signatures of reflection in the AIA 94 Å intensity images. The positions of the local maxima were identified along each ridge and fitted with a linear function to calculate the propagation speed.

The two yellow dashed lines represent the fitted straight line for the forward and the reflected wave having speeds 499 km s^{-1} (line A) and 357 km s^{-1}(line B) (with errors less than 15 km s^{-1}). These speeds compare very well with the average speeds we estimated from time-distance created using the XRT and AIA images. Here we must emphasize the fact that the simulation is 2D, so there is no projection effect unlike our observations. This consistency of the speed value validate our result obtained from DEM analysis which shows a temperature ≈ 10MK.

To estimate the damping of the observed propagating intensity, we take a similar approach as for the observational data analysis. The time evolution of the intensity profile averaged over a chosen box (shown as yellow rectangle in Fig 4.8) is plotted as blue solid curve in Figure 4.9. We fit the function on that profile and obtained the best fit curve, shown as the red dotted line. The period and the damping times are 10.1 minutes and 10.3 minutes respectively.

[1] `https://wiki.esat.kuleuven.be/FoMo/FrontPage`

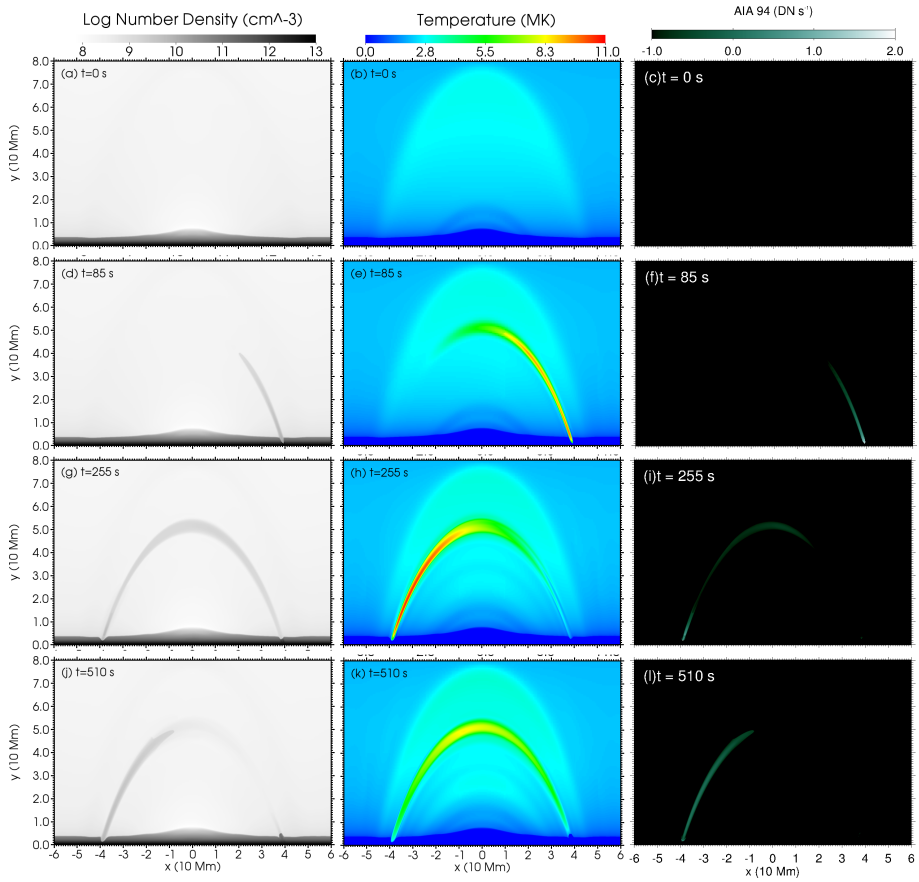

Figure 4.7: Snapshots showing the density (n_e), temperature (T) and the AIA 94 Å intensity images respectively at different time of the simulation. The association of the intensity enhancement with the density and temperature is seen very clearly.

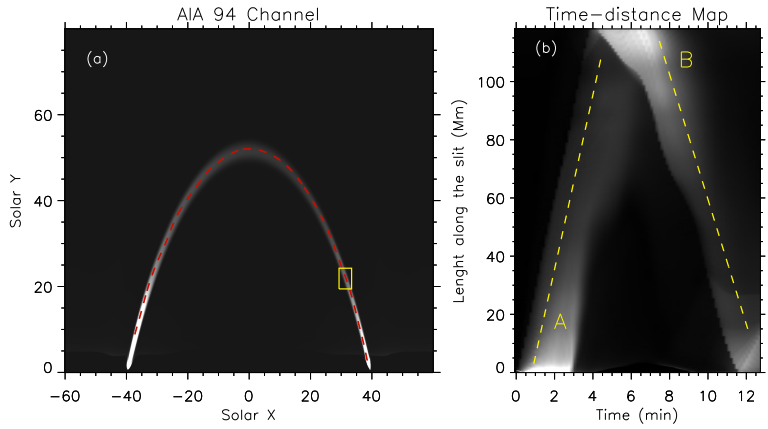

Figure 4.8: Panel (a) shows the time averaged synthesized AIA 94 Å intensity image. The red dashed line indicates the artificial slit used for constructing the time-distance map. The yellow rectangular box is used to generate the intensity profile shown in Fig 4.9. Panel (b) shows the time-distance map with the fitted straight (in yellow) line used for speed calculation.

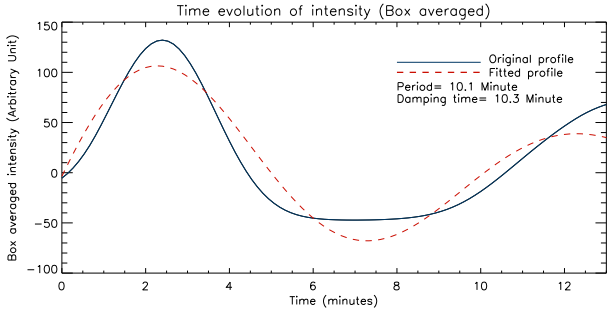

Figure 4.9: The blue solid line shows the intensity profile averaged over the chosen yellow box. The fitted damped sinusoidal function is shown with the red dashed line. The period and the damping time is printed on the panel.

Chapter 5

Kelvin-Helmholtz Instability for Loop-top Hard X-ray Sources in Solar Flares

"When agreements are made according to what is right, what is spoken can be made good. When respect is shown according to what is proper, one keeps far from shame and disgrace. When the parties upon whom a man leans are proper persons to be intimate with, he can make them his guides and masters."

—Confucius

In this chapter we propose a model for the formation of loop-top hard X-ray (HXR) sources in solar flares through the Inverse Compton mechanism, scattering the surrounding soft X-ray (SXR) photons to higher energy HXR photons. We simulate the consequences of a flare-driven energy deposit in the upper chromosphere in the impulsive phase of single loop flares. We will investigate how the Kelvin-Helmholtz instability (KHI) is triggered by the chromosphere evaporation flows, then search possible method to generate HXR photons through the non-thermal particles accelerated and trapped by the KHI in the loop top. The result is submitted to ApJ and currently undergoing review with a positive first referee report.

5.1 Background

Solar flares, the most powerful events of solar activity, are thought to be the result of magnetic reconnection occuring in the corona and can release in excess of 10^{32} ergs of energy in a matter of minutes (Hudson, 2011). A substantial fraction of the released energy is transported downwards along the magnetic loop by non-thermal particles (Brown, 1971), or by thermal conduction (Fletcher et al., 2011) and/or Poynting flux (Fletcher and Hudson, 2008). The bulk of the non-thermal particle energy gets deposited in the chromosphere via Coulomb collisions (Brown, 1971). This produces HXR emission via non-thermal bremsstrahlung primarily at the footpoints of the loops (Hoyng et al., 1981) and is referred to as the thick target model (Brown, 1971). The overpressure resulting from the tremendous energy deposit drives an upward mass flow at a speed up to hundreds of kilometers per second, known as chromospheric evaporation. The affected coronal loops thereby get filled with hot plasma and these loops are then observed via thermal SXR emission (Veronig et al., 2005). Since the intensity of non-thermal bremsstrahlung depends on the ambient plasma density, HXR emission is usually too weak to occur in the corona, where the densities are generally much lower. Only in a few cases, coronal densities seem to be high enough such that HXR sources can be clearly observed in the corona (e.g. Veronig and Brown, 2004). Nevertheless, several examples clearly show HXR emission from coronal sources (Frost and Dennis, 1971; Hudson, 1978; Masuda et al., 1994; Tomczak, 2001; Krucker and Lin, 2008). Arguably the most famous example showed an impulsive non-thermal HXR source appearing above thermal SXR loops by Masuda et al. (1994), and this confirmed the overlying cusp geometry of the standard solar flare model (Shibata and Magara, 2011). However, although several somewhat similar events have been observed since (Tomczak, 2001; Krucker and Battaglia, 2014), the Masuda event has not proven to be typical of solar flares in general. Most events with both SXR and HXR coronal sources show less separation ($\leq$3,500 km) between the thermal SXR loops and the coronal HXR source, and many thermal events in a loop that fills by chromospheric evaporation even show co-spatial non-thermal emission (Tomczak, 2001; Krucker and Lin, 2008).

Therefore, the emission mechanism of these rare loop-top HXR events might be different from the Masuda flare, which was interpreted as a partially thick target up in the corona, by injecting non-thermal particles into the cusp of a magnetic trap (Fletcher, 1995). Korchak (1971) concluded that an Inverse Compton (IC) contribution might sometimes be significant, particularly in the low ambient density conditions relevant to these loop-top HXR events. With an ambient coronal number density of 10^9 cm^{-3}, Inverse Compton radiation eventually dominates over bremsstrahlung in the 10-100 keV photon energy range (Krucker et al., 2008). Furthermore, these bright, concentrated, loop-top coronal HXR sources show time variation in the order of tens of seconds to minutes and are most prominent during the rise of the thermal emission (Krucker et al., 2008). Therefore, the populations of loop-top non-thermal particles which possibly contribute to HXR emission by IC could be accelerated in turbulent plasma conditions, which also helps to trap particles (Turkmani et al., 2006; Krucker et al., 2008). In such cases, the accelerator is then believed to be co-spatial with the

coronal HXR source.

In this chapter, we propose a model which generates turbulence in the loop top by the Kelvin-Helmholtz instability (KHI). The KHI is triggered by the chromospheric evaporation flows from asymmetric flare energy deposition at both loop footpoints. The KHI, produced when two fluid flows have a velocity shear across an interface or finite extent region (Chandrasekhar, 1961), is able to form vortices which can trigger further fine-scale reconnection and turbulence in a magnetized plasma (Keppens et al., 1999; Baty and Keppens, 2002; Henri et al., 2013). KHI is well studied at fast-slow stream interfaces in a variety of solar structures (Heyvaerts and Priest, 1983; Andries and Goossens, 2001), and has even been observed directly in connection with a coronal mass ejection (Foullon et al., 2011) or in solar prominences (Berger et al., 2010). Here, we will demonstrate KHI in a single suddenly footpoint-heated loop.

The chapter is then organized as follows: in §5.2 we describe the numerical setup; in §5.3 we show the results of the simulation and discuss the implications, and conclusions are drawn in §5.4.

5.2 Initial Setup

Our numerical setup, initial and boundary conditions follow the model in Fang et al. (2015b), using a single-fluid magnetohydrodynamic (MHD) plasma description on a two-dimensional (2D) domain of size 80 by 50 Mm (in x-y). We initialize with a linear force-free magnetic field given by

$$\begin{aligned} B_x &= -B_0 \cos\left(\frac{\pi x}{L_0}\right) \sin\theta_0 \exp\left(-\frac{\pi y \sin\theta_0}{L_0}\right) , \\ B_y &= B_0 \sin\left(\frac{\pi x}{L_0}\right) \exp\left(-\frac{\pi y \sin\theta_0}{L_0}\right) , \\ B_z &= -B_0 \cos\left(\frac{\pi x}{L_0}\right) \cos\theta_0 \exp\left(-\frac{\pi y \sin\theta_0}{L_0}\right) , \end{aligned} \tag{5.1}$$

with the angle $\theta_0 = 30^\circ$ between the arcade and the neutral line ($x = 0, y = 0$) and the horizontal size of our domain setting $L_0 = 80$ Mm. The differences from Fang et al. (2015b) is that we adopt a higher magnetic field strength of $B_0 = 80$ G, instead of 50 G in Fang et al. (2015b), in order to have a realistic flare loop magnetic field as deduced from observations. For the initial thermal structure, we set a uniform temperature of 10,000 K below a height of 2.7 Mm and fix the temperature variation to ensure a constant vertical thermal conduction flux $\kappa \partial T/\partial y = 2 \times 10^5$ erg cm^{-2} s^{-1} above this height, identical to Fang et al. (2015b). The initial density is derived from hydrostatic equilibrium with a number density of 1.2×10^{15} cm^{-3} at the bottom. There is no flow to start with. To obtain a self-consistent thermally structured corona, we augment this setup with a background heating rate decaying exponentially with height, $H_0 = c_0 \exp\left(-\frac{y}{\lambda_0}\right)$ where $c_0 = 10^{-4}$ erg cm^{-3} s^{-1} and $\lambda_0 = 80$ Mm. This heating appears as a source term in the energy equation, and is meant to balance the radiative losses and anisotropic heat conduction related losses of the corona in its

equilibrium state. With this initial setup, we integrate the governing MHD equations until the above configuration reaches a quasi-equilibrium state at 144 minutes after initialisation, when we reset time to zero. In the remainder of this paper, we only discuss the stage following this relaxation phase. The relaxed state of the system is reached when the maximal residual velocity is less than 10 km s^{-1} in the entire domain. Panel (a) and (b) in Fig. 5.1 show the number density and temperature of the relaxed system, respectively. The right frame (c) quantifies the corresponding thermal X-ray emission as explained further on, which is completely absent for this relaxed initial state. We use the MPI-parallelized Adaptive Mesh Refinement Versatile Advection Code *MPI-AMRVAC* (Keppens et al., 2012; Porth et al., 2014; Keppens and Porth, 2014) with an effective resolution of 1024×640 or an equivalent spatial resolution of 79 km in both directions, obtained through four adaptive mesh refinement levels.

5.3 Triggering Chromosphere Evaporation

The effect of the solar flare is modeled by its chromospheric energy deposit, handled as a finite duration heat pulse located at the loop footpoints. The temporal evolution of the heat pulse is controlled by $f(t)$, a piecewise linear ramping function to add and complete the sudden heating within 180 seconds. The asymmetric energy input is handled by a function $g(x)$, which sets the ratio of energy deposition at the left footpoint ($x < 0$) to the right footpoint ($x > 0$) to 0.8. Both functions appear in the heat pulse functional form $H_1(x, y, t)$ (which is an extra energy source term in addition to the background heating $H_0(x, y)$) specified as

$$\begin{aligned} H_1 &= c_1 \exp(-(y - y_c)^2/\lambda^2) f(t) g(x) \\ &\text{if} \quad A(x_1, 0) < A(x, y) < A(x_2, 0) \end{aligned} \tag{5.2}$$

$$A(x, y) = \frac{B_0 L_0}{\pi} \cos\left(\frac{\pi x}{L_0}\right) \exp\left(-\frac{\pi y \sin\theta_0}{L_0}\right) , \tag{5.3}$$

$$f(t) = \begin{cases} t/30, & 0 \le t < 30 \quad \text{s} \\ 1, & 30 \le t < 150 \quad \text{s} \\ (180 - t)/30, & 150 \le t < 180 \quad \text{s} \end{cases} \tag{5.4}$$

$$g(x) = \begin{cases} 1, & x > 0 \\ 0.8, & x < 0 \end{cases} \tag{5.5}$$

where $c_1 = 80$ erg cm^{-3} s^{-1}, $y_c = 3$ Mm, $\lambda^2 = 10$ Mm^2, $x_1 = 24$ Mm, and $x_2 = 23$ Mm. The heat pulse is located close to the loop footpoint, i.e. ≈ 0.3 Mm above the transition region, mimicking the footpoint heating by dissipated non-thermal particles. The energy of H_1 is expected to be quickly transported by thermal conduction away from the footpoints. The extra heating H_1 is active at two footpoints of a single magnetic loop or flux tube consisting of the magnetic field lines identified by the out-of-plane magnetic vector potential component $A(x, y)$ in the range of $x_2 < |x| < x_1$.

5.3.1 Estimating the thermal X-ray emission

We estimate the thermal X-ray emission in the 3-12 keV photon energy range based on the spatial distributions of density and temperature obtained from the simulation by the method described in Pinto et al. (2015) and also implemenetd in the open source forward modelling code FoMo available at `https://wiki.esat.kuleuven.be/FoMo`. The corresponding continuum thermal X-ray photon flux density of a fully ionized hydrogen plasma emitted at the photon energy $h\nu$ is defined as

$$I\left(h\nu,T\right)=I_0\frac{\mathrm{EM}}{h\nu\sqrt{k_bT}}g_{ff}\left(h\nu,T\right)\exp\left(-\frac{h\nu}{k_bT}\right)\,, \tag{5.6}$$

$$g_{ff}\left(h\nu,T\right)=\begin{cases}1, & h\nu\lesssim k_bT\\ \left(\frac{k_bT}{h\nu}\right)^{0.4}, & h\nu>k_bT\end{cases}\,, \tag{5.7}$$

where EM is the emission measure n^2V of a finite volume V of plasma of number density n and temperature T, the coefficient I_0 is 1.07×10^{-42} for a photon flux measured at a distance of 1 AU, if the photon flux density is expressed in units of photons $\cdot\,\mathrm{cm}^{-2}\cdot\mathrm{s}^{-1}\cdot\mathrm{keV}^{-1}$, and $g_{ff}\left(h\nu,T\right)$ is the Gaunt factor for free-free bremsstrahlung emission. We compute the photon flux density at different photon energies for each individual grid cell, and then integrate the total photon flux density as $DN=\sum I\left(h\nu,T\right)\Delta h\nu$ in the $3<h\nu<12$ keV photon energy range. We use 0.01 keV as $\Delta h\nu$, meaning totally 90 bins in the $3<h\nu<12$ keV energy range. This process leads to the figures shown in Fig. 5.1, right column.

5.4 Asymmetric footpoint heating inducing KHI

The temporal evolution of the number density (left column), temperature (middle column), and synthesized SXR photon fluxes (right column) are shown in Fig. 5.1, covering a timespan of about 4.15 minutes. As described in §2.2, we use H_1 to mimic the flare energy deposited in the upper chromosphere, and the consequent overpressure resulting from H_1 drives upward mass flows at a speed up to 700 km s^{-1}. We also witness a rapid thermodynamic change (due to thermal conduction) in the loop, reaching an extremely hot temperature around 18 MK. These upward chromospheric evaporation flows have been detected directly in imaging sequences as SXR emission propagating toward the loop-top sources (Silva et al., 1997; Liu et al., 2006; Nitta et al., 2012). This is also seen in our simulation, as in panel (f) of Fig. 5.1 (and in the time period before this image, for which we refer to the corresponding movie). In the last several decades, simulations of chromospheric evaporation were mostly carried out with symmetric energy input assumptions on both loop footpoints and these focused mainly on the UV-SXR spectral lines produced by the evaporated plasma (Fisher et al., 1985; Mariska et al., 1989; Yokoyama and Shibata, 2001; Allred et al., 2005; Liu et al., 2009). However, asymmetric energy deposition at footpoints is a much more likely scenario, and could be intrinsic to the acceleration process as pursued by McClements and Alexander (2005). So, in our simulation we assume

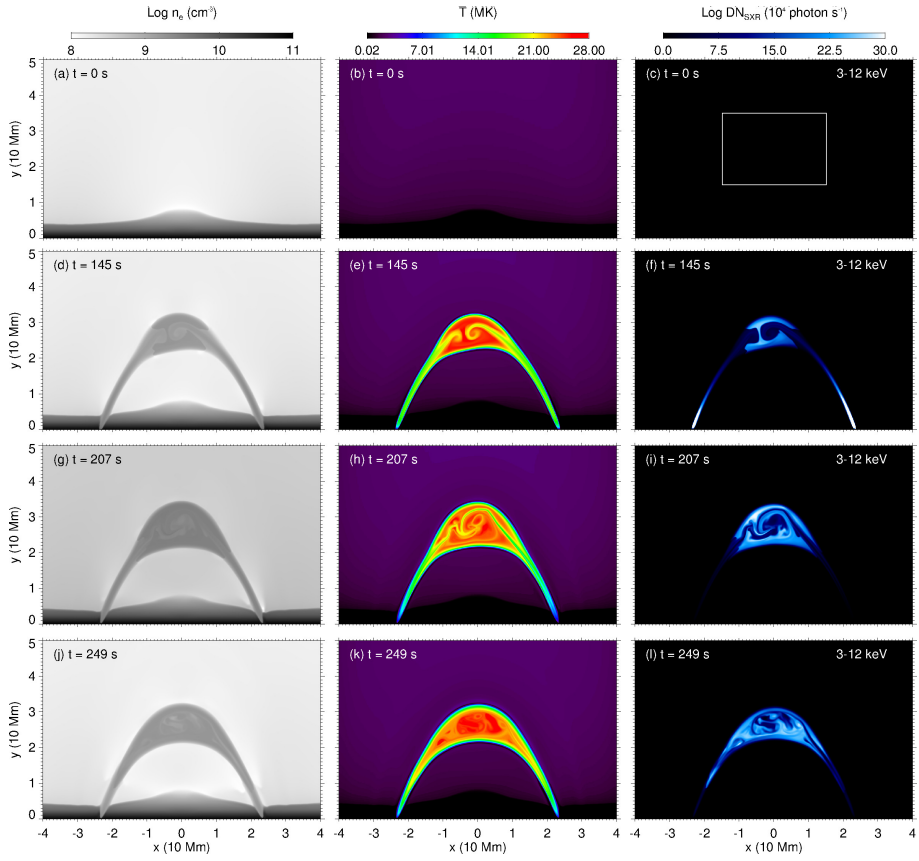

Figure 5.1: Temporal evolution of number density (left column), temperature (middle column), and synthesized SXR photon flux images (right column) at $t \approx 0$, 145, 207 and 249 seconds, respectively. There is an animation (m1.mp4) of Fig. 5.1 available online.

that the deposition of flare energy at two footpoints is slightly asymmetric, with a ratio of 0.8 as described in equation (5). As a result, the right evaporation flow rises quicker and is hotter than the left one as shown in panel (e). The asymmetric energy deposition guarantees that the two evaporation flows will not merely collide at the apex, a situation known to only generate reflected shocks. Panel (e) indeed shows that when our two evaporation flows run into each other asymmetrically, the right one has already crossed the loop apex. In addition, the hotter, right evaporation flow causes a bigger expansion of the loop cross-section in the right half of the loop. This configuration provides the conditions for the formation of shear flows, the trigger of the KHI. As shown in panel (e), right after the collision of both flows, the KHI begins to develop immediately, and the typical vortical structures of the KHI appear and grow up quickly from panel (e) to (g). The development of vortices in a magnetized plasma can further induce small-scale structure to develop, with a potential cascade of energy to establish a turbulent plasma state (Keppens et al., 1999; Baty and Keppens, 2002; Elmegreen and Scalo, 2004; Henri et al., 2013).

Our grid-adaptive simulations offer enough resolution to also capture a number of (numerical) reconnection processes occurring during the vortex development. The left column in Fig. 5.2 shows the temporal evolution of the current distribution perpendicular to the plane (the component J_z) in a color scale, overlaid with contours of the magnetic vector potential which identify magnetic field lines. By the vortical winding up of the field, we obtain locally anti-parallel magnetic field lines and accompanying strong current sheets, all introduced by the KHI as a trigger for local reconnection processes near the apex as shown in panel (c). The resulting magnetic islands keep evolving, merging, and splitting for the following 4 minutes. In fully kinetic simulations of isolated reconnection layers, Drake et al. (2006) demonstrated that the formation of micro-turbulence inside current sheets can act as a non-thermal particle accelerator. Although we only simulated the MHD scales, the mesoscopic (i.e. in between the macro-scale of the loop diameter and the kinetic scales) current sheets in panel (c) have the possibility to form micro-turbulence inside them and accelerate particles very efficiently. Normally, in an open magnetic configuration, such high energy particles escape easily in the order of seconds. In that case, the HXR emission which depends on the density of non-thermal particles cannot achieve a high intensity. However, in our simulation, the accompanying rotating magnetic islands exist on MHD scales for several minutes, so they can trap the accelerated particles during their formation at the loop apex. Note that the local island structures indeed have minute-long lifetime and fine-structure variation, which matches the time scale and variation suggested by the observations for loop-top HXR sources (Krucker et al., 2008).

The observations suggest that the time variation of loop-top HXR sources are most prominent during the rise of the thermal emission, normally observed as SXR emission (Krucker et al., 2008). In order to confirm that the chromospheric evaporation flows not only have the ability to trigger the KHI to establish the preferred looptop site for particle acceleration, but also provide enough SXR photons for the Inverse Compton mechanism producing HXR emission, we calculate the thermal emission of the plasma by the method in §5.3.1 in the energy range of 3-12 KeV, a typical SXR band in

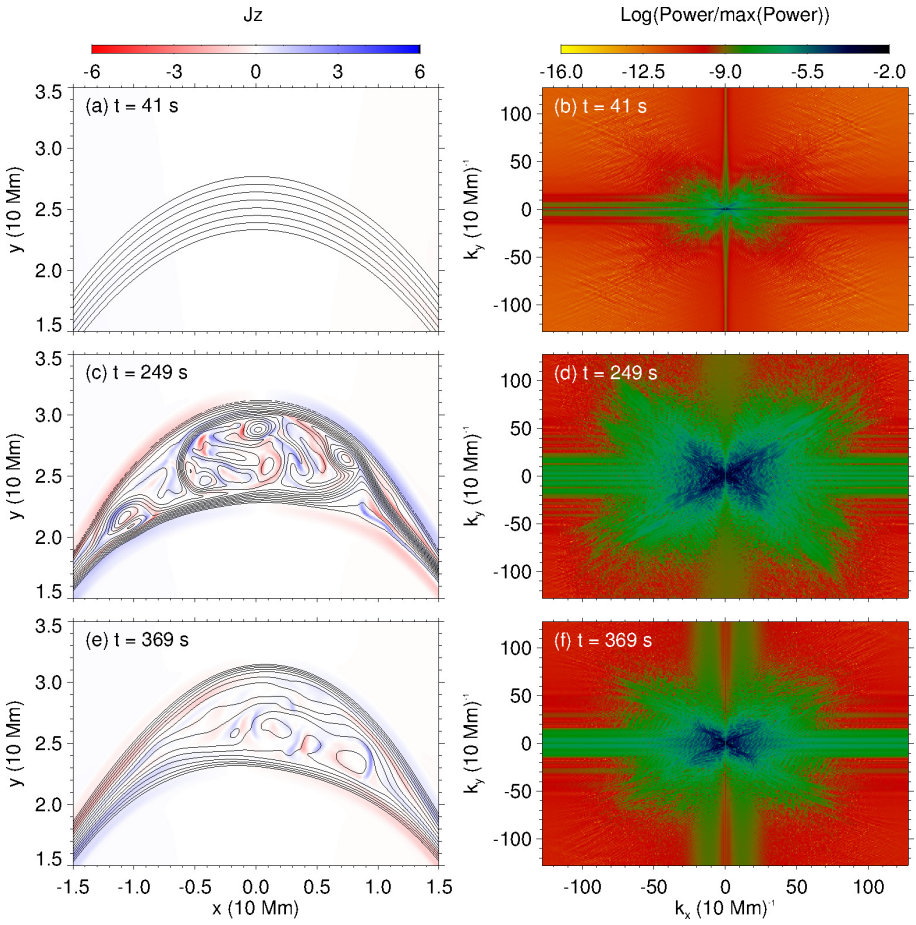

Figure 5.2: For the region in the white rectangle in panel (c) of Fig. 4.1, the temporal evolution of the current J_z perpendicular to the plane, overlaid by contours of magnetic vector potential (left column), and log-scaled power spectrum from Fourier analysis of the J_z images (right column) at $t \approx 41$, 249, and 369 seconds, respectively.

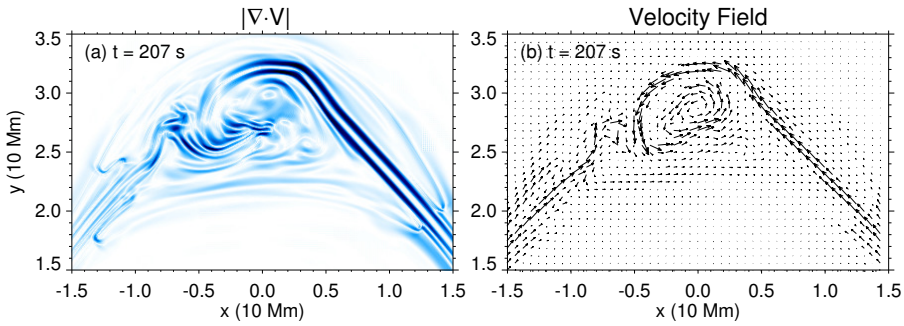

Figure 5.3: At $t \approx 207$ seconds, inside the region shown by the white rectangle in panel (c) of Fig. 4.1, we show in panel (a) the absolute value of the divergence of the plasma velocity and the flow field itself in panel (b).

RHESSI, as shown by the right column in Fig. 5.1. At the initial stage of the flare energy deposition, the SXR emission is concentrated at the two footpoints, and then rises to the apex. Afterwards, the collision between two evaporation flows compresses the plasma at the loop-top area and increases both the number density and temperature there, resulting in a bright loop-top SXR source as shown in panel (f), (i) and (l). The evolution of SXR emission in our simulation not only recovers the previous observational result of SXR emission in flare events (Liu et al., 2006; Veronig et al., 2005), but also indicates the co-spatial and simultaneous relationship between the particle accelerator introduced by the KHI and the generation of SXR photons from thermal emission of hot plasma. Thus, the Inverse Compton emission mechanism has all ingredients to create a HXR source with time order of minutes at the apex.

5.5 Ingredients for non-thermal particle acceleration

The exact nature of particle acceleration in flares is still a matter of debate (Fletcher and Hudson, 2008; Brown et al., 2009), but our simulation supports the suggestion by Krucker et al. (2008) that loop-top non-thermal particles are very likely accelerated and trapped by localised turbulent plasma. Turbulence is the most natural agent for establishing an energy cascade over a large dynamical range, and the corresponding stochastic acceleration models have been widely used for solar flare studies (Miller, 1997; Petrosian and Liu, 2004). We find strong indications of KHI induced turbulence at the apex in our simulation. Such turbulence could be a possible accelerator for non-thermal particles. The acceleration mechanism in turbulence is usually first order Fermi acceleration by shocks and second order Fermi acceleration by stochastic

processes (Fermi, 1949). From our MHD model, we can only argue how shocks and stochastic processes are indeed locally realized. Panel (a) in Fig. 5.3 shows the absolute value of the divergence of the velocity field in the zoomed-in region shown by the white rectangle in panel (c) of Fig. 5.1. This identifies the locations of strong compression, an indication of shock fronts, and suggests that first order Fermi acceleration can take place efficiently there. We also show the flow field itself in panel (b), showing that the island structures seen in Fig. 5.2 are indeed correlated to vortical flow structures. We interpret the fine-structure seen as (not yet fully resolved) turbulence which infers that stochastic acceleration could also play a part in this region as well.

The efficiency of the acceleration process in turbulence strongly depends on the existence of short wavelength structures (or high wave number components). We perform a spatial Fourier analysis on each frame of $J_z(x, y)$ shown in the left column of Fig. 5.2, by forward Fast Fourier Transform procedure (FFT, IDL8.2). With shifting the zero-frequency component to the center of the spectrum, FFT governs the equation as

$$F(k_x, k_y) = \frac{1}{NM} \sum_{x=-N/2}^{N/2} \sum_{y=-M/2}^{M/2} J_z(x, y) \exp\left(-i2\pi \left(\frac{k_x \cdot x}{N} + \frac{k_y \cdot m}{M}\right)\right), \qquad (5.8)$$

which implies the zero point symmetry in wave number domain. We then obtain the corresponding log-scaled power spectrum in the wave number domain in the right column of Fig. 5.2. Before the start of KHI at $t \approx 41$ seconds, panel (b) shows that the distribution of this power spectrum is more centrally peaked at the low wave numbers, in accord with non-existence of small structures then. During the development of the KHI at $t \approx 249$ seconds, panel (d) demonstrates that the distribution of power spectrum spreads out to the larger wave numbers, indicating that smaller scale structures are generated. After the fading of the shear flows and vortices at $t \approx 369$ seconds, the KHI are suppressed by the magnetic field, and panel (f) displays that the power spectrum contracts back into the small wavenumber regime again, meaning that the small structures disappear. The evolution of the power spectrum in the right column of Fig. 5.2 reveals that the KHI does introduce strong turbulence during its evolution at the apex.

5.6 Discussion and conclusion

In this chapter, we propose a new ingredient to the standard model for solar flares, for the rare events where one witnesses the formation of loop-top HXR sources. Our model provides further support to the interpretation that these HXR loop-top sources can occur through the Inverse Compton mechanism scattering the surrounding SXR photons to higher energy. We show that a slight asymmetry between the left-right footpoint deposited energy by non-thermal particles from the reconnection layer developing above the loops is sufficient to establish rapid chromospheric evaporation flows with speeds up to 700 km/s that are liable to Kelvin-Helmholtz instability (KHI) when they meet near the loop apex. As usual in KHI evolutions in magnetized

plasma conditions, vortices form further fine scale structure within, and the turbulence that appears at the apex of loops could be considered as an efficient accelerator for non-thermal particles. The island structures are ideal sites for trapping non thermal particles at the loop-top. We show that our model reproduces the thermal SXR evolution related to the evaporation flows, as well as establishing a pronounced SXR source region in the loop-top. We suggest that locally accelerated non-thermal particles can easily upscatter these thermal SXR photons to HXR photons. This needs to be further investigated by augmenting the MHD scenario demonstrated here, with test particle evolutions to quantify the efficiency of the acceleration process. Our work provides strong support to the role of KHI as a clear trigger of loop-top SXR to HXR emission, during the impulsive phase of single loop flares.

Chapter 6

Summary and Conclusion

The filamentation and dynamics in coronal loops has been observed since the beginning of the last century. It includes prominences, filaments, and later on coronal rain, as well as waves, flares and even CMEs. With the recent launched telescopes and updated ground observatories, the observations of coronal loops depict unpredicted fine and complicated physical structures to us. It becomes evident that the further development of high resolution observations of these coronal phenomena (prominences, coronal rain, solar flares and so on) is a topic of great interest. The aim of this thesis is trying to improve the numerical simulation modelling of the filamentation and dynamics in coronal loops. The main results in this thesis obtained in Chapter 3, 4 and 5 are summarized below.

In Chapter 3, we simulate the initial formation and the long-term sustainment of the enigmatic coronal rain phenomenon for the first time in a realistic 2.5D magnetic configuration. We collect enough statistics to quantify blob widths, lengths which average 400 km, 800 km. We found and discussed the process of establishing a structured prominence-coronal-transition-region (PCTR) around coronal rain condensations. The strong radiation loss at the boundary of blobs results in local dips in the gas pressure structure at the blob boundary where the temperature sharply rises from 0.01 MK to a coronal temperature of 0.5 MK. In an overall time of 6 hours, a secondary cycle of coronal rain in the simulation occurs, which confirms the deductions from previous 1D simulations and observations that by providing consistent and enough energy, coronal rain can form a secondary cycle or even more. Plenty of counter-streaming flows are found in our simulation, and one of the reasons is that the extremely low gas pressure area between two neighbouring coronal rain blobs drives strong siphon flows towards it. These driven shear flows accompany the blobs until they fall into the transition region finally. Actually these counter-streaming flows also in return influence the deformation of the blobs, which can break into several segments, starting from an elongated one. At the end we also show a preliminary

result of our 3D simulation to anticipate the further analysis and study of the coronal rain phenomenon.

In Chapter 4, a 2.5D MHD simulation of chromospheric evaporation is performed and the following reflected patterns in a flare loop are clearly observed. The periodic intensity variations captured by the synthesized AIA 131 and 94 Å emission images match well with previous observations (Kumar et al., 2013, 2015). With a particle tracer, we confirmed that these reflected patterns contain a clear wave component, in their sound speed like propagation. Through comparison with predicted paths of sound waves, we also found that these reflected patterns are dominated by the wave component while modulated by mass flows. To sum up, the reflected patterns observed in our simulation contain both slow waves and mass flows. With the synthesized Doppler shift velocity and intensity maps in SUMER Fe XIX line emission, we confirmed that these reflected patterns are propagating slow mode waves rather than standing slow mode waves in our simulation, due to the in-phase relationship between Doppler shift and intensity. From the light curves of the synthesized AIA 131, 94 Å emission, we estimated the period of oscillations which increases from 570 seconds to 720 seconds during the observed three periods. The increase of the period was due to the decreasing loop temperature and sound speed, caused by the strong cooling.

In Chapter 5, we propose a new ingredient to the standard model for solar flares, for the rare events where one witnesses the formation of loop-top HXR sources. We show that a slight asymmetry between the left-right footpoint deposited energy by non-thermal particles from the reconnection layer developing above the loops is sufficient to establish rapid chromospheric evaporation flows with speeds up to 700 km/s that are liable to Kelvin-Helmholtz instability (KHI) when they meet near the loop apex. As usual in KHI evolutions in magnetized plasma conditions, vortices form further fine scale structure within, and the turbulence that appears at the apex of loops could be considered as an efficient accelerator for non-thermal particles. The island structures are ideal sites for trapping non thermal particles at the loop-top. We show that our model reproduces the thermal SXR evolution related to the evaporation flows, as well as establishing a pronounced SXR source region in the loop-top. We suggest that locally accelerated non-thermal particles can easily upscatter these thermal SXR photons to HXR photons. Our work provides strong support to the role of KHI as a clear trigger of loop-top SXR to HXR emission, during the impulsive phase of single loop flares.

Now we move to our future plans for the above studies. For the formation and dynamics of the coronal rain, we will study already obtained 3D simulations. These were done as using a linear force-free magnetic topology which are commonly seen in quiet Sun area. Since most of the coronal rain are observed in active region, we also want to explore a different setup to mimic a magnetic topology in an active Sun area. An approach to obtain the magnetic field in an active area is using a bipolar map at the chromosphere and extrapolating it into the corona. We need to simulate the magnetic topologies, while we turn on the heating to evaporate the chromosphere plasma. An even more ambitious approach is using the realistic magnetogram map

from observations instead of adopting the bipolar topology, and then extrapolate from this underlying field into the corona. This will need to handle realistic conditions provided by extrapolating from the realistic magnetograms. Chapter 5 presents the idea that the particles accelerated and trapped in the apex of a flaring loop could be able to scatter the surrounding SXR photons to form a HXR source as in some observation. This idea could be an ingredient to the standard model for solar flares and does not conflict with any existing elements in the standard model. However, this needs to be further investigated by augmenting the MHD scenario demonstrated here, with test particle evolutions to quantify the efficiency of the acceleration process.

Bibliography

C. E. Alexander, R. W. Walsh, S. Régnier, J. Cirtain, A. R. Winebarger, L. Golub, K. Kobayashi, S. Platt, N. Mitchell, K. Korreck, B. DePontieu, C. DeForest, M. Weber, A. Title, and S. Kuzin. Anti-parallel EUV Flows Observed along Active Region Filament Threads with Hi-C. *ApJ*, 775:L32, Sept. 2013. doi: 10.1088/2041-8205/775/1/L32. pages 42, 66

H. Alfvén. Magneto hydrodynamic waves, and the heating of the solar corona. *MNRAS*, 107:211, 1947. doi: 10.1093/mnras/107.2.211. pages 11

J. C. Allred, S. L. Hawley, W. P. Abbett, and M. Carlsson. Radiative Hydrodynamic Models of the Optical and Ultraviolet Emission from Solar Flares. *ApJ*, 630:573–586, Sept. 2005. doi: 10.1086/431751. pages 103

J. Andries and M. Goossens. Kelvin-Helmholtz instabilities and resonant flow instabilities for a coronal plume model with plasma pressure. *A&A*, 368:1083–1094, Mar. 2001. doi: 10.1051/0004-6361:20010050. pages 101

S. Anfinogentov, V. M. Nakariakov, M. Mathioudakis, T. Van Doorsselaere, and A. F. Kowalski. The Decaying Long-period Oscillation of a Stellar Megaflare. *ApJ*, 773:156, Aug. 2013. doi: 10.1088/0004-637X/773/2/156. pages 82

S. K. Antiochos and J. A. Klimchuk. A model for the formation of solar prominences. *ApJ*, 378:372–377, Sept. 1991. doi: 10.1086/170437. pages 13, 16, 17, 42

S. K. Antiochos, P. J. MacNeice, D. S. Spicer, and J. A. Klimchuk. The Dynamic Formation of Prominence Condensations. *ApJ*, 512:985–991, Feb. 1999. doi: 10.1086/306804. pages 13, 16, 42

S. K. Antiochos, P. J. MacNeice, and D. S. Spicer. The Thermal Nonequilibrium of Prominences. *ApJ*, 536:494–499, June 2000. doi: 10.1086/308922. pages 16

P. Antolin and L. Rouppe van der Voort. Observing the Fine Structure of Loops through High-resolution Spectroscopic Observations of Coronal Rain with the CRISP Instrument at the Swedish Solar Telescope. *ApJ*, 745:152, Feb. 2012. doi: 10.1088/0004-637X/745/2/152. pages 15, 42, 47, 48, 50, 51, 52, 59, 63

P. Antolin and T. Van Doorsselaere. Line-of-sight geometrical and instrumental resolution effects on intensity perturbations by sausage modes. *A&A*, 555:A74, July 2013. doi: 10.1051/0004-6361/201220784. pages 85

P. Antolin and E. Verwichte. Transverse Oscillations of Loops with Coronal Rain Observed by Hinode/Solar Optical Telescope. *ApJ*, 736:121, Aug. 2011. doi: 10.1088/0004-637X/736/2/121. pages 42, 51

P. Antolin, K. Shibata, and G. Vissers. Coronal Rain as a Marker for Coronal Heating Mechanisms. *ApJ*, 716:154–166, June 2010. doi: 10.1088/0004-637X/716/1/154. pages 15, 17, 42, 43, 47, 48, 51, 63

M. J. Aschwanden. Revisiting the Determination of the Coronal Heating Function from Yohkoh Data. *ApJ*, 559:L171–L174, Oct. 2001. doi: 10.1086/323788. pages 17

M. J. Aschwanden. *Physics of the Solar Corona. An Introduction*. Praxis Publishing Ltd, Aug. 2004. pages 8

M. J. Aschwanden and R. W. Nightingale. Elementary Loop Structures in the Solar Corona Analyzed from TRACE Triple-Filter Images. *ApJ*, 633:499–517, Nov. 2005. doi: 10.1086/452630. pages 51

M. J. Aschwanden and D. Tsiklauri. The Hydrodynamic Evolution of Impulsively Heated Coronal Loops: Explicit Analytical Approximations. *ApJS*, 185:171–185, Nov. 2009. doi: 10.1088/0067-0049/185/1/171. pages 17

M. J. Aschwanden, R. W. Nightingale, J. Andries, M. Goossens, and T. Van Doorsselaere. Observational Tests of Damping by Resonant Absorption in Coronal Loop Oscillations. *ApJ*, 598:1375–1386, Dec. 2003. doi: 10.1086/379104. pages 82

J. N. Bahcall, W. F. Huebner, S. H. Lubow, P. D. Parker, and R. K. Ulrich. Standard solar models and the uncertainties in predicted capture rates of solar neutrinos. *Reviews of Modern Physics*, 54:767–799, July 1982. doi: 10.1103/RevModPhys.54.767. pages 2

H. Baty and R. Keppens. Interplay between Kelvin-Helmholtz and Current-driven Instabilities in Jets. *ApJ*, 580:800–814, Dec. 2002. doi: 10.1086/343893. pages 101, 105

J. M. Beckers. Motions in the Chromosphere near Sunspots. *Australian Journal of Physics*, 15:327, Sept. 1962. doi: 10.1071/PH620327. pages 14, 15

T. E. Berger, G. Slater, N. Hurlburt, R. Shine, T. Tarbell, A. Title, B. W. Lites, T. J. Okamoto, K. Ichimoto, Y. Katsukawa, T. Magara, Y. Suematsu, and T. Shimizu. Quiescent Prominence Dynamics Observed with the Hinode Solar Optical Telescope. I. Turbulent Upflow Plumes. *ApJ*, 716:1288–1307, June 2010. doi: 10.1088/0004-637X/716/2/1288. pages 101

P. Boerner, C. Edwards, J. Lemen, A. Rausch, C. Schrijver, R. Shine, L. Shing, R. Stern, T. Tarbell, A. Title, C. J. Wolfson, R. Soufli, E. Spiller, E. Gullikson, D. McKenzie, D. Windt, L. Golub, W. Podgorski, P. Testa, and M. Weber. Initial Calibration of the Atmospheric Imaging Assembly (AIA) on the Solar Dynamics Observatory (SDO). *Sol. Phys.*, 275:41–66, Jan. 2012. doi: 10.1007/s11207-011-9804-8. pages 95

V. Bommier and J. L. Leroy. Global Pattern of the Magnetic Field Vectors Above Neutral Lines from 1974 to 1982: Pic-du-Midi Observations of Prominences. In D. F. Webb, B. Schmieder, and D. M. Rust, editors, *IAU Colloq. 167: New Perspectives on Solar Prominences*, volume 150 of *Astronomical Society of the Pacific Conference Series*, page 434, 1998. pages 37

J. C. Brown. The Deduction of Energy Spectra of Non-Thermal Electrons in Flares from the Observed Dynamic Spectra of Hard X-Ray Bursts. *Sol. Phys.*, 18:489–502, July 1971. doi: 10.1007/BF00149070. pages 19, 22, 100

J. C. Brown, R. Turkmani, E. P. Kontar, A. L. MacKinnon, and L. Vlahos. Local re-acceleration and a modified thick target model of solar flare electrons. *A&A*, 508: 993–1000, Dec. 2009. doi: 10.1051/0004-6361/200913145. pages 107

M. Čada and M. Torrilhon. Compact third-order limiter functions for finite volume methods. *Journal of Computational Physics*, 228(11):4118 – 4145, 2009. ISSN 0021-9991. doi: http://dx.doi.org/10.1016/j.jcp.2009.02.020. URL `http://www.sciencedirect.com/science/article/pii/S0021999109000953`. pages 33, 46, 76

H. Carmichael. A Process for Flares. *NASA Special Publication*, 50:451, 1964. pages 21

B. W. Carroll and D. A. Ostlie. *An Introduction to Modern Astrophysics*. 1996. pages 2, 4

J. Chae, H. Wang, J. Qiu, P. R. Goode, L. Strous, and H. S. Yun. The Formation of a Prominence in Active Region NOAA 8668. I. SOHO/MDI Observations of Magnetic Field Evolution. *ApJ*, 560:476–489, Oct. 2001. doi: 10.1086/322491. pages 16

S. Chandrasekhar. *Hydrodynamic and hydromagnetic stability*. 1961. pages 101

J. Colgan, J. Abdallah, Jr., M. E. Sherrill, M. Foster, C. J. Fontes, and U. Feldman. Radiative Losses of Solar Coronal Plasmas. *ApJ*, 689:585–592, Dec. 2008. doi: 10.1086/592561. pages 34, 35, 43, 83, 95

R. B. Dahlburg, S. K. Antiochos, and J. A. Klimchuk. Prominence Formation by Localized Heating. *ApJ*, 495:485–490, Mar. 1998. doi: 10.1086/305286. pages 16

A. De Groof, D. Berghmans, L. van Driel-Gesztelyi, and S. Poedts. Intensity variations in EIT shutterless mode: Waves or flows? *A&A*, 415:1141–1151, Mar. 2004. doi: 10.1051/0004-6361:20034252. pages 14

A. de Groof, C. Bastiaensen, D. A. N. Müller, D. Berghmans, and S. Poedts. Detailed comparison of downflows seen both in EIT 30.4 nm and Big Bear Hα movies. *A&A*, 443:319–328, Nov. 2005. doi: 10.1051/0004-6361:20053129. pages 14, 17, 42

I. De Moortel and V. M. Nakariakov. Magnetohydrodynamic waves and coronal seismology: an overview of recent results. *Philosophical Transactions of the Royal Society of London Series A*, 370:3193–3216, July 2012. doi: 10.1098/rsta.2011.0640. pages 82

J. F. Drake, M. Swisdak, H. Che, and M. A. Shay. Electron acceleration from contracting magnetic islands during reconnection. *Nature*, 443:553–556, Oct. 2006. doi: 10.1038/nature05116. pages 105

B. Edlén. The identification of the coronal lines (George Darwin Lecture). *MNRAS*, 105:323, 1945. doi: 10.1093/mnras/105.6.323. pages 10

B. G. Elmegreen and J. Scalo. Interstellar Turbulence I: Observations and Processes. *ARA&A*, 42:211–273, Sept. 2004. doi: 10.1146/annurev.astro.41.011802.094859. pages 105

A. G. Emslie, B. R. Dennis, A. Y. Shih, P. C. Chamberlin, R. A. Mewaldt, C. S. Moore, G. H. Share, A. Vourlidas, and B. T. Welsch. Global Energetics of Thirty-eight Large Solar Eruptive Events. *ApJ*, 759:71, Nov. 2012. doi: 10.1088/0004-637X/759/1/71. pages 18

Y. A. Fadeyev, H. Le Coroller, and D. Gillet. The structure of radiative shock waves. IV. Effects of electron thermal conduction. *A&A*, 392:735–740, Sept. 2002. doi: 10.1051/0004-6361:20020995. pages 83

X. Fang, C. Xia, and R. Keppens. Multidimensional Modeling of Coronal Rain Dynamics. *ApJ*, 771:L29, July 2013. doi: 10.1088/2041-8205/771/2/L29. pages 37, 41, 42, 43, 44, 45, 53, 54, 59, 62, 63, 84

X. Fang, C. Xia, R. Keppens, and T. Van Doorsselaere. Coronal Rain in Magnetic Arcades: Rebound Shocks, Limit Cycles, and Shear Flows. *ApJ*, 807:142, July 2015a. doi: 10.1088/0004-637X/807/2/142. pages 41, 42

X. Fang, D. Yuan, T. Van Doorsselaere, R. Keppens, and C. Xia. Modeling of Reflective Propagating Slow-mode Wave in a Flaring Loop. *ApJ*, 813:33, Nov. 2015b. doi: 10.1088/0004-637X/813/1/33. pages 81, 94, 101

E. Fermi. On the Origin of the Cosmic Radiation. *Physical Review*, 75:1169–1174, Apr. 1949. doi: 10.1103/PhysRev.75.1169. pages 108

G. B. Field. Absorption by Intergalactic Hydrogen. *ApJ*, 135:684–693, May 1962. doi: 10.1086/147312. pages 13

G. B. Field. Thermal Instability. *ApJ*, 142:531, Aug. 1965. doi: 10.1086/148317. pages 13, 16, 41, 61

G. H. Fisher, R. C. Canfield, and A. N. McClymont. Flare loop radiative hydrodynamics. V - Response to thick-target heating. VI - Chromospheric evaporation due to heating by nonthermal electrons. VII - Dynamics of the thick-target heated chromosphere. *ApJ*, 289:414–441, Feb. 1985. doi: 10.1086/162901. pages 103

L. Fletcher. On the generation of loop-top impulsive hard X-ray sources. *A&A*, 303: L9, Nov. 1995. pages 100

L. Fletcher and H. S. Hudson. Impulsive Phase Flare Energy Transport by Large-Scale Alfvén Waves and the Electron Acceleration Problem. *ApJ*, 675:1645-1655, Mar. 2008. doi: 10.1086/527044. pages 100, 107

L. Fletcher, B. R. Dennis, H. S. Hudson, S. Krucker, K. Phillips, A. Veronig, M. Battaglia, L. Bone, A. Caspi, Q. Chen, P. Gallagher, P. T. Grigis, H. Ji, W. Liu, R. O. Milligan, and M. Temmer. An Observational Overview of Solar Flares. *Space Sci. Rev.*, 159:19–106, Sept. 2011. doi: 10.1007/s11214-010-9701-8. pages 19, 100

J. M. Fontenla, E. H. Avrett, and R. Loeser. Energy balance in the solar transition region. II - Effects of pressure and energy input on hydrostatic models. *ApJ*, 377: 712–725, Aug. 1991. doi: 10.1086/170399. pages 44

C. Foullon, E. Verwichte, V. M. Nakariakov, K. Nykyri, and C. J. Farrugia. Magnetic Kelvin-Helmholtz Instability at the Sun. *ApJ*, 729:L8, Mar. 2011. doi: 10.1088/2041-8205/729/1/L8. pages 101

K. J. Frost and B. R. Dennis. Evidence from Hard X-Rays for Two-Stage Particle Acceleration in a Solar Flare. *ApJ*, 165:655, May 1971. doi: 10.1086/150932. pages 100

J. L. Giuliani, Jr. On the dynamics in evaporating cloud envelopes. *ApJ*, 277:605–614, Feb. 1984. doi: 10.1086/161731. pages 83

J. P. Goedbloed, R. Keppens, and S. Poedts. *Advanced Magnetohydrodynamics*. Apr. 2010. pages 26

J. P. H. Goedbloed and S. Poedts. *Principles of Magnetohydrodynamics*. Aug. 2004. pages 26

D. W. Goldsmith. Thermal Effects in the Formation of Loop Prominences. *Sol. Phys.*, 19:86–91, Aug. 1971. doi: 10.1007/BF00148826. pages 13, 16, 42

M. Goossens, editor. *An introduction to plasma astrophysics and magnetohydrodynamics*, volume 294 of *Astrophysics and Space Science Library*, Oct. 2003. doi: 10.1007/978-94-007-1076-4. pages 26, 27

M. Goossens, J. Andries, and M. J. Aschwanden. Coronal loop oscillations. An interpretation in terms of resonant absorption of quasi-mode kink oscillations. *A&A*, 394:L39–L42, Nov. 2002. doi: 10.1051/0004-6361:20021378. pages 82

P. Gouttebroze and N. Labrosse. Radiative transfer in cylindrical threads with incident radiation. VI. A hydrogen plus helium system. *A&A*, 503:663–671, Sept. 2009. doi: 10.1051/0004-6361/200811483. pages 14

W. Grotrian. Zur physikalischen Deutung der Lichtkurve der Nova Herculis 1934. Mit 3 Abbildungen. *ZAp*, 13:215, 1937. pages 9

M. Gruszecki and V. M. Nakariakov. Slow magnetacoustic waves in magnetic arcades. *A&A*, 536:A68, Dec. 2011. doi: 10.1051/0004-6361/201117549. pages 82

P. Henri, S. S. Cerri, F. Califano, F. Pegoraro, C. Rossi, M. Faganello, O. Šebek, P. M. Trávníček, P. Hellinger, J. T. Frederiksen, A. Nordlund, S. Markidis, R. Keppens, and G. Lapenta. Nonlinear evolution of the magnetized Kelvin-Helmholtz instability: From fluid to kinetic modeling. *Physics of Plasmas*, 20(10):102118, Oct. 2013. doi: 10.1063/1.4826214. pages 101, 105

J. Heyvaerts and E. R. Priest. Coronal heating by phase-mixed shear Alfven waves. *A&A*, 117:220–234, Jan. 1983. pages 101

E. Hildner. The Formation of Solar Quiescent Prominences by Condensation. *Sol. Phys.*, 35:123–136, Mar. 1974. doi: 10.1007/BF00156962. pages 13, 16

T. Hirayama. Theoretical Model of Flares and Prominences. I: Evaporating Flare Model. *Sol. Phys.*, 34:323–338, Feb. 1974. doi: 10.1007/BF00153671. pages 21

T. Hirayama. Modern observations of solar prominences. *Sol. Phys.*, 100:415–434, Oct. 1985. doi: 10.1007/BF00158439. pages 48

P. Hoyng, A. Duijveman, M. E. Machado, D. M. Rust, Z. Svestka, A. Boelee, C. de Jager, K. T. Frost, H. Lafleur, G. M. Simnett, H. F. van Beek, and B. E. Woodgate. Origin and Location of the Hard X-Ray Emission in a Two-Ribbon Flare. *ApJ*, 246: L155, June 1981. doi: 10.1086/183574. pages 100

H. S. Hudson. A purely coronal hard X-ray event. *ApJ*, 224:235–240, Aug. 1978. doi: 10.1086/156370. pages 100

H. S. Hudson. Global Properties of Solar Flares. *Space Sci. Rev.*, 158:5–41, Jan. 2011. doi: 10.1007/s11214-010-9721-4. pages 100

S. Kamio, H. Peter, W. Curdt, and S. K. Solanki. Continuous upflows and sporadic downflows observed in active regions. *A&A*, 532:A96, Aug. 2011. doi: 10.1051/0004-6361/201117188. pages 15, 42

J. T. Karpen and S. K. Antiochos. Condensation Formation by Impulsive Heating in Prominences. *ApJ*, 676:658-671, Mar. 2008. doi: 10.1086/526335. pages 16

J. T. Karpen, S. K. Antiochos, M. Hohensee, J. A. Klimchuk, and P. J. MacNeice. Are Magnetic Dips Necessary for Prominence Formation? *ApJ*, 553:L85–L88, May 2001. doi: 10.1086/320497. pages 17, 42

J. T. Karpen, S. K. Antiochos, J. A. Klimchuk, and P. J. MacNeice. Constraints on the Magnetic Field Geometry in Prominences. *ApJ*, 593:1187–1194, Aug. 2003. doi: 10.1086/376690. pages 16

J. T. Karpen, S. E. M. Tanner, S. K. Antiochos, and C. R. DeVore. Prominence Formation by Thermal Nonequilibrium in the Sheared-Arcade Model. *ApJ*, 635: 1319–1328, Dec. 2005. doi: 10.1086/497531. pages 17

J. T. Karpen, S. K. Antiochos, and J. A. Klimchuk. The Origin of High-Speed Motions and Threads in Prominences. *ApJ*, 637:531–540, Jan. 2006. doi: 10.1086/498237. pages 16, 17

I. Kawaguchi. Observed Interaction between Prominences. *PASJ*, 22:405, 1970. pages 14, 41

R. Keppens and O. Porth. Scalar hyperbolic {PDE} simulations and coupling strategies. *Journal of Computational and Applied Mathematics*, 266:87 – 101, 2014. ISSN 0377-0427. doi: http://dx.doi.org/10.1016/j.cam.2014.01.017. URL `http://www.sciencedirect.com/science/article/pii/S0377042714000387`. pages 45, 84, 102

R. Keppens and C. Xia. The Dynamics of Funnel Prominences. *ApJ*, 789:22, July 2014. doi: 10.1088/0004-637X/789/1/22. pages 43

R. Keppens, G. Tóth, R. H. J. Westermann, and J. P. Goedbloed. Growth and saturation of the Kelvin-Helmholtz instability with parallel and antiparallel magnetic fields. *Journal of Plasma Physics*, 61:1–19, Jan. 1999. doi: 10.1017/S0022377898007223. pages 101, 105

R. Keppens, Z. Meliani, A. van Marle, P. Delmont, A. Vlasis, and B. van der Holst. Parallel, grid-adaptive approaches for relativistic hydro and magnetohydrodynamics. *Journal of Computational Physics*, 231(3):718 – 744, 2012. ISSN 0021-9991. doi: http://dx.doi.org/10.1016/j.jcp.2011.01.020. URL `http://www.sciencedirect.com/science/article/pii/S0021999111000386`. Special Issue: Computational Plasma PhysicsSpecial Issue: Computational Plasma Physics. pages 35, 37, 45, 84, 102

S. Kim, V. M. Nakariakov, and K. Shibasaki. Slow Magnetoacoustic Oscillations in the Microwave Emission of Solar Flares. *ApJ*, 756:L36, Sept. 2012. doi: 10.1088/2041-8205/756/2/L36. pages 82

L. Kleint, P. Antolin, H. Tian, P. Judge, P. Testa, B. De Pontieu, J. Martínez-Sykora, K. K. Reeves, J. P. Wuelser, S. McKillop, S. Saar, M. Carlsson, P. Boerner, N. Hurlburt, J. Lemen, T. D. Tarbell, A. Title, L. Golub, V. Hansteen, S. Jaeggli, and C. Kankelborg. Detection of Supersonic Downflows and Associated Heating Events in the Transition Region above Sunspots. *ApJ*, 789:L42, July 2014. doi: 10.1088/2041-8205/789/2/L42. pages 42, 63, 64, 65

B. Kliem. Particle orbits, trapping, and acceleration in a filamentary current sheet model. *ApJS*, 90:719–728, Feb. 1994. doi: 10.1086/191896. pages 20

J. A. Klimchuk, J. T. Karpen, and S. K. Antiochos. Can Thermal Nonequilibrium Explain Coronal Loops? *ApJ*, 714:1239–1248, May 2010. doi: 10.1088/0004-637X/714/2/1239. pages 52

R. A. Kopp and G. W. Pneuman. Magnetic reconnection in the corona and the loop prominence phenomenon. *Sol. Phys.*, 50:85–98, Oct. 1976. doi: 10.1007/BF00206193. pages 21

A. A. Korchak. On the Origin of Solar Flare X-Rays. *Sol. Phys.*, 18:284–304, June 1971. doi: 10.1007/BF00145943. pages 100

S. Krucker and M. Battaglia. Particle Densities within the Acceleration Region of a Solar Flare. *ApJ*, 780:107, Jan. 2014. doi: 10.1088/0004-637X/780/1/107. pages 100

S. Krucker and R. P. Lin. Hard X-Ray Emissions from Partially Occulted Solar Flares. *ApJ*, 673:1181-1187, Feb. 2008. doi: 10.1086/524010. pages 100

S. Krucker, M. Battaglia, P. J. Cargill, L. Fletcher, H. S. Hudson, A. L. MacKinnon, S. Masuda, L. Sui, M. Tomczak, A. L. Veronig, L. Vlahos, and S. M. White. Hard X-ray emission from the solar corona. *A&A Rev.*, 16:155–208, Oct. 2008. doi: 10.1007/s00159-008-0014-9. pages 100, 105, 107

P. Kumar, D. E. Innes, and B. Inhester. Solar Dynamics Observatory/Atmospheric Imaging Assembly Observations of a Reflecting Longitudinal Wave in a Coronal Loop. *ApJ*, 779:L7, Dec. 2013. doi: 10.1088/2041-8205/779/1/L7. pages 83, 93, 112

P. Kumar, V. M. Nakariakov, and K.-S. Cho. X-Ray and EUV Observations of Simultaneous Short and Long Period Oscillations in Hot Coronal Arcade Loops. *ApJ*, 804:4, May 2015. doi: 10.1088/0004-637X/804/1/4. pages 83, 90, 92, 93, 112

N. Labrosse, P. Heinzel, J.-C. Vial, T. Kucera, S. Parenti, S. Gunár, B. Schmieder, and G. Kilper. Physics of Solar Prominences: Spectral Diagnostics and Non-LTE Modelling. *Space Sci. Rev.*, 151:243–332, Apr. 2010. doi: 10.1007/s11214-010-9630-6. pages 13

J.-L. Leroy. Emissions 'froides' dans la couronne solaire. *Sol. Phys.*, 25:413–417, Aug. 1972. doi: 10.1007/BF00192338. pages 14, 41

R. H. Levine and G. L. Withbroe. Physics of an active region loop system. *Sol. Phys.*, 51:83–101, Feb. 1977. doi: 10.1007/BF00240447. pages 15

W. Liu and L. Ofman. Advances in Observing Various Coronal EUV Waves in the SDO Era and Their Seismological Applications (Invited Review). *Sol. Phys.*, 289: 3233–3277, Sept. 2014. doi: 10.1007/s11207-014-0528-4. pages 82

W. Liu, S. Liu, Y. W. Jiang, and V. Petrosian. RHESSI Observation of Chromospheric Evaporation. *ApJ*, 649:1124–1139, Oct. 2006. doi: 10.1086/506268. pages 103, 107

W. Liu, V. Petrosian, and J. T. Mariska. Combined Modeling of Acceleration, Transport, and Hydrodynamic Response in Solar Flares. I. The Numerical Model. *ApJ*, 702:1553–1566, Sept. 2009. doi: 10.1088/0004-637X/702/2/1553. pages 103

M. Luna, J. T. Karpen, and C. R. DeVore. Formation and Evolution of a Multi-threaded Solar Prominence. *ApJ*, 746:30, Feb. 2012. doi: 10.1088/0004-637X/746/1/30. pages 17

D. H. Mackay, J. T. Karpen, J. L. Ballester, B. Schmieder, and G. Aulanier. Physics of Solar Prominences: Magnetic Structure and Dynamics. *Space Sci. Rev.*, 151: 333–399, Apr. 2010. doi: 10.1007/s11214-010-9628-0. pages 13

S. Mandal, D. Yuan, X. Fang, D. Banerjee, V. Pant, and T. Van Doorsselaere. Reflection Of Propagating Slow Magneto-acoustic Waves In Hot Coronal Loops : Multi-instrument Observations and Numerical Modelling. *ArXiv e-prints*, Apr. 2016. pages ix, 94

J. T. Mariska. Observations of Solar Flare Doppler Shift Oscillations with the Bragg Crystal Spectrometer on Yohkoh. *ApJ*, 620:L67–L70, Feb. 2005. doi: 10.1086/428611. pages 82

J. T. Mariska. Characteristics of Solar Flare Doppler-Shift Oscillations Observed with the Bragg Crystal Spectrometer on Yohkoh. *ApJ*, 639:484–494, Mar. 2006. doi: 10.1086/499296. pages 82

J. T. Mariska, A. G. Emslie, and P. Li. Numerical simulations of impulsively heated solar flares. *ApJ*, 341:1067–1074, June 1989. doi: 10.1086/167564. pages 103

S. Masuda, T. Kosugi, H. Hara, S. Tsuneta, and Y. Ogawara. A loop-top hard X-ray source in a compact solar flare as evidence for magnetic reconnection. *Nature*, 371: 495–497, Oct. 1994. doi: 10.1038/371495a0. pages 100

K. G. McClements and D. Alexander. Fokker-Planck Modeling of Asymmetric Footpoint Hard X-Ray Emission in Solar Flares. *ApJ*, 619:1153–1159, Feb. 2005. doi: 10.1086/426581. pages 103

Z. Meliani, R. Keppens, and B. Giacomazzo. Faranoff-Riley type I jet deceleration at density discontinuities. Relativistic hydrodynamics with a realistic equation of state. *A&A*, 491:321–337, Nov. 2008. doi: 10.1051/0004-6361:20079185. pages 34, 46, 77

C. A. Mendoza-Briceño, L. D. G. Sigalotti, and R. Erdélyi. Catastrophic Cooling of Impulsively Heated Coronal Loops. *ApJ*, 624:1080–1092, May 2005. doi: 10.1086/429249. pages 17

J. A. Miller. Electron Acceleration in Solar Flares by Fast Mode Waves: Quasi-linear Theory and Pitch-Angle Scattering. *ApJ*, 491:939–951, Dec. 1997. pages 107

R. O. Milligan, P. T. Gallagher, M. Mathioudakis, D. S. Bloomfield, F. P. Keenan, and R. A. Schwartz. RHESSI and SOHO CDS Observations of Explosive Chromospheric Evaporation. *ApJ*, 638:L117–L120, Feb. 2006. doi: 10.1086/500555. pages 22

Y. Mok, J. F. Drake, D. D. Schnack, and G. van Hoven. Prominence formation in a coronal loop. *ApJ*, 359:228–231, Aug. 1990. doi: 10.1086/169053. pages 13, 16, 42

Y. Mok, Z. Mikić, R. Lionello, and J. A. Linker. Calculating the Thermal Structure of Solar Active Regions in Three Dimensions. *ApJ*, 621:1098–1108, Mar. 2005. doi: 10.1086/427739. pages 44

Y. Mok, Z. Mikić, R. Lionello, and J. A. Linker. The Formation of Coronal Loops by Thermal Instability in Three Dimensions. *ApJ*, 679:L161–L165, June 2008. doi: 10.1086/589440. pages 13, 16

D. A. N. Müller, V. H. Hansteen, and H. Peter. Dynamics of solar coronal loops. I. Condensation in cool loops and its effect on transition region lines. *A&A*, 411: 605–613, Dec. 2003. doi: 10.1051/0004-6361:20031328. pages 17, 42, 47, 52, 59

D. A. N. Müller, H. Peter, and V. H. Hansteen. Dynamics of solar coronal loops. II. Catastrophic cooling and high-speed downflows. *A&A*, 424:289–300, Sept. 2004. doi: 10.1051/0004-6361:20040403. pages 17, 42, 52

D. A. N. Müller, A. De Groof, V. H. Hansteen, and H. Peter. High-speed coronal rain. *A&A*, 436:1067–1074, June 2005. doi: 10.1051/0004-6361:20042141. pages 15, 17, 42, 48, 52

V. M. Nakariakov and V. F. Melnikov. Quasi-Periodic Pulsations in Solar Flares. *Space Sci. Rev.*, 149:119–151, Dec. 2009. doi: 10.1007/s11214-009-9536-3. pages 82

V. M. Nakariakov and L. Ofman. Determination of the coronal magnetic field by coronal loop oscillations. *A&A*, 372:L53–L56, June 2001. doi: 10.1051/0004-6361:20010607. pages 82

V. M. Nakariakov, D. Tsiklauri, A. Kelly, T. D. Arber, and M. J. Aschwanden. Acoustic oscillations in solar and stellar flaring loops. *A&A*, 414:L25–L28, Jan. 2004. doi: 10.1051/0004-6361:20031738. pages 82

S. Nitta, S. Imada, and T. T. Yamamoto. Clear Detection of Chromospheric Evaporation Upflows with High Spatial/Temporal Resolution by Hinode XRT. *Sol. Phys.*, 276:183–197, Feb. 2012. doi: 10.1007/s11207-011-9890-7. pages 103

L. Ofman and T. Wang. Hot Coronal Loop Oscillations Observed by SUMER: Slow Magnetosonic Wave Damping by Thermal Conduction. *ApJ*, 580:L85–L88, Nov. 2002. doi: 10.1086/345548. pages 82, 93

E. O'Shea, D. Banerjee, and J. G. Doyle. Plasma condensation in coronal loops. *A&A*, 475:L25–L28, Nov. 2007. doi: 10.1051/0004-6361:20078617. pages 14, 41

E. N. Parker. Instability of Thermal Fields. *ApJ*, 117:431, May 1953. doi: 10.1086/145707. pages 13, 16, 20, 41

E. N. Parker. Sweet's Mechanism for Merging Magnetic Fields in Conducting Fluids. *J. Geophys. Res.*, 62:509–520, Dec. 1957. doi: 10.1029/JZ062i004p00509. pages 12

E. N. Parker. Nanoflares and the solar X-ray corona. *ApJ*, 330:474–479, July 1988. doi: 10.1086/166485. pages 11, 17

S. Patsourakos and J.-C. Vial. Soho Contribution to Prominence Science. *Sol. Phys.*, 208:253–281, Aug. 2002. doi: 10.1023/A:1020510120772. pages 14

V. Petrosian and S. Liu. Stochastic Acceleration of Electrons and Protons. I. Acceleration by Parallel-Propagating Waves. *ApJ*, 610:550–571, July 2004. doi: 10.1086/421486. pages 107

H. E. Petschek. Magnetic Field Annihilation. *NASA Special Publication*, 50:425, 1964. pages 12, 20

R. F. Pinto, N. Vilmer, and A. S. Brun. Soft X-ray emission in kink-unstable coronal loops. *A&A*, 576:A37, Apr. 2015. doi: 10.1051/0004-6361/201323358. pages 103

O. Porth, C. Xia, T. Hendrix, S. P. Moschou, and R. Keppens. MPI-AMRVAC for Solar and Astrophysics. *ApJS*, 214:4, Sept. 2014. doi: 10.1088/0067-0049/214/1/4. pages 45, 84, 102

B. Roberts. Waves and Oscillations in the Corona - (Invited Review). *Sol. Phys.*, 193: 139–152, Apr. 2000. doi: 10.1023/A:1005237109398. pages 82

T. Sakurai, K. Ichimoto, K. P. Raju, and J. Singh. Spectroscopic Observation of Coronal Waves. *Sol. Phys.*, 209:265–286, Oct. 2002. doi: 10.1023/A:1021297313448. pages 91

C. J. Schrijver. Catastrophic cooling and high-speed downflow in quiescent solar coronal loops observed with TRACE. *Sol. Phys.*, 198:325–345, Feb. 2001. doi: 10.1023/A:1005211925515. pages 14, 17, 41, 42, 52

M. Schwarzschild. On Noise Arising from the Solar Granulation. *ApJ*, 107:1, Jan. 1948. doi: 10.1086/144983. pages 11

E. Scullion, L. Rouppe van der Voort, S. Wedemeyer, and P. Antolin. Unresolved Fine-scale Structure in Solar Coronal Loop-tops. *ApJ*, 797:36, Dec. 2014. doi: 10.1088/0004-637X/797/1/36. pages 43

M. Selwa, K. Murawski, and S. K. Solanki. Excitation and damping of slow magnetosonic standing waves in a solar coronal loop. *A&A*, 436:701–709, June 2005. doi: 10.1051/0004-6361:20042319. pages 82

M. Selwa, L. Ofman, and K. Murawski. Numerical Simulations of Slow Standing Waves in a Curved Solar Coronal Loop. *ApJ*, 668:L83–L86, Oct. 2007. doi: 10.1086/522602. pages 82

K. Shibata and T. Magara. Solar Flares: Magnetohydrodynamic Processes. *Living Reviews in Solar Physics*, 8, Dec. 2011. doi: 10.12942/lrsp-2011-6. pages 100

K. Shibata and T. Yokoyama. Origin of the Universal Correlation between the Flare Temperature and the Emission Measure for Solar and Stellar Flares. *ApJ*, 526: L49–L52, Nov. 1999. doi: 10.1086/312354. pages 20, 21

A. V. R. Silva, H. Wang, D. E. Gary, N. Nitta, and H. Zirin. Imaging the Chromospheric Evaporation of the 1994 June 30 Solar Flare. *ApJ*, 481:978–987, May 1997. pages 103

L. Spitzer, Jr. On a Possible Interstellar Galactic Corona. *ApJ*, 124:20, July 1956. doi: 10.1086/146200. pages 13

P. A. Sturrock. A Model of Quasi-Stellar Radio Sources. *Nature*, 211:697–700, Aug. 1966. doi: 10.1038/211697a0. pages 21

P. A. Sweet. The Neutral Point Theory of Solar Flares. In B. Lehnert, editor, *Electromagnetic Phenomena in Cosmical Physics*, volume 6 of *IAU Symposium*, page 123, 1958. pages 12, 20

E. Tandberg-Hanssen. Books-Received - the Nature of Solar Prominences. *Science*, 269:111, July 1995. pages 37

Y. Taroyan and R. Erdélyi. Heating Diagnostics with MHD Waves. *Space Sci. Rev.*, 149:229–254, Dec. 2009. doi: 10.1007/s11214-009-9506-9. pages 11, 12

Y. Taroyan, R. Erdélyi, J. G. Doyle, and S. J. Bradshaw. Footpoint excitation of standing acoustic waves in coronal loops. *A&A*, 438:713–720, Aug. 2005. doi: 10.1051/0004-6361:20052794. pages 82

Y. Taroyan, R. Erdélyi, T. J. Wang, and S. J. Bradshaw. Forward Modeling of Hot Loop Oscillations Observed by SUMER and SXT. *ApJ*, 659:L173–L176, Apr. 2007. doi: 10.1086/517521. pages 82

R. J. Thomas, C. J. Crannell, and R. Starr. Expressions to determine temperatures and emission measures for solar X-ray events from GOES measurements. *Sol. Phys.*, 95:323–329, Feb. 1985. doi: 10.1007/BF00152409. pages 18

M. Tomczak. The analysis of hard X-ray radiation of flares with occulted footpoints. *A&A*, 366:294–305, Jan. 2001. doi: 10.1051/0004-6361:20000204. pages 100

E. F. Toro, M. Spruce, and W. Speares. Restoration of the contact surface in the HLL-Riemann solver. *Shock Waves*, 4:25–34, July 1994. doi: 10.1007/BF01414629. pages 33

R. H. D. Townsend. An Exact Integration Scheme for Radiative Cooling in Hydrodynamical Simulations. *ApJS*, 181:391–397, Apr. 2009. doi: 10.1088/0067-0049/181/2/391. pages 34, 43

D. Tripathi, H. E. Mason, B. N. Dwivedi, G. del Zanna, and P. R. Young. Active Region Loops: Hinode/Extreme-Ultraviolet Imaging Spectrometer Observations. *ApJ*, 694:1256–1265, Apr. 2009. doi: 10.1088/0004-637X/694/2/1256. pages 14, 63

D. Tsiklauri, V. M. Nakariakov, T. D. Arber, and M. J. Aschwanden. Flare-generated acoustic oscillations in solar and stellar coronal loops. *A&A*, 422:351–355, July 2004. doi: 10.1051/0004-6361:20040299. pages 82

R. Turkmani, P. J. Cargill, K. Galsgaard, L. Vlahos, and H. Isliker. Particle acceleration in stochastic current sheets in stressed coronal active regions. *A&A*, 449:749–757, Apr. 2006. doi: 10.1051/0004-6361:20053548. pages 100

I. Ugarte-Urra, H. P. Warren, and D. H. Brooks. Hinode Coronal Loop Observations. In B. Lites, M. Cheung, T. Magara, J. Mariska, and K. Reeves, editors, *The Second Hinode Science Meeting: Beyond Discovery-Toward Understanding*, volume 415 of *Astronomical Society of the Pacific Conference Series*, page 241, Dec. 2009. pages 18

R. A. M. van der Linden and M. Goossens. The thermal continuum in coronal loops - Instability criteria and the influence of perpendicular thermal conduction. *Sol. Phys.*, 134:247–273, Aug. 1991a. doi: 10.1007/BF00152647. pages 13, 74

R. A. M. van der Linden and M. Goossens. Thermal instability in slab geometry in the presence of anisotropical thermal conduction. *Sol. Phys.*, 131:79–105, Jan. 1991b. doi: 10.1007/BF00151746. pages 13

T. Van Doorsselaere, A. De Groof, J. Zender, D. Berghmans, and M. Goossens. LYRA Observations of Two Oscillation Modes in a Single Flare. *ApJ*, 740:90, Oct. 2011a. doi: 10.1088/0004-637X/740/2/90. pages 82

T. Van Doorsselaere, N. Wardle, G. Del Zanna, K. Jansari, E. Verwichte, and V. M. Nakariakov. The First Measurement of the Adiabatic Index in the Solar Corona Using Time-dependent Spectroscopy of Hinode/EIS Observations. *ApJ*, 727:L32, Feb. 2011b. doi: 10.1088/2041-8205/727/2/L32. pages 82

A. J. van Marle, Z. Meliani, R. Keppens, and L. Decin. Computing the Dust Distribution in the Bow Shock of a Fast-moving, Evolved Star. *ApJ*, 734:L26, June 2011. doi: 10.1088/2041-8205/734/2/L26. pages 44

A. M. Veronig and J. C. Brown. A Coronal Thick-Target Interpretation of Two Hard X-Ray Loop Events. *ApJ*, 603:L117–L120, Mar. 2004. doi: 10.1086/383199. pages 100

A. M. Veronig, J. C. Brown, B. R. Dennis, R. A. Schwartz, L. Sui, and A. K. Tolbert. Physics of the Neupert Effect: Estimates of the Effects of Source Energy, Mass Transport, and Geometry Using RHESSI and GOES Data. *ApJ*, 621:482–497, Mar. 2005. doi: 10.1086/427274. pages 100, 107

E. Verwichte, M. Haynes, T. D. Arber, and C. S. Brady. Damping of Slow MHD Coronal Loop Oscillations by Shocks. *ApJ*, 685:1286-1290, Oct. 2008. doi: 10.1086/591077. pages 92

T. Wang. Standing Slow-Mode Waves in Hot Coronal Loops: Observations, Modeling, and Coronal Seismology. *Space Sci. Rev.*, 158:397–419, July 2011. doi: 10.1007/s11214-010-9716-1. pages 82, 83, 85, 90

T. Wang, Y. Yan, J. Wang, H. Kurokawa, and K. Shibata. The Large-Scale Coronal Field Structure and Source Region Features for a Halo Coronal Mass Ejection. *ApJ*, 572:580–597, June 2002. doi: 10.1086/340189. pages 82

T. Wang, D. E. Innes, and J. Qiu. Determination of the Coronal Magnetic Field from Hot-Loop Oscillations Observed by SUMER and SXT. *ApJ*, 656:598–609, Feb. 2007. doi: 10.1086/510424. pages 82

T. J. Wang, S. K. Solanki, W. Curdt, D. E. Innes, I. E. Dammasch, and B. Kliem. Hot coronal loop oscillations observed with SUMER: Examples and statistics. *A&A*, 406:1105–1121, Aug. 2003a. doi: 10.1051/0004-6361:20030858. pages 82, 91

T. J. Wang, S. K. Solanki, D. E. Innes, W. Curdt, and E. Marsch. Slow-mode standing waves observed by SUMER in hot coronal loops. *A&A*, 402:L17–L20, May 2003b. doi: 10.1051/0004-6361:20030448. pages 82, 93

Y.-M. Wang. The Jetlike Nature of He II λ304 Prominences. *ApJ*, 520:L71–L74, July 1999. doi: 10.1086/312149. pages 16

G. L. Withbroe and R. W. Noyes. Mass and energy flow in the solar chromosphere and corona. *ARA&A*, 15:363–387, 1977. doi: 10.1146/annurev.aa.15.090177.002051. pages 11

T. N. Woods, G. Kopp, and P. C. Chamberlin. Contributions of the solar ultraviolet irradiance to the total solar irradiance during large flares. *Journal of Geophysical Research (Space Physics)*, 111:A10S14, Oct. 2006. doi: 10.1029/2005JA011507. pages 19

C. Xia, P. F. Chen, R. Keppens, and A. J. van Marle. Formation of Solar Filaments by Steady and Nonsteady Chromospheric Heating. *ApJ*, 737:27, Aug. 2011. doi: 10.1088/0004-637X/737/1/27. pages 16, 17, 42, 43, 45, 53, 61

C. Xia, P. F. Chen, and R. Keppens. Simulations of Prominence Formation in the Magnetized Solar Corona by Chromospheric Heating. *ApJ*, 748:L26, Apr. 2012. doi: 10.1088/2041-8205/748/2/L26. pages 37, 43, 53, 84

T. Yokoyama and K. Shibata. A Two-dimensional Magnetohydrodynamic Simulation of Chromospheric Evaporation in a Solar Flare Based on a Magnetic Reconnection Model. *ApJ*, 494:L113–L116, Feb. 1998. doi: 10.1086/311174. pages 22

T. Yokoyama and K. Shibata. Magnetohydrodynamic Simulation of a Solar Flare with Chromospheric Evaporation Effect Based on the Magnetic Reconnection Model. *ApJ*, 549:1160–1174, Mar. 2001. doi: 10.1086/319440. pages 103

S. Yu, V. M. Nakariakov, L. A. Selzer, B. Tan, and Y. Yan. Quasi-periodic Wiggles of Microwave Zebra Structures in a Solar Flare. *ApJ*, 777:159, Nov. 2013. doi: 10.1088/0004-637X/777/2/159. pages 93

D. Yuan, V. M. Nakariakov, Z. Huang, B. Li, J. Su, Y. Yan, and B. Tan. Oscillations in a Sunspot with Light Bridges. *ApJ*, 792:41, Sept. 2014a. doi: 10.1088/0004-637X/792/1/41. pages 82

D. Yuan, R. Sych, V. E. Reznikova, and V. M. Nakariakov. Multi-height observations of magnetoacoustic cut-off frequency in a sunspot atmosphere. *A&A*, 561:A19, Jan. 2014b. doi: 10.1051/0004-6361/201220208. pages 82

D. Yuan, T. Van Doorsselaere, D. Banerjee, and P. Antolin. Forward Modeling of Standing Slow Modes in Flaring Coronal Loops. *ApJ*, 807:98, July 2015. doi: 10.1088/0004-637X/807/1/98. pages 85, 91

H. Zanstra. On the Formation of Condensations in a Gaseous Nebula. In *Gas Dynamics of Cosmic Clouds*, volume 2 of *IAU Symposium*, page 70, 1955. pages 13

Curriculum

Xia Fang

Email: xia.alex.fang@gmail.com
Address: Celestijnenlaan 200B 3.33 3001 Heverlee, Belgium

Research Interest

- MHD Simulation
- High Performance Computing
- Solar Plasma Physics
- High Energy Astronomy

Education

2012-2016	PhD Student
	Katholieke Universiteit Leuven, Belgium
2009-2009	Master Student
	Nanjing University, China
2005-2009	Bachelor Student
	Nanjing University, China

Posters and Talks

1. Oral talk at The 6th Coronal Loops Workshop, July 25-27, La-Roche, 2013.
2. Oral talk at The 2th Asian-Pacific solar physics meeting, Oct 21-26, Hangzhou, China, 2013.
3. Oral talk at Charm first annual meeting, April 18-19, Brussel, 2013.
4. Poster at the CosmoComp/CHARM spring school, May 27-31, Leiden, 2013.

5. Poster at IAUS300, Nature of Prominences and their role in Space Weather, July 10-14, Paris, 2013.
6. Oral talk at The 6th Coronal Loops Workshop, July 25-27, La-Roche, 2013.
7. Poster at 69th Dutch Astronomy Conference, May 19-21, Noordwijkerhout, 2014.
8. Oral Talks at ISSI Workshop, Feb 23-27, Bern, 2015.
9. Poster at 7th Coronal Loop Workshop, July 21-23, Cambridge, 2015.
10. Seminars, The Role of Kelvin-Helmholtz Instability for Producing Loop-top Hard X-ray Sources in Solar Flares, Sep 27-30, 2015.
11. Poster at AGU Fall Meeting, December 14-18, San Francisco, 2015.

List of publications

[1] Fang, X.; Xia, C.; Keppens, R. Multidimensional Modeling of Coronal Rain Dynamics. The Astrophysical Journal Letters, Volume 771, Issue 2, article id. L29, 6 pp. (2013)

[2] Fang, X.; Xia, C.; Keppens, R. Modeling Prominence Formation in 2.5D. Proceedings of the International Astronomical Union, IAU Symposium, Volume 300, pp. 410-411. (2014)

[3] Fang, X.; Xia, C.; Keppens, R.; Van Doorsselaere, T. Coronal Rain in Magnetic Arcades: Rebound Shocks, Limit Cycles, and Shear Flows. The Astrophysical Journal, Volume 807, Issue 2, article id. 142, 15 pp. (2015)

[4] Fang, X.; Yuan, D.; Van Doorsselaere, T.; Keppens, R.; Xia, C. Modeling of Reflective Propagating Slow-mode Wave in a Flaring Loop. The Astrophysical Journal, Volume 813, Issue 1, article id. 33, 8 pp. (2015)

[5] Moschou, S. P.; Keppens, R.; Xia, C.; Fang, X. Simulating coronal condensation dynamics in 3D. Advances in Space Research, Volume 56, Issue 12, p. 2738-2759. (2015)

[6] Mandal, S.; Yuan, D.; Fang, X.; Banerjee, D.; Pant, V.; Van Doorsselaere, T. Reflection Of Propagating Slow Magneto-acoustic Waves In Hot Coronal Loops : Multi-instrument Observations and Numerical Modelling. The Astrophysical Journal, accepted. (2016)

[7] Fang, X.; Yuan, D.; Xia, C.; Keppens, R.; Van Doorsselaere, T. The Role of Kelvin-Helmholtz Instability for Producing Loop-top Hard X-ray Sources in Solar Flares. The Astrophysical Journal, in review. (2016)

FACULTY OF SCIENCE
DEPARTMENT OF MATHEMATICS
CENTRE FOR MATHEMATICAL PLASMA-ASTROPHYSICS
Celestijnenlaan 200B box 03.33
B-3001 Leuven
xia.fang@wis.kuleuven.be
http://wis.kuleuven.be/CmPA